Imperial College London

Department of Materials Engineering

DEVELOPMENT OF Fe_xN THIN FILMS WITH MICROCOMPRESSION ANALYSIS

Nur Izzati binti Muhammad Nadzri

May 2020

This thesis is submitted in part of fulfilment of the requirements for the degree of

Doctor of Philosophy

Abstract

This thesis explores the growth routes of metal nitrides based materials of binary and ternary nitrides. It is believed that this iron nitrides based materials exhibit interesting properties in term of electronic optical, thermal and magnetic properties. However, most experimental and analytical efforts in this research field have been carried out in the form of bulk samples and there was no research of these nitrides in thin films. Consider the unique characteristics of iron nitrides system, the binary and ternary nitrides of both Fe_xN and $Fe_xW_{y-1}N$ thin films were grown using electron beam physical vapor deposition method under metal rich conditions.

There exist significant challenges for the development of both binary and ternary nitrides thin films. It required to remain stable during the growth in order to incorporate nitrogen in the system to obtain Fe-N system due to the nature of nitrogen of having strong triple bond. The first aspect of this thesis investigates the development of these nitrides by using four different methods. Results from XRD and XPS reveal that there was formation of iron oxides on the thin films and further XPS data shows the percentage of nitrogen is lower than expected. The highest content of iron was then selected to proceed with second phase of the project with the aim of developing iron nitrides thin films with thicker films under higher growth temperature.

The formation of iron nitrides was found in the thin films with higher growth temperature. The XPS analysis that shows the presence of either Fe^{2+} or Fe^{3+} species in the sample and further investigation by TEM reveals the film hexagonal crystal structure which corresponds to Fe_3N. An attempt of growing ternary nitrides was carried out with different iron to tungsten ratio. However, in this preliminary study, we only managed to obtain W-N composition with a limited amount of iron presence in the sample. It was found that either the iron has been oxidised or some iron oxides or tungsten oxides were formed during the synthesis

Microcompression experiment was carried out on the thicker iron nitrides thin films in order to calculate their Young's modulus. It was found that the value is still lower than the bulk samples which may be corresponds to misalignment between the pillar and the system during the experiments. However, it was observed that there was no deformation such as crack occurred on the thin films during this test. Further study shall be carried out to have a better understanding of these iron nitrides based thin films.

Declaration of originality

I, Nur Izzati binti Muhammad Nadzri, declare that the work reported within this thesis is my own, unless otherwise stated. Collaborations are acknowledged in the text.

Copyright declaration

The copyright of this thesis rests with the author and is made available under a Creative Commons Attribution Non-Commercial No Derivatives licence. Researchers are free to copy, distribute or transmit the thesis on the condition that they attribute it, that they do not use it for commercial purposes and that they do not alter, transform or build upon it. For any reuse or redistribution, researchers must make clear to others the licence terms of this work.

Acknowledgements

Alhamdulillah. All Praise to be God the Almighty.

The work presented herein would not be possible without the scientific supervision and guidance of Dr Finn Giuliani and Dr Michelle Moram. Thank you for the support and guidance throughout this PhD studies, for being enthusiastic about this project, for never giving up on me and for believing in me. None of this would be possible without both of them. Thank you both!

To Dr. Robert Davies, a very special thank you, who was very critical and crucial with thin film growth in our Nitrides group. His ideas, dedication and motivation driven me to become better and without his unbelievable talent, it will not be possible for me to have my samples. Your contribution was priceless and deeply appreciated.

I would like to also to thank Dr. Kevin Zou and Dr Anna Regoutz for helping me to have a better understanding on XRD and XPS. For always giving me positive vibes and push me to believe in myself. My sincere thanks also go to Dr Mahmoud Ardakani and my cat lover good friend Dr Ecaterina War, for their patience during training sessions on both TEM and FIB.

I am also grateful to everyone at Imperial College London, especially my go-to scientific advisor Dr Sudha Joseph, Dr Sneha Rhode, Dr Matthew and Professor Eduardo Saiz. Thank you for making it bearable when everything seems out of reach. For my coffee sessions friends, Maryam, Muzamir, Aida, Farah, Azizi, Iman, Nikman, Aini and Faridah-thank you for keeping me sane. For my good friends back home, Teha, Afrah, Pia and Kak Raz.

To my siblings, Kakni and Adik, thank you for taking a good care of our parents while I was away. Thank you for the silly advices and jokes. To my in laws, thank you for the encouragement.

I would like to also acknowledge Ministry of Higher Education Malaysia and Universiti Malaysia Perlis. Nothing to be grateful for other than receiving this scholarship.

Lastly, I owe my deepest gratitude to my Mom and Dad. I could not accomplish this work without your blessings. To my husband, Izzat Shahiman thank you for holding my hand at time of difficulties and to my little miracle, Izzat Mikhael Nadzmil. Thank you for being the little angel you are. We've made it!

List of Figures

Figure 1.1 From Hogbert et al.[1] The hexagonal crystal structures for the $M_{n+1}AXn$ phases (n = 1,2 or 3), showing the different stacking in the existing subgroups of the compositions M_2AX, M_3AX_2 and M_4AX_3 . **10**

Figure 1.2 From Geim and Grigorieva [2]. Building van der Waals heterostructures where a monolayer is place on top of other monolayer or few crystals and add another 2D crystal. **14**

Figure 1.3 Fe-N phase diagram[3] **15**

Figure 1.4 From Gölden *et al.*[4]. Thin film phase diagram of the iron nitride system. Thin films were grown by MBE. **17**

Figure 1.5 From Babu *et al.*[5]. AFM images of Fe-N on Si (100) films of (a) t = 40 nm, (b) t = 80 nm, (c) t = 160 nm and (d) t = 240 nm. **19**

Figure 1.6 From Bem *et al.* [6] , XRD pattern of $FeWN_2$. **20**

Figure 1.7 From Miura *et al.* [7]. Crystal structure of $FeWN_2$. Trigonal prismatic tungsten layers are shown as filled polyhedral. The iron and nitrogen positions are indicated in a ball and stick representation. Large and small balls represent iron and nitrogen, respectively. **21**

Figure 1.8 From Weil and Kumta [8]. SEM images showing the microstructure of (a) as dried precursors of Fe-W-N and (b) as heat treated at 950°C for 4 h in ammonia $FeWN_2$. **22**

Figure 1.9 Typical load-displacement curve obtained from an instrumented nanoindentation experiment performed with a Berkovich indenter, showing important analysis performances[9]. **27**

Figure 1.10 Adapted from Tommaso[10] where the Berkovich indenter geometry (not to scale) and θ_1 is the angle between the central axis and the **29**

pyramid face and θ_2 is the angle between the central axis and the pyramid's edge.

Figure 1.11 From Fei *et al.* [11]. Schematic of micropillar compression test **35**

Figure 2.1 From Dr. Robert Davies. Schematic diagram of the EB-PVD process. **40**

Figure 2.2 From Innova AFM Manual [12]. Schematic diagram of an AFM apparatus. **41**

Figure 2.3 From M. Moram and V.Vickers [13] Schematic of x-ray diffraction where the condition required for Bragg diffraction to occur. **44**

Figure 2.4 From T. Tsui [14]. Rotational axes of an X-ray diffractometer. **45**

Figure 2.5 From L. Calvo-barrio and G. Vargas [15]. (a) X-ray induced photoelectron emission and (b) Auger effect in the photoelectron emission. **47**

Figure 2.6 From Lin *et. al.*[16] XPS spectrum Fe $2p_{3/2}$ and $2p_{1/2}$ of FeN sample fabricated under a N_2 partial pressure of 0.2 mTorr. **48**

Figure 2.7 A basic SEM schematic diagram[17]. **50**

Figure 2.8 (a) Relrod in reciprocal space created from diffraction of a crystalline specimen and (b) The relrod when the beam is away from the exact Bragg condition. The Ewald sphere intercepts the relrod at a negative value of s which defines the vector **K = g + s** **54**

Figure 2.9 (a) An image of DP acquired along [0001] for a cross section sample of Fe_XN, showing the direct (0000) and (b) is a schematic diagram of the process to achieve a diffraction pattern. **55**

Figure 2.10 From Williams and Carter[18].Ray diagram showing how the objective lens and objective aperture is used in combination to produce (a) Bright field image that is formed from the direct electron beam and (b) a displaced aperture dark field image formed with a specific off axis scattered beam. **56**

Figure 2.11 A basic schematic diagram of a Ga liquid metal ion source in FIB column **60**

Figure 2.12 Image of a sapphire 0001 pillar with a cross pattern fiducial mark. Platinum deposition is placed on t on the fiducial mark to protect it from the beam damage during milling. **62**

Figure 2.13 (a) SEM micrograph showing a flat punch tip of 10 μm in diameter parallel to micropillar with (b) inserts of Alemnis nanoindentation platform for in-situ compression test and (c) the load-test conditions of loading and unloading of the tip displacement. **66**

Figure 3.1 2 x 2 um AFM images of Fe_xN films on sapphire (0001) substrate. All images were processed using parabolic flattening. **72**

Figure 3.2 XRD peaks of different Fe content of (a) x = 0.30 with a flow rate of 3 sccm, (b) x = 0.33 with a flow rate of 2 sccm and (c) x = 0.35 with a flow rate of 2 sccm grown on (0001) sapphire **74**

Figure 3.3 XPS survey spectrum for Fe_xN where (a) x = 0.30, (b) x = 0.33 and (c) x = 0.35 grown on sapphire (Al_2O_3). **76**

Figure 3.4 2 x 2 um AFM images of Fe_xN films on sapphire (0001) substrate under 1000ºC with (a) 30 minutes and (b) 3 hour of growth time with FexN (x = 0.35) in N_2 flow of 2sccm. All images were processed using parabolic flattening **79**

Figure 3.5 XRD peaks of Fe_xN thin film grown on (0001) sapphire for (a) different growth time of 30 minutes and 3 hours at 1000ºC and (b) enlarged peak of Fe3N (200) where showed small peak shifts occurred. **80**

Figure 3.6 XPS survey spectrum for Fe_xN where x = 0.35 at 1000C for (a) 30 minutes and (b) 3 hours. **82**

Figure 3.7 XPS core line spectra of Fe2p (a) 30 minutes and (b) 3 hour of growth time for x = 0.35 at 1000ºC. The red line is as received sample while the blue indicates after 600 seconds of etching. **84**

Figure 3.8 TEM Bright field image of Fe_xN (x=0.35) thin films on sapphire showing thickness in the range of 600 nm. **85**

Figure 3.9 Selected area diffraction pattern of (a) film with zone axis of [0001] and (b) substrate with zone axis of [12-16]. Both of the images are showing diffraction of hexagonal crystal structure. **86**

Figure 3.10 HRTEM images of sample with (a) film and sample shown a hexagonal crystal structure and (b) and higher resolution on the film to check the d-spacing for both [01-10] and [1-100] film directions. **87**

Figure 3.11 2 x 2 um AFM images of $Fe_xW_{y-1}N$ films on sapphire (0001) substrate. All images were processed using parabolic flattening. **90**

Figure 3.12 XRD of $Fe_xW_{y-1}N$ with (a) y = 0.32 (b) y = 0.33 and (c) y = 0.34 with 600ºC with 7.5 x 10^{-5} of base pressure. **91**

Figure 3.13 XPS survey spectrum for Fe_xN where (a) y = 0.32 (b) y = 0.33 and (c) y = 0.34 with 600ºC grown on sapphire (Al_2O_3). **92**

Figure 3.14 XPS depth profiling spectra of $Fe_xW_{y-1}N$ film on (a) y = 0.32 (b) y = 0.33 and (c) y = 0.34 at 600ºC. The red line is as received sample, blue indicates after 60 seconds of etching and yellow and green indicates 120 second and 180 second of etching. **94**

Figure 4.1 Load-displacement graphs of one of the MgO (100) pillars before and after the pillar correction when the stiffness surface is taken into account. **101**

Figure 4.2 The stress-strain curve of two pillars with an average diameter of 3 µm and 9 µm in diameter of height with five cyclic loading and unloading of MgO (100) with just the elastic portion plotted and then **104**

the Young's modulus fitted on (a) and (b) for Pillar 1 and (c) and (d) for Pillar 2.

Figure 4.3 Figure 4.3: Young's modulus (GPa) of Pillar 1 (black square) and Pillar 2 (red circle) of MgO (100) for five cycles during microcompression with two magenta lines that show literature value that was obtained from Chung[19] (indicates in triangle) and Baudson *et al.*[20] (indicates in star) which is between the values after second cycles for both pillars. **105**

Figure 4.4 Figure 4.4: Micropillar of MgO (100) of before and after compression for (a) Pillar 1 and (b) Pillar 2 with Quanta SE, 650F with the red arrows depicting changes of the behaviour of the pillars. **107**

Figure 4.5 Figure 4.5: Micropillar of MgO (100) which was under microcompression test where (a)stress-strain curve, (b) pop-in phenomenon in the third cycle of the sample and (c) image of before and after microcompression took place. **109**

Figure 4.6 Load-displacement graphs of one of the MgO (110) pillars before and after the pillar correction when the stiffness surface is taken into account. **110**

Figure 4.7 The stress-strain curve of two pillars with an average diameter of 3 μm and 9 μm in diameter of height with five cyclic loading and unloading of MgO (110) with just the elastic portion plotted and then the Young's modulus fitted on (a) and (b) for Pillar 1 and (c) and (d) for Pillar 2. **112**

Figure 4.8 Young's modulus (GPa) of Pillar 1 (black square) and Pillar 2 (red circle) of MgO (100) for five cycles during microcompression with two magenta lines that show literature value that was obtained from Isaak[21] (indicates in triangle) and Chang *et al.*[22](indicates in star) which is between the values after second cycles for both pillars. **113**

Figure 4.9 Micropillar of MgO (110) which was under microcompression test where (a)stress-strain curve, (b) pop-in phenomenon in the third cycle **116**

of the sample and (c) image of before and after microcompression took place.

Figure 4.10 Micropillar of MgO (110) which was under microcompression test where (a) stress-strain curve, (b) dislocation avalanches in the fifth cycle of the sample and (c) image of before and after microcompression took place. **118**

Figure 5.1 Fe_xN thin films with sapphire as the substrate. As presented, the sapphire is part of the pillar and also acted as a base for the thin film sample. **124**

Figure 5.2 Micropillar of FexN thin films on sapphire as substrate where Pillar 1 shows the average diameter and height. **124**

Figure 5.3 Load-displacement graphs of one of the sapphire (0001) pillars before and after the pillar correction was applied on them. **125**

Figure 5.4 The stress-strain curves of three pillars with a different diameter of height with five cyclic loading and unloading cycles for (a) pillar 1 and (b) pillar 2. **127**

Figure 5.5 Young's modulus (GPa) of Pillar 1 (black square) and Pillar 2 (red circle) of Sapphire (0001) for five cycles during microcompression, where the magenta lines indicate the sapphire literature data that was obtained from Saha and Nix[23] (indicates in star) and Zoubolis *et al.*[24] (indicates in triangle) which is between the values for third and fourth cycles for both pillars.. **128**

Figure 5.6 Before and after for both Pillar 1 and Pillar 2 of Sapphire (0001) that shows similar SEM images of pre and post microcompression test. **130**

Figure 5.7 Pillar 1 of Sapphire (0001) denotes the morphology of the pillar during point (a), (b), (c) and (d) of microcompression test. **131**

Figure 5.8 Pillar 2 of Sapphire (0001) denotes the morphology of the pillar during point (a), (b), (c) and (d) of microcompression test. **132**

Figure 5.9 Adapted from Chu *et al.*[25] where this schematic illustration demonstrates the method of extracting mechanical properties of thin film. In our case, the substrate used is sapphire and thin films is Fe_xN and we are using the same method to get Fe_xN thin films Young's modulus. **134**

Figure 5.10 The stress-strain curves of the thin film pillars with the substrates removed of five cyclic loading and unloading cycles of Fe_xN thin film on sapphire for (a) pillar 1 with a diameter of 2.89 μm, and (c) pillar 2 with a diameter of 2.56 μm. The Young's modulus was exracted from the unloading segment of (b) pillar 1 and (d) pillar 2. The $E_{sapphire}$ was directly obtained from previous sapphire micropillar compression test. **136**

Figure 5.11 Young's modulus (GPa) of Pillar 1 (black square) and Pillar 2 (red circle) of Fe_xN thin films for five cycles during microcompression where the magenta lines show the Fe_3N literature value that was obtained from Rissanen *et al.*[13](indicates in star) and Chen *et al.*[15](indicates in triangle) which is between the values for third and fourth cycles for both pillars. **137**

Figure 5.12 Figure 5.12: Micropillar of Fe_xN of before and after compression for (a) Pillar 1 and (b) Pillar 2 with Quanta SE, 650F with the red arrows depicting changes of the behaviour of the pillars. **140**

Figure 5.13 Pillar 1 of Fe_xN denotes the morphology of the pillar during point (a), (b), (c) and (d) of microcompression test. **141**

Figure 5.14 Pillar 2 of Fe_xN denotes the morphology of the pillar during point (a), (b), (c) and (d) of microcompression test. **142**

List of Tables

Table 1.1	Atomic radius of transition metals[26].	**4**
Table 1.2	Physical and Chemical Properties of Common Transition Metal Nitrides[27]	**5**
Table 1.3	Properties of Elastic Constants	**24**
Table 2.1	Summary of milling process of micropillars on MgO and sapphire	**62**
Table 3.1	Growth series of Fe_xN with x = 0.30, 0.33 and 0.35 grown on sapphire substrate	**70**
Table 3.2	Atomic percentage based survey scan spectra	**77**
Table 3.3	Growth series of Fe_xN (x = 0.35) at 1000°C for 30 minutes and 180 minutes grown on sapphire substrate	**78**
Table 3.4	Growth series of $Fe_xWy_{-1}N$ with different ratio of y = 0.32, 0.33, 0.34 grown on sapphire substrate	**88**
Table 3.5	Atomic percentage of $Fe_xW_{y-1}N$ based survey scan spectra	**93**

List of Acronyms

AFM	Atomic force microscopy
BSE	Back scattered electron
EB	Electron beam
EBPVD	Electron beam physical vapor deposition
FIB	Focused ion beam
HRTEM	High resolution transmission electron microscopy
LED	Light emitting diode
MBE	Molecular beam epitaxy
MOCVD	Metalorganic chemical vapor deposition
PLD	Pulsed laser deposition
RMS	Root-mean-square
RUS	Resonant ultrasound spectroscopy
SE	Secondary electron
SEM	Secondary electron microscopy
TEM	Transmission electron microscopy
XPS	X-ray photoelectron spectroscopy
XRD	X-ray diffraction

Table of Contents

Abstract ..... ***II***

Declaration of originality ..... ***IV***

Acknowledgements ..... ***V***

List of Figures ..... ***VII***

List of Tables ..... ***XIV***

List of Acronyms ..... ***XV***

Chapter 1: Introductions **1**

1.1 Motivation 1
1.2 Nitrides 2
1.3 Properties of metal nitrides 3
1.4 Layered nitrides: Binary and ternary 5
1.5 Challenges with ternary nitrides growth 7
1.5.1 3D layered nitrides 9
1.5.2 2D layered nitrides 13
1.6 Nitrides of interest in this work 14
1.6.1 Iron based nitrides material 15
1.6.2 Iron tungsten nitrides material 19
1.7 Elastic modulus measurements 22
1.7.1 Introduction 22
1.7.2 Experimental techniques of elastic constant measurements 25

Chapter 2: *Experimental techniques* ***38***

2.1 Epitaxial growth of Fe_xN 38
2.1.1 Electron beam physical vapor deposition (EBPVD) 38
2.2 Characterisation techniques 40
2.2.1 Atomic force microscopy 40
2.2.2 X-ray diffraction (XRD) 43
2.2.3 X-ray photoelectron spectroscopy (XPS) 46
2.2.4 Secondary electron microscopy (SEM) 49
2.2.4.1 Imaging 51
2.2.5 Transmission electron microscopy (TEM) 52
2.2.5.1 Sample preparation 52
2.2.5.2 TEM imaging 53
2.2.5.3 Mass thickness contrast, diffraction contrast and phase contrast 55
2.2.5.4 High resolution imaging 56
2.3 Mechanical property measurement 58
2.3.1 Principle of focused ion beam (FIB) 58
2.3.1.1 Fabrication of micropillars with focused ion beam 60
2.3.2 Microcompression 64

Chapter 3: *Analysis study of Fe_xN thin films and $Fe_xW_{y-1}N$ thin films* ***69***

3.1 Introduction 69
3.2 Growth of Fe_xN thin films 70
3.2.1 Growth conditions for Fe_xN with different iron (x) content 70

3.2.1.1 Surface morphology 71
3.2.1.2 Structural determination 73
3.2.2 Growth conditions for Fe_xN with different growth time 78
3.2.2.1 Surface morphology 78
3.2.2.2 Structural determination 79
3.3 Growth of $Fe_xW_{y-1}N$ thin films 87
3.3.1 Growth conditions of $Fe_xW_{y-1}N$ 87
3.3.2 Surface morphology 88
3.3.3 Structural determination by XRD and XPS 91
3.4 Discussion 94
3.5 Summary 98

Chapter 4: *Preliminary study of microcompression:MgO (100) and MgO (110) 99*

4.1 Introduction 99
4.2 Micropillar fabrications and microcompression experiment 100
4.3 Results 101
4.3.1 Microcompression of MgO (100) 101
4.3.2 Morphology of MgO (100) micropillars 106
4.3.3 Microcompression of MgO (110) 109
4.3.4 Morphology of MgO (110) micropillars 114
4.4 Discussion 118
4.5 Summary 121

Chapter 5: *Microcompression study of Fe_xN thin films on sapphire 122*

5.1 Introduction 122
5.2 Micropillar fabrications and microcompression experiment 123
5.3 Results 125
5.3.1 Microcompression of Sapphire (0001) 125
5.3.2 Morphology of Sapphire (0001) micropillars 129
5.3.3 Microcompression of Fe_xN on sapphire 133
5.3.4 Morphology of Fe_xN on sapphire micropillars 138
5.4 Discussion 143
5.5 Summary 147

Chapter 6: *Conclusions & Further Work 149*

6.1 Conclusions 149
6.2 Future work 150

References 152

Appendix A 166

This thesis is dedicated to my beloved parents and family

"When the going gets tough, the tough get going"

Abah and Mama

This is for you

Chapter 1

Introductions

1.1 Motivation

Nitrides-based materials such as titanium and chromium nitride are of interest in current research as they exhibit useful technological applications such as in microelectronics and optoelectronic devices. This is because these materials have inherent properties such as high electron conductivity, high melting point and wider band gap[28–30].

Metal nitrides-based materials (such as binary and ternary nitrides) in particular are able to exhibits interesting materials of electronic optical, thermal and magnetic properties. They can be metallic, insulating or even superconducting (TiNCl, ZrNCl and HfNCl)[31,32], with absorption/emission bands from ultraviolet (UV) to visible (GaN and AlN)[33,34]. Low to high thermal conductivity (BN)[35,36], paramagnetic to ferromagnetic (Fe_4N and $Fe_{16}N_2$)[37,38] and soft to extreme hardness (TiN and VN)[39,40].

In this project we are aiming to study the development of binary and ternary iron-based nitride thin films with a particular interest in the growth mechanisms and the Young's modulus of these materials. Before the binary nitride thin films are tested with microcompression to measure elastic modulus, a preliminary study of this method was conducted by selecting single crystal MgO as our reference material, given that its bulk deformation is well documented and has been the subject of a number of elastic measurements studies[21,22,41–43]. The aim of this preliminary study is to observe whether the elastic constant values agrees with the

literature,since the technique used for determining MgO elastic constant will later be carried out on Fe_xN thin films, where the elastic properties are unknown.

The necessary concepts required to understand this thesis will be outlined in the present chapter, and the theory and methods of the characterisation techniques used, such as atomic force microscopy (AFM), transmission electron microscopy (TEM) and X-ray diffraction (XRD), will be explained in Chapter 2. Furthermore, Chapter 3-5 will describe the growth and microstructural characterization of Iron (Fe)-based nitrides films on sapphire and their elastic modulus by using microcompression technique. Finally, Chapter 6 will summarize all results from Chapters 3-5 and discuss the work that will be undertaken in the future.

1.2 Nitrides

Nitrogen belongs to group V, but it is clearly different from other elements located in the subsequent periods, such as phosphorus and arsenic due to its higher electronegativity. The compounds of nitrogen are sometimes similar to carbides in terms of structure, physical and chemical properties and also form oxynitrides materials because nitrogen occurs after carbon and before oxygen in the second period.

Nitride chemistry has remained a relatively neglected area of research but in the past 30 to 40 years, the field has expanded as a number of new compounds and structures were discovered[44–47] . The bonding in the nitrides is largely metallic with a strong overlap between the metal atoms, while the N atoms are usually considered to occupy the interstitial sites within the metal sublattice. This has made them share similar properties with the carbides materials (TiC and WC)[48–50], which have higher hardness that leads to applications in abrasives and protective coatings[51].

1.3 Properties of metal nitrides

Most metal nitrides (i.e. FeN, GaN and BN) are metallic conductors with electronic and magnetic properties with better properties exceeding their parental metals. (Fe, Ga, B). They also possess high resistance against electrochemical corrosion and a very high cohesive strength that is responsible for their extremely high melting point, which is also reflected in extreme hardness, strength and in some cases brittleness, which makes metal nitrides typical ceramic materials[44,47,52,53].

Transition metal nitrides are formed by occupancy of nitrogen atoms into interstitial sites of metal lattice. The lattice expansion of metal will take place first before the crystal structure of the metal lattice changes to another form of crystal structure as nitrogen atom concentration increases. Nitrogen can form metal nitrides with all transition metals, except for the late elements of the second and third row because the reactions with nitrogen would not release enough lattice energy and would thus make them unstable[37].Similar to those of the pure transition metals, simple structures can be found in the early groups of the transition metal compounds. Other structures are more complicated and were systematized first by the Hägg, who stated that the geometrical rules of the atomic arrangement depend on the radius ratio:[27]

$$r = \frac{r_x}{r_m} \tag{1}$$

where r_x is the atomic radius of a non-metal and r_M is the atomic radius of a metal (Equation 1).

For r lower than 0.59 simple structures, such as face centred cubic (FCC), hexagonal close-packed (hcp) and simple hexagonal (hex), are predicted. Nonmetal ions are placed in the

interstitial sites of octahedral or cubic prismatic geometry. For r larger than 0.59 the metallic arrangement becomes distorted and more complex structures are formed.

Table 1.1 shows examples of atomic radius for transition metals. Atomic radius is inversely proportional to the effective nuclear charge. Theoretically, the nuclear effective charge increases as the element moves from left to right in the periodic table, thus decreasing the atomic radius. When this occurs, the transition metal element will have a repulsion due to the increased number of electrons in the 3d sub shell which repels to the present in the 4s electrons. The repulsion will increase the atomic radius of these elements.

Table 1.1: Atomic radius of transition metals[26].

Elements	**Atomic radius (Å)**
Iron (Fe)	1.56
Tungsten (W)	1.93
Chromium (Cr)	1.66
Copper (Cu)	1.45
Zinc (Zn)	1.42

Early transition metal compounds (groups 3 to 6) have MX or M_2X stoichiometry M_4X, where M stands for transition metals and X stands for nitride. The increased metal content in nitrides with the increasing group number means lower affinity towards nitrogen and lower stability. The high stability of the group 4 to 6 compounds is reflected in their high melting point (Table 1.2) and many of them are superior to the ceramic materials like SiC or Si_3N_4. Besides binary nitrides (MX_n) ternary ($M_IM_{II}X_n$) and quaterny ($M_IM_{II}M_{III}X_n$) nitrides are also known in the form of solid solutions where one transition metal can be randomly substituted in the lattice by the other (e.g. V_xMoN_y).

Transition-metal nitrides, commonly referred to as refractory hard metals, have both combination of physical and chemical properties, which make them attractive from both fundamental and technological points of view[54].

Table 1.2 Physical and Chemical Properties of Common Transition Metal Nitrides[27].

Group	Element	Melting Point (K)		Hardness (kg mm^{-2})	
		Metal	Nitride	Metal	Nitride
4	Ti	1933	3220 (TiN)	55	2100
5	V	2190	2619 (VN)	55	1500
	Cr	2130	2013 (Cr_2N)	230	1100
6	Mo	2883	2223 (MO_2N)	250	1700
	W	3680	873 (WN)	360	-
8	Fe	1810	943 (Fe_4N)	66	-
	Others	4073 (diamond)	2173 (Si_3N_4)	7600 (diamond)	1700 (Si_3N_4)

1.4 Layered nitrides: Binary and ternary

In general, the strong triple bond in molecular nitrogen compared to oxygen favours the decomposition of nitride into metal. However, the diversity of structures and chemical bonding in the metal nitrides are potentially richer than that of oxides and therefore nitrides are likely to serve as source of interesting new functional materials. For example, nitrides include unique crystal structures, in which several bonding types (ionic, covalent, metallic) may exist within one compound [55–57].

Much interest in nitride chemistry has been focused on the binary nitrides. These materials exhibit a wide variety of physical and chemical properties. Nonetheless, the search for new ternary transition metal nitrides, which may display a wider variety of useful properties has

only begun recently[58]. Ternary nitrides, either in solid solution as nanocomposites can form part of multilayers and super lattices which could lead to super hard coatings and controlled plasticity. Binary and ternary nitride compounds exhibit diverse and often novel crystal structures in which transition metal ions frequently display under unusual oxidation states and/or coordination to nitrogen and these are commonly lower than those seen in oxide chemistry [59].

One of the well-known binary nitrides is III-nitride alloy which usually a thin film of gallium nitride (GaN) and indium nitride (InN) which were grown on silicon or sapphire substrate. These III-nitride materials are attractive to researchers due to their potential application in light emitting diodes (LEDs), laser diodes (LDs), tandem solar cells and field effect transistors (FETs). These thin films were grown as epitaxial layers and then their properties such as semiconductor heterostructure interface are studied by measuring the mismatch of the energy level of the majority carries across the interface [57].

Gregoryanz *et al.*[60] studied a binary noble metal nitride by synthesising the platinum nitride (PtN) by laser-heated diamond anvil cell techniques. This is one of the highest pressures at which synthesis has been carried out with complete recovery of the product to ambient conditions. It was found that this compound can be formed above 45-50 GPa and temperatures exceeding 2000 K when quenched to atmospheric pressure and the temperature remained stable.

Previous research showed that many ternary nitride compounds have been prepared by pairing a transition metal with a more electropositive element, usually an alkali or alkaline and water and exhibit insulating behaviour due to poor transition metal to transition metal orbital overlap[61].

A study on the thermodynamics of formation of binary and ternary nitrides of Ce/Mn/N system was conducted by Tessier *et al.*[62]. They believed that although, the novel approaches were widely developed using solid state synthetic routes, low temperature techniques and single crystal preparations, the energetics of both these binary and ternary nitrides have not been widely explored due to the stability of dinitrogen. Two binary and a ternary nitrides which are η-Mn_3N_2, *0*-Mn_6N_5 and Ce_2MnN_3 were prepared and used a drop solution calorimetry in high temperature oxide melts to study the energetics of nitride formations due to the stronger N_2 triple bond compared to the O_2 double bond (as mentioned in earlier topic). However, when compared between binary and ternary nitrides, the results show the role of inductive effects in Ce_3MnN_3 leading to a higher energetics stability compared to binary component.

1.5 Challenges with ternary nitrides growth

Ternary nitrides have become of interest recently due the higher order nitride compounds being expected to display different and/or complex crystal structures with exotic magnetic, optical and electrical properties in comparison to the binary nitrides.

Although ternary nitrides have many advantages in both electronic and mechanical properties, numerous challenges in their growth remain. For a long time, little progress was made in the synthesis of the ternary nitrides more complex than binary because of the difficulties to synthesise them in practice. One of the reasons is due to the unique chemistry of nitrogen which presents itself in the preparation of these nitrides.

The diffusion rate of nitrogen in many materials is slow; consequently, high temperatures are often required for reasonable reaction rates. Furthermore, the greater strength of nitrogen triple bond in N_2 (941 kJ mol^{-1}) in comparison to the strength of the oxygen double bond in O_2 (500 kJ mol^{-1}) results in lower free energies of formation and lower thermodynamic stability of

nitrides at elevated temperatures. Nonetheless, the study of new ternary nitrides which may display a wider variety of useful properties, has begun only recently when new synthesis strategies have been developed [61].

As compared to oxygen or to halogens, the N_2 molecule has great stability and is less reactive. The direct reaction with nitrogen is difficult, due to, among other reasons, enthalpy of dissociation, which is about two times larger than the O_2 molecule which is about 226 kcal mol^{-1}. This implies that the reactions of nitriding occur generally in high temperature reactions and that they often involve nitrogen containing species i.e ammonia, which are more reactive than molecular nitrogen [55].

It is also known that the crystal structure of the ternary nitrides consists of mostly hexagonal structures. This limits the choice of substrates for ternary nitrides growth to those substrates which are stable at higher temperatures. Sapphire, silicon and carbides are the three most commonly used substrates. Silicon carbide is expensive compared to silicon or sapphire, which will then limit its use to high power applications devices only.

The orientation of a film is controlled by the interaction with substrates, and by the kinetics of the growth process resulting from different growth rates of different crystal faces. Unlike silicon, [0001] sapphire crystal structure has the same type of crystal structure of iron nitrides, which is hexagonal. Therefore, when both films and substrates possess similar crystal structure the interaction between film and substrate interaction has been found to be none or very weak, which give rise to a good quality of interface[63].

A study conducted by Lei and Ludwig[64] on GaN thin films on both silicon and sapphire substrates found that a higher inhomogeneous strain occurred in the thin film on the silicon substrates and the lattice mismatch is around 21 %, while thin films grown on sapphire orient

themselves to match the bulk atomic positions of the film and substrates thus decreasing the effective lattice mismatch below values for epitaxy on silicon substrates.

Wickenden *et al.*[65] also supported this study by stating that for the growth of hexagonal thin films on the c plane sapphire (which is [0001]), the mismatch between the substrate and films is not more than 0.7 % approximately. One of the reasons is because the relatively small in and out of plane misorientation and little secondary phase occurred on the GaN thin films grown on sapphire. Stacking faults on GaN thin films despite it was grown on sapphire or silicon is common due to carrier mobility of atoms.

In contrast, although Si (111) is inexpensive, the large lattice mismatch between the thin film and Si results in film cracking which reduces the quality of the films. Therefore, sapphire is the favoured substrate because of its stability at high temperatures, ease of handling, optical transparency, wide availability, simple pregrowth cleaning requirements and low costs. Therefore, ternary nitride thin films are commonly grown on the (0001) basal plane of sapphire, as epitaxy layers, and by high-temperature processes such as electron beam epitaxy (EBE).

Layered ternary nitrides broadly follow two patterns in terms of their crystal chemistry where knowledge of relatively well characterised analogues (chiefly from oxide chemistry) or parent system can be used to predict the structure of the material and begin the modification and manipulation of the composition, structure and also their physical properties of potential materials [66].

1.5.1 3D layered nitrides

It is of interest to explore nitride systems in which the ratio of the main groupof metal and the transition metal elements is low (≤1). As the amount of electropositive metal decreases, there is a tendency to a greater connectivity of the transition metal-nitrogen polyhedral. The

enhanced metal orbital overlaps should yield a greater degree of covalency in bonding and result in more stable and robust compounds[59,66].

For example, MAX *n*-phases (*n* = 1,2, or 3), are a class of ductile inherently nanolaminated ternary nitrides and carbides, including 60 known phases[67]. In these phases, M is an early transition metal, A is an A group (mostly IIIA and IVA, or group 13 and 14) and X is either nitrogen or carbon. They were initially discovered and their crystallographic structure was determined by Hogberg *et al.*[1]. However, there is increasing interest in the field today. This interest in the MAX-phases, as reflected by an increasing number of experimental and theoretical studies, is largely motivated by the unusual combination of metallic and ceramic properties.

These properties are typically shared by the other MAX-phases and came from the highly anisotropic hexagonal crystal structure in which the early transition metal atoms and the carbon and/or nitrogen atoms form octahedral edge sharing building (MX) blocks interleaved by pure A-element layers as shown in Figure 1. Due to three different stacking sequences of the MX block between each neighbouring A-element layers, the MAX-phases are known in three subgroups with the stoichiometry's M_2AX, M_3AX_2 and M_4AX_3.

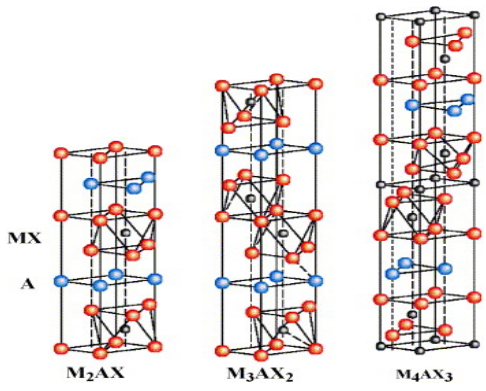


Figure 1.1: From Hogbert*et al.*[1] The hexagonal crystal structures for the $M_{n+1}AXn$ phases (n = 1,2 or 3), showing the different stacking in the existing subgroups of the compositions M_2AX, M_3AX_2 and M_4AX_3 .

Since in this project, we are interested in the development of thin films, besides characterisation, the mechanical property of this film is also investigated with a microcompression test in order to compare the thin film's elastic modulus value to the bulk sample's which is available from other references. The fundamental difference between most bulk synthesis methods and the thin film synthesis is that the bulk syntheses are assumed to operate relatively close to thermodynamic equilibrium, while the latter proceeds far from thermodynamic equilibrium. There are few well known methods to the synthesis of thin films i.e; physical vapour deposition (PVD), chemical vapour deposition, CVD and solid-state reaction. Methods like CVD and solid-state reaction is documented to be similar to bulk synthesis method compared to the PVD.

The difference in the thermodynamic equilibrium is crucial in the thin film synthesis because energy can be provided to the growing film by means other than temperature, i.e; by an energetic growth flux or ion bombardment. For MAX phase, this route offers beneficial outcomes such as (i) it is possible to reduce the synthesis temperature of MAX phases substantially and (ii) it gives opportunity of metastable phases growth possible although ion bombardment may have competing detrimental effects [67].

Ternary layered nitrides can also be synthesised and commonly have the formula of ABN_2; where A is an alkali, main group or transition metal; B represents a transition metal while N is nitrogen. Their crystal structure is layered but their electronic properties may have either 2D or 3D character. Ternary nitrides of stoichiometry ABN_2 crystallise in a variety of different structures. This stoichiometry is relatively well documented for ternary alkali metal nitrides, and the majority of group 1a transition metal nitrides form layered structures similar to those seen in ternary oxide and chalcogenide chemistry. For example, $LiMN_2$ are hexagonal layered compounds with M = Mo or W coordinated to six nitrogen atoms in a trigonal coordination[68]. These nitrides are reported to be metallic in nature mixed transition metal nitrides such as

$FeWN_2$ (which will be considered in this project), is a layered material similar in structure to $LiMoN_2$ with alternating layers of A-N octahedral and B-N trigonal prism[69,70]

The ABN_2 class consists mainly of 2D layered type compounds with a hexagonal crystal structure, although the nature of the layers and the pattern in which the layers stack vary with cation size and transition metal type. Usually, these type of nitrides (ABN_2) contain six-fold coordinated metal atoms in either octahedral or trigonal prismatic geometry. These structures often differ, principally, in terms of their layer stacking sequence.

However, some ABN_2 compounds do not have hexagonal crystal structures, e.g. when the 'A' element has a higher atomic number. The compounds $KTaN_2$ and $RbTaN_2$ for instance formed orthorhombic structures apparently similar to metal oxides such as $KGaO_2$. Meanwhile, $CsTaN_2$ prepared under similar conditions crystallises with the cubic crystallite structure and at ambient pressure, $KTaN_2$ and $KNbN_2$ are reported to form cubic structures which may be analogous to $CsTaN_2$[71]

Also, some ternary nitrides are not layered, for example a study conducted by Matenoglou *et al.*[72]on structure and bonding in TI based ternary transition metal nitrides showed when it is mixed with/or Zr, Hf, Nb, Ta, and Mo, the rock-salt structure is stable while the compounds exhibit covalent like bonding and have high hardness and strength, and yet are also good conductors of heat and electricity.

In summary, the motivation for developing new nitride materials with layered crystal structures in 3D thin film form is to discover new materials which may have improved stability, increased hardness, improved temperature stability, improved diffusion barrier properties and/or improved conductivity for use in hard coatings or in electronic device applications.

1.5.2 2D layered nitrides

The same chemical compound can exhibit different properties depending on whether it is arranged in a characteristically 1D, 2D or 3D crystal structure. Most crystal structures are 3D, but there are some 2D layered crystal structures among experimentally known crystals. These materials typically are strong in plane bonds and have weak van der Waals like coupling between layers. Because of their layered structure, it has long been tempting to try splitting such materials into individual atomically thin 2D layers, although it remains unclear whether free standing atomic layers could exist. Thus far, most efforts have focused on chemical exfoliation of strongly layered materials and in particular stage I intercalated ones, like previous research on graphite [73].

For example, graphene is the most famous 2D atomically thin material, which may allow applications in transistors, sensors and other devices [74]. Another layered material is boron nitride (BN). Pairs of boron and nitrogen atoms are isoelectronic to pairs of carbon atoms. Thus, boron nitride and diamond are like cubic boron nitride. However, the polar bonding in 2D atomically thin *h*-BN leads to the presence of a wide electronic band gap compared to its isoelectronic analogue graphene. BN provides excellent protection against oxidation and wear and is electrically insulating. Therefore, magnetic articles coated with BN would have significant advantages for technological application [75–77]. It is also useful in combination with graphene as an insulating layer in electronic devices based on 2D materials.

Geim and Grigorieva[2] discussed extending the range of known Van der Waals heterostructures from graphene and BN to include other two dimensional (2D) atomic crystals such as molybdenum disulphide (MoS_2), and other dichalcogenides. These materials are of interest for light emitting diodes (LED), high mobility transistors and semiconductors. These can be used to make heterostructures and devices by stacking different 2D crystals on top of each other. The resulting stack represents an artificial material assembled in a chosen sequence as shown

in Figure 1.2. Strong covalent bonds provided in plane stability 2D crystals, whereas relatively weak, van der Waals forces are sufficient to keep the stack together. The possibility of making multilayer van der Waals heterostructures has been demonstrated experimentally only recently. Most importantly, it turned out that in practice this atomic scale works exceptionally well.

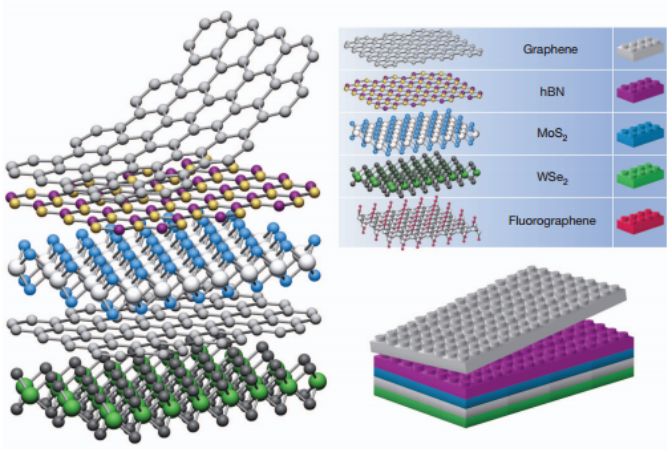


Figure 1.2. From Geim and Grigorieva[2]. Building van der Waals heterostructures where a monolayer is place on top of other monolayer or few crystals and add another 2D crystal.

According to Yamanaka [32] one of the most fascinating characteristics of layer structured crystal will be the potentially of intercalation. In layer structured crystals, the chemical bonds within the 2D layers are relatively strong, whereas the interlayer interaction is mainly due to Van der Waals, or weak ionic bonding; thus, in some crystals various guest species can be intercalated into the gap between the layers.

1.6 Nitrides of interest in this work

The following nitrides were selected for synthesis as (i) previous work had indicated that these nitrides are stable with respect to oxidation in air,(ii) these materials were potentially suitable as candidates for testing possible nitride synthesis routes, (iii) their electronic properties are of interest but have not yet been well characterised. Essentially, these are the ‘prototype’ layered

nitrides, from which future layered nitrides may be derived for use in coatings and/or electronic devices.

1.6.1 Iron based nitrides material

Iron nitrides (Fe-N) have been attracting scientific and technological interest over the past few decades. Their ability to improve surface hardness and wear resistance makes them popular and recently the iron nitride films have been widely investigated due to various crystallographic phases and interesting magnetic properties.

The iron nitride phase diagrams provide thermodynamics information of these phases based on the crystal lattice and based on this phase diagrams the modes of growth for iron nitrides thin films are developed. The phase diagram of Fe_xN has been studied by the classic work of Jack[78] and Wriedt *et al.*[3] which is presented in Figure 1.3. Depending on the temperature and concentration of nitrogen diffused into the ferrite, a number of phases may form. Most ordered nitrides of Fe are based on close packed iron structures. For example, Fe_4N may be seen in face centred cubic (fcc) iron, where ¼ of all octahedral sited are occupied by nitrogen where the octahedral share corners only. Meanwhile for Fe_3N is based on the hexagonal close packed (hcp) where 1/3 of the octahedral sites is being filled by nitrogen[79].

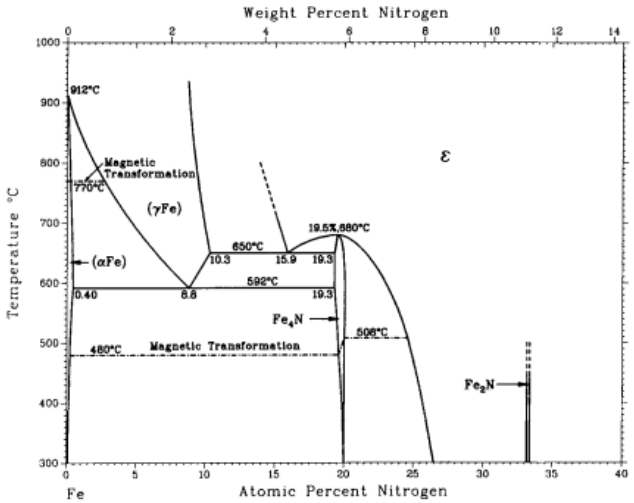


Figure 1.3: Fe-N phase diagram[3].

One of the most studied iron nitride compounds is $Fe_{16}N_2$ as it has a giant magnetic moment where it is an intermediate phase which forms when γ'-Fe_4N is being synthesised, meanwhile the Fe_3N_4 phase has been predicted theoretically but has not yet been observed experimentally. All ordered iron nitrides are metastable compounds, which can persist at moderate temperatures because of kinetic constraints. Therefore, phases which are related like α, γ and εFe will arise from Fe-N. and other extended phases, including the α''$Fe_{16}N_2$, γ'-Fe_4N, ε-Fe_3N, ξ-Fe_2N and α'-FeN phases in the order of increasing nitrogen content. $Fe_{16}N_2$, Fe_4N, Fe_3N are magnetic while Fe_2N and FeN are non-magnetic [80,81,90,82–89] .

There has been growing interest in studying the nitride phase evolution of Fe-N thin films grown on various single-crystal Si (100)[91], MgO (001)[92] and $SrTiO_3$ (100)[93] substrates. The selection of an appropriate deposition temperature and the amount of nitrogen concentration plays a major role in the nitrogen ordering and the structural phase of the thin films.

Various preparation techniques have been used to synthesize the Fe-N thin films, such as the molecular beam epitaxy [94], ion implantation [95], gas nitriding [96] and chemical vapour deposition [97]. Many earlier attempts reported in the literature have failed to produce the Fe-N thin films or an individual iron-nitride phase due to the lack of sufficient thermal activation energy and the poor nitrogen ordering.

One of the widely studied Fe-N materials is γ'-Fe_4N, given its simple composition and crystal structure. In the early years of its development, the synthesis and study of γ'-Fe_4N was motivated by its possible application as a catalyst for the production of ammonia and surface treatment of steels with ammonia [98] until it was discovered that γ'-Fe_4N has the potential as a material for high density magnetic recording and was studied due to its high magnetic flux density, low coactivity, low resistance and other properties. The simple unit cell of γ'-Fe_4N makes it a suitable candidate for the first generation of the ab initio methods [88,99,100]

Figure 1.4 shows the phase diagram summary of nitrogen radical source in a thin film which was grown by molecular beam epitaxy (MBE). The thin film phase diagram almost reproduces the thermodynamic equilibrium state when the samples are grown at 200°C. The diagram is dominated by α-Fe with N interstitial when it comes to low nitrogen content. There is a coexistence region of -Fe, α'-Fe_8N, γ'-Fe_4N and ε-Fe_3N on the nitrogen content of more than 12.5 %. The diagram also shows that the growth window of γ'-Fe_4N is larger than expected where a needle shaped region was formed around the optimal nitrogen content of 20%. A pure sample of γ'-Fe_4N is obtained in higher temperatures and at lower temperatures in a very narrow range growth parameters [4].

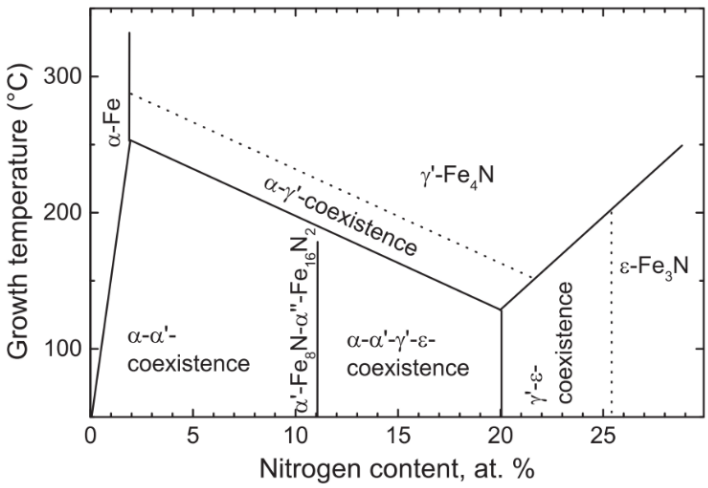


Figure 1.4: From Gölden *et al.*[4]. Thin film phase diagram of the iron nitride system. Thin films were grown by MBE.

Rissanen *et al.*[101] synthesised nitrogen rich thin films of FeN_x by reactive magnetron sputtering and studied the effect of deposition parameters, gas mixture, and pressure and substrate temperature on thin films. It was found that the phase structure is very sensitive to the pressure and the N_2 and Ar flows. It is also very hard to get a pure phase of FeN although 27 sccm of Ar_2 and 30 sccm of N_2 succeeded in producing films consisting about 90 % of FeN. Impurities

was the main concern in the Ar and N_2 gas flows which occurred due to sputtering chamber walls being heated and impurities condensed and vaporized into the plasma.

A study conducted by Babu *et al.*[102] on the effect of thickness on structural and magnetic properties in nanocrystal Fe-N thin films shows that the Fe-N thin films exhibit a structural transformation from -Fe_3N to y'-Fe_4N phase with the increasing film thickness. The smaller Fe-N grains and large strain exhibit more domain wall motion; therefore, the films exhibit and increase in coercivity (the ability of ferromagnetic material to withstand external magnetic field without becoming demagnetised) with decreasing thickness.

The AFM images of surface morphology of the thin films on Si (100) with thicknesses t = 40, 80,160 and 240 nm are shown in Figure 1.5. The *rms* roughness of the films was observed to decrease with the increasing thickness. The in-plane grain size is larger than the thickness in the thinnest ε-Fe_3N film. Nearly spherical shaped grains can be seen on the other films as their grain size becomes smaller than the thickness.

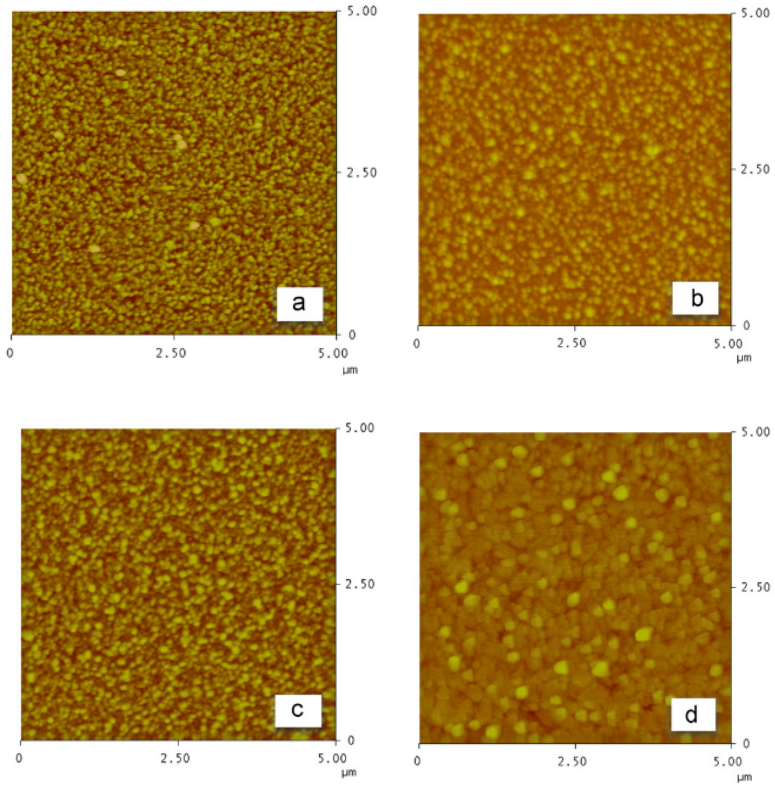


Figure 1.5: From Babu *et al.*[5]. AFM images of Fe-N on Si (100) films of (a) t = 40 nm, (b) t = 80 nm, (c) t = 160 nm and (d) t = 240 nm.

1.6.2 Iron tungsten nitrides material

Many new and structurally diverse ternary metal nitrides have been discovered in recent years [103]. In recent years ternary nitrides containing two transition metals have raised a lot of interest especially after $FeWN_2$ was reported in 1993. $FeWN_2$ is stable in air and moisture and does not dissolve in acids and bases, which makes it easier to synthesise [6,29,104].

In early years of the ternary nitrides development, synthesis routes that were used were nitridation of intermetallic compounds, solid state reaction between two metal compounds and ammonia or nitrogen, and mechanical comminution of the binary nitrides in a high temperature atmosphere of ammonia or nitrogen.

One of the earliest techniques of the $FeWN_2$ synthesis is by ammonolysis using the solid state oxide precursors where $FeWO_4$ was placed into an aluminium boat and heated under flowing

ammonia in order to obtain $FeWN_2$. During those years, nitrides are not usually synthesised directly but rather by converting one nitride into another. The sample of $FeWN_2$ was heated at 800ºC and held for 12 hours in the reaction temperature before quenching took place [6]. The black product, $FeWN_2$ was indexed by X-ray powder diffraction shown in Figure 1.6 and has a hexagonal structure similar to the known nitrides $LiMoN_2$ and $CuTaN_2$ with the space group of $P6_3/mmc$[6,29].

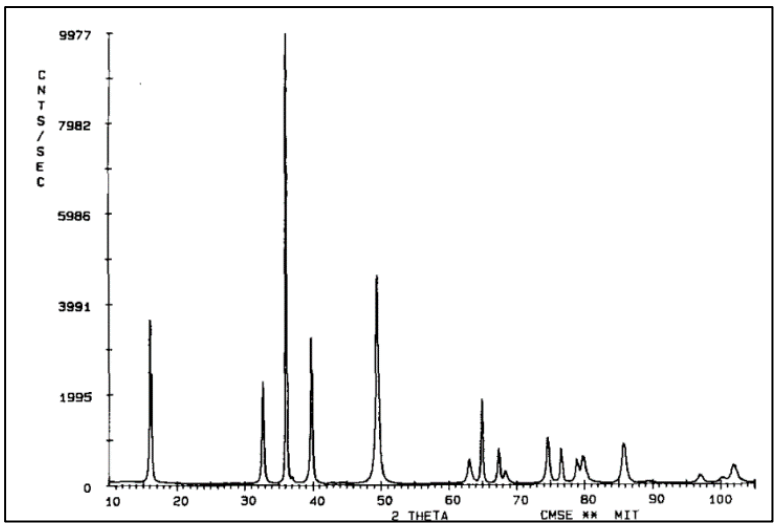


Figure 1.6: From Bem *et al.*[6] , XRD pattern of $FeWN_2$.

$FeWN_2$ is a layered nitride, consisting of alternating W-N prismatic layers and Fe. The layer stacking is AcAc'BcBc'A, where capital letters represent a close packed nitrogen layer, lower case letters are close packed W layers and primed lower-case letters are Fe layers. Figure 1.7 shows $FeWN_2$ structure.

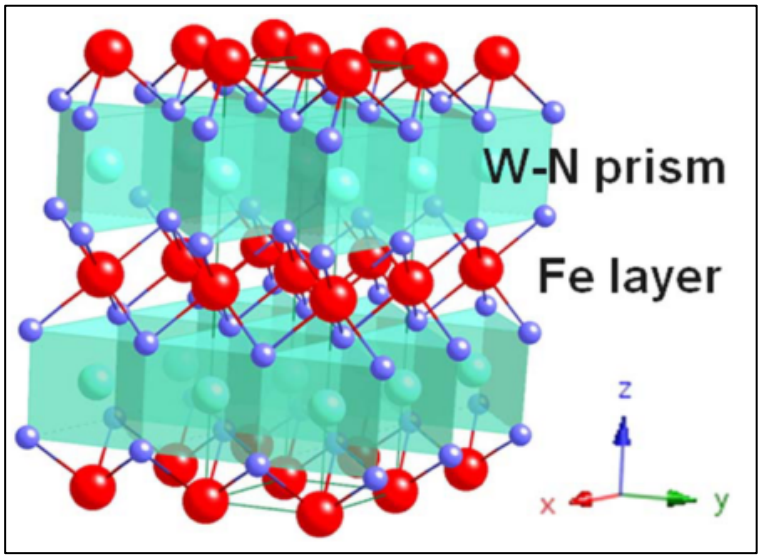


Figure 1.7: From Miura *et al.*[7]. Crystal structure of $FeWN_2$. Trigonal prismatic tungsten layers are shown as filled polyhedral. The iron and nitrogen positions are indicated in a ball and stick representation. Large and small balls represent iron and nitrogen, respectively.

Weil and Kumta[8] synthesised $FeWN_2$ and other ternary nitrides (Fe_3MoN, Ni_3MoN and Ti_3AlN) by using chemically complexed precursors. One of the reasons is that the normal approach from previous researchers require either prolonged heat treatments or a combination of long soak times at high temperatures. Besides, the reaction with the crucible as well as compositional inhomogeneities leads to problems like contamination which will then affect the properties and applications in which these materials could potentially be used.

Figure 1.8 shows the morphologies of the powders synthesised by the chemical complexed precursor's technique. From the scanning electron (SEM) images, it shows that Fe-W-N shows roughly spherical particles that aresubmicrometers in size. The powder was then converted to single phase ternary nitrides by heating it at 950°C for 4 hours. The end product results in, $FeWN_2$, Ni_3Mo_3N and produced a very fine crystalline materials [8,105].

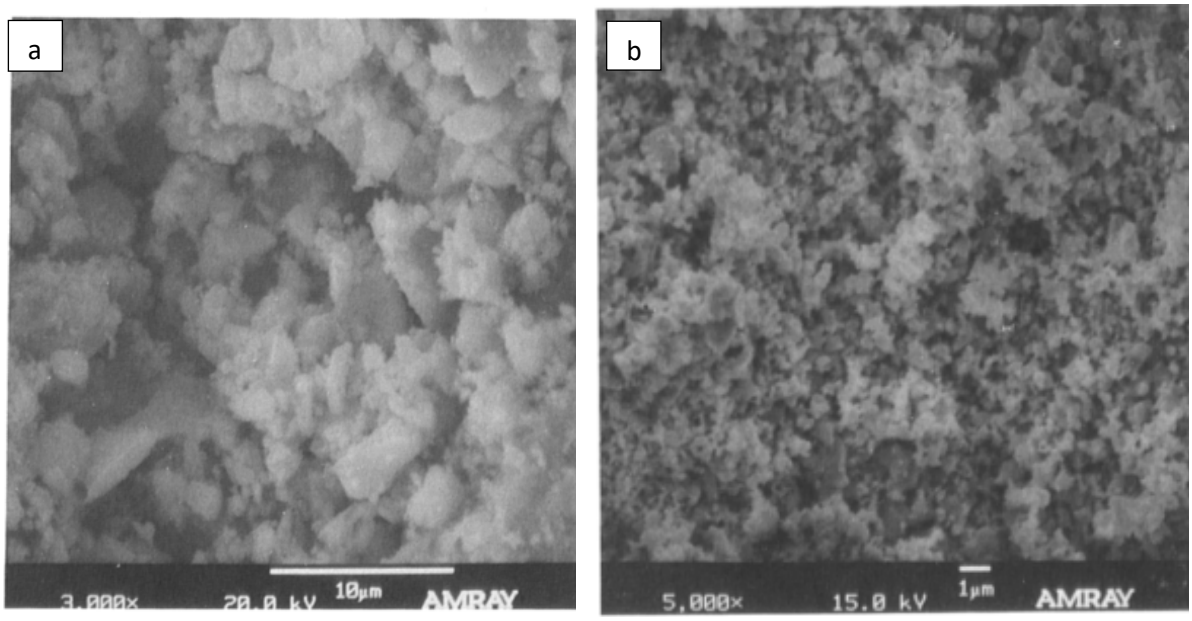


Figure 1.8: From Weil and Kumta[8]. SEM images showing the microstructure of (a) as dried precursors of Fe-W-N and (b) as heat treated at 950°C for 4 h in ammonia $FeWN_2$.

1.7 Elastic modulus measurements

1.7.1 Introduction

The elastic constants of a material can be described as the resistance to deformation by an externally applied stress and they provide useful information about bonding stability and structural stability[106]. Elastic constants include the bulk modulus, Poisson's ratio, shear modulus and Young's modulus as summarised in Table 1.3 They are important for understanding the response of materials loaded in the elastic regime.

Among all the material properties, Young's modulus is one of the most influential factors in the development of thin film technology. Young's modulus which is also referred to as elastic modulus or modulus of elasticity is the ratio of stress to strain and is equal to the slope of a stress strain diagram for the material[107]. For example, a study on the elasticity of $Pb(Zr,Ti)O_3$[108]reported that the large anisotropy in Young's modulus in their materials has

helped them to study the piezoelectric coefficient as it is related to the mechanical state of the material.

Another method that is widely used to calculate elastic constants is density functional theory (DFT). DFT is a very successful theory that makes it possible to evaluate many physical properties of materials accurately and efficiently. A study conducted by Bannikov *et al.*[109] on elastic structure, chemical bonding and elastic properties of $TaThN_3$ compared the Young's modulus of ternary and binary nitrides between $TaThN_3$ and TaN. It was reported that TH mononitride in ternary nitrides is less resistant to shear deformation which lead to decreasing Young's modulus from binary to ternary nitrides. One of the reasons is the increase of lattice constant in the cubic Th-containing nitride. Thus, the $TaThN_3$ exhibits a higher hardness compare to its binary compound.

A modelling technique to study the elastic properties and electronic band structure was conducted by Mattesini and Mater[110] by the ab initio calculations for the cubic SC_3EN (E= Al, Ga, In). The obtained elastic constants which was carried out by the augmented plane wave local orbital method were used to estimate their mechanical stability with the affluence of the stiffness of Sc-based ternary nitrides.

Table 1.3: Properties of Elastic Constants

Properties	Definition	Equations	Units
Young's Modulus (E)	Quantifies the resistance of a solid to a change in its length	$\frac{F/A}{\Delta L/L}$ Where, F = Load A = Area ΔL = Change in length L = Original length	N/mm^2
Poisson Ratio (v)	The ratio of transverse contraction strain to longitudinal extension strain in the direction of stretching forces	$\frac{\Delta x/x}{\Delta y/y}$ Where, x = Transverse strain y = Axial strain	-
Shear Modulus (g)	Quantifies the resistance to motion of the planes of a solid sliding past each other under shear stress	$\frac{F/A}{\Delta x/h}$ Where, Δx = Horizontal distance that the sheared face moves h = Height of the object	N/mm^2
Bulk Modulus (B)	Quantifies the resistance of solids or liquids to changes in their volume	$\frac{\Delta P}{\Delta V/V}$ Where, ΔP = Change amount of pressure ΔV = Change amount of volume	N/mm^2

1.7.2 Experimental techniques of elastic constant measurements

Considering the importance of elastic properties of materials for design and engineering applications, it is not surprising that a great number of experimental techniques have been developed to determine them. There are two different experimental techniques commonly used in the past for determining the elastic constants, namely resonant ultrasound spectroscopy (RUS) and nanoindentation.

Resonant ultrasound spectroscopy is a technique based on measuring the mechanical resonance spectrum for a sample of known geometry, dimensions and mass. It is known that the mechanical resonance frequencies of a freely suspended solid object are the special solutions to the equation of motion, which depend on shape of the object. In this technique, an elastic wave constant is generated by transmitting a transducer whereas the other two transducers are used to detect resonance. The spectrum obtained cannot be deconvolved to deduce the elastic constants. Instead, an approximate spectrum is calculated from the known sample dimensions, density and a set of reference elastic constants[111,112].

A study on resonant ultrasound resonance on aluminium/sapphire samples of a low thickness reported that the elastic modulus of aluminium decreases from 230 GPa to about 137 GPa. Another experiment of RUS technique of a small sample was carried out on AlCuLi. However, the precision of elastic was not as expected compared to the bigger size of AlCuLi because small AlCuLi developed brittle nature, while excessive pressure in the RUS technique caused fracture of the samples[112–114].

The second commonly used technique is nanoindentation which is conducted by determining the mechanical properties of materials during indentation (i.e Young's modulus and hardness). To perform the measurement, the first step involves establishing an equivalence between the depth of penetration of the indenter geometry and the corresponding cross-sectional area.

Previously, the contact area between the indenter and sample surface was measured by the direct observation of the hardness impressions because imaging very small indentations is both difficult and time consuming. Therefore, Oliver and Pharr suggested a method of measuring elastic modulus and hardness by measuring their indentation load-displacement curves with information about the indenter geometry compared to the previous technique. By using this method, the penetration depth of the indenter, the applied load and the elastic response of the materials are calculated from the load and displacement in order to obtain hardness and Young's modulus.

Based on the previous research, when an indenter makes a contact with a sample surface, this indenter will usually produce a large impression radius than the radius of the indenters. This is similar to both the spherical and conical indenters. This is because during indentation loading, the indenter sinks into the sample, leading to elastic, and then followed by plastic deformation of the specimen surface. However, during unloading, it is assumed that only the vertical elastic displacement recovers, leaving a permanent impression in the material surface. The unloading curve represents Hooke's law, which corresponds to elastic recovery at a stage during which diamond indenter is in constant contact area with the material and it was assumed linear as shown in Figure 1.9.

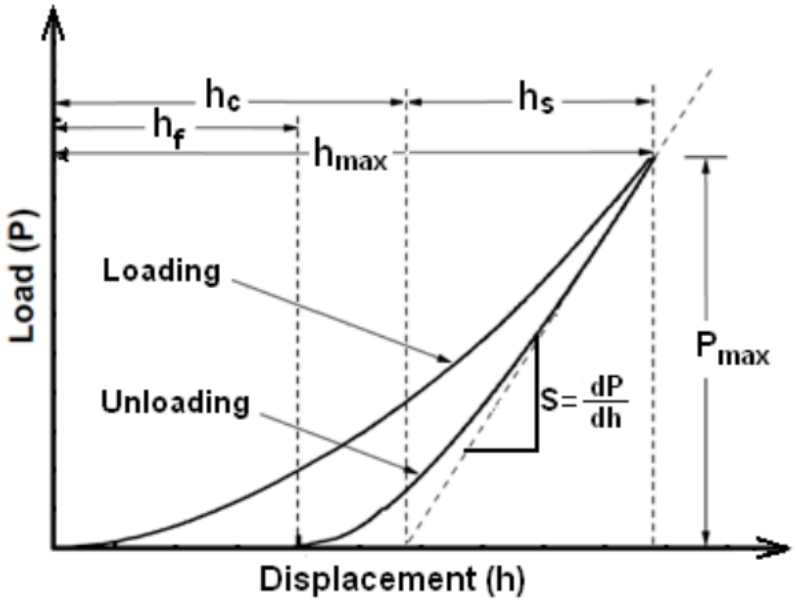


Figure 1.9: Typical load-displacement curve obtained from an instrumented nanoindentation experiment performed with a Berkovich indenter, showing important analysis performances[9].

However, Oliver and Pharr[115] showed that the unloading curve is not linear even in the initial stages. And its deviation from linearity should be accounted for. The unloading curve was fitted to a power low and the initial unloading lope could be determined by analytically differentiating this power low and evaluating the derivative at the maximum load/displacement points.

In order to get hardness of the indentation sample, the elastic modulus must be measured first. There are few things to take into considerations which are the depth of the impression made by a conical indenter recovers during unloading, the diameter of the contact impression in the surface remains constant and the contribution from non-rigid indenters on the load-displacement behaviour can be effectively accounted for by the defining a reduced modulus, E_r;

$$\frac{1}{E_r} = \frac{1-v^2}{E} + \frac{1-v_i^2}{E_i} \tag{2}$$

Where E and E_i are the elastic moduli of the specimen and the diamond indenter; v, v_i are the Poisson's ratio of the specimen and the diamond. In order to determine the elastic modulus of the tested material (E) from this equation, v is presumed to be known and E_r has to be determined. The elastic plastic response of the indented material coupled with a functional relationship between the displacement of the indenter and the contact area, make possible the calculation of hardness and the elastic modulus. The data is analysed according to the following equations:

$$S = \frac{dP}{dH} = \beta \frac{2}{\sqrt{\Pi}} E_r \sqrt{A} \tag{3}$$

Where S is the unloading stiffness which is defined as the slope of the initial protion of the unloading curve; P is the applied load, h is the indentation depth at P load, A is the projected contact area between the indenter and the specimen, and ß is a parameter which accounts for the deviation in stiffness corresponding to various indenter geometries. The unloading stiffness and contact area must be determined in order to calculate E_r.

Previously, Doerner and Nix[116] proposed a linear fit for the unloading curve to determine the stiffness when a cylindrical punch indenter is used. However, Oliver and Pharr observed that the unlading response during indentations made by sharp tip self similar (conical/pyramidal) indenters is rather well described by the power law relation which is

$$P = a(h - h_f)^m \tag{4}$$

Where, h_f is the final residual depth of the indent impression. α and m are fitting constant and are determined by a least squared fitting exercise, which implies an initial guess for α, m and

h_f. The obtained relationship can be differentiated to obtain the initial unloading slope (stiffness). Meanwhile, the contact area represents the cross-sectional area of the indenter as a function of the distance from its tip is given by

$$A = F(h_c) \tag{5}$$

Where h_c is the contact depth between the indenter and the material. The function F is experimentally determined before or after experiment and it accounts for the deviations from the ideal Berkovich indenter. Unlike pyramidal geometries, the indenter sides tend to coverage towards a line, meanwhile the Berkovich indenter is more suited for the construction of a single point vertex[117]. Some geometric considerations should be taken on the Berkovich geometry where the relationship between the diamond area function (DAF), or depth (equivalent to the contact depth, h_c) to cross sectional area should be considered. From there, it is possible to find the relationship between b and h_c, c and d (Figure 1.10) and results in equations as below

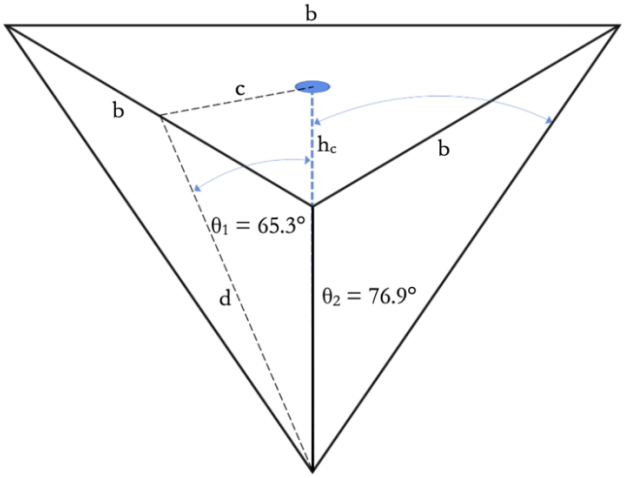


Figure 1.10: Adapted from Tommaso[10] where the Berkovich indenter geometry (not to scale) and θ_1 is the angle between the central axis and the pyramid face and θ_2 is the angle between the central axis and the pyramid's edge.

$$A = \frac{\sqrt{3}}{4} b^2 \tag{6}$$

$$h_c = \cos 65.3° d \tag{7}$$

Where d is equivalent to

$$d = \frac{c}{\sin 65.3°} \tag{8}$$

Where c is equivalent to

$$c = \frac{\tan 30°}{b} \quad b = \frac{\sqrt{3}}{6} b \tag{9}$$

Thus given d;

$$d = \frac{b}{2\sqrt{3} \sin 65.3°} \tag{10}$$

Hence a relationship between b and h_c can be found as;

$$b = 2\sqrt{3} \tan 65.3° h_c \tag{11}$$

Therefore, combining Equation 1.5 and Equation 1.10 gives Equation 1.1, where for an ideal Berkovich pyramid geometry, this relation is described by the following equation where

$$A = 24.56 h_c^2 \tag{12}$$

Where h_c is the depth of contact and A is the projected area of the contact (Figure 1.9). Additional terms need to be added in this equation to keep tip rounding and other damage into consideration.

Every indentation test starts after the indenter makes contact with the surface of the specimen. The first step in the determination of a reliable indentation stress-strain curve from the measured load-displacement data is an accurate estimation of the point of effective initial contact, where the initial contact force (which is the minimum force detected by instrument)

will cause the indenter to penetrate slightly into the specimen, and the penetration was not measured by the instrument, if the tip is very sharp. The initial penetration depth is very small and can usually be neglected by large indents.

One way to determine the initial penetration is by fitting a suitable regression curve to a number of initial points of the load displacement curve and extrapolating it to zero load. However, for indents of around tens of nanometer depth the inaccuracy of surface detection becomes significant and should be taken into account.

Furthermore, the deflection of the surface during indentation should also be considered although the sample surface is flat. This is because the contact area depends not only on the shape of the indenter but also on the elastic response of the material indented. Pile up behavior usually occur when there is a displacement of volume of material by the indenter that pushes out to the side of the indenter. This will cause an increase in contact height above the sample surface. However, regions without uplift case occurred at some unaccounted area of contact supporting the load and a contact depth smaller than it would be. As for the pile up effect, it is rather difficult to determine without a priori knowledge of the mechanical properties and work hardening behaviour of the material.

For soft thin films on hard substrates (i.e. Al on sapphire), when penetration occurs, the film may be pushed upwards and experience the “pile up” effect. However, if nanoindentation is conducted on a hard film on a soft substrate (i.e. Al on glass), the “sink in” effect will take place. Both of these will lead to overestimation and underestimation of the modulus results. According to Cripps[118], the “pile up” effect occurs because the sample appears to be in a higher modulus and harder than it actually is because more material is supporting the indenter load and the depth of the penetration for a given contact area is lower, thus giving an overestimated result.

A previous study of performing nanoindentation on ZiF thin films with thicknesses between 200 to 500 nm were reported and it was found that these thin films with different thicknesses were experiencing a sink in effect which leads to overestimation/underestimation moduli data when compared to their bulk samples[119]. The same trend was also observed in nanoindentation of aluminium and tungsten thin films demonstrated by Saha and Nix[23]. The elastic modulus is highly affected by the substrate effect because the elastic field under the indenter is not confined to the thin film itself, rather, it is a long range of field that extends into the substrate especially in the films with small thickness which makes it difficult to estimate the film modulus from the nanoindentation data only.

Therefore, the 10 % rule of sample thickness is the rule of thumb when conducting nanoindentation on thin films to avoid the above issues. It is also risky to perform such a test on the thickness of less than 1 μm because that means the indent should be performed at a 100 nm and this will make the calibrations for the tip are very difficult to do. Besides that, not only will it introduce pile up or sink in of the film during indentation, but it will also introduce the substrate effect which makes the data unreproducible and inaccurate. Furthermore, the interpretation of nanoindentation data is usually carried out using the Oliver and Pharr method, in which the projected contact area between the indenter tip and the material is estimated using the equations for the elastic contact of an indenter of an arbitrary shape on a uniform and isotropic half space[120] (which already explained above).

However, this method is only applied by conditions where both film/substrate should not have a large difference in modulus due to the substrate modulus also contributing to the measured elastic contact modulus, while its influence on the contact modulus increases as the depth of indentation increases. The consequence is wrong modulus results of the thin films[121,122].

Despite the popularity of the nanoindentation technique, there are still some intrinsic shortcomings, especially when it involves thin films. One of them is the complex stress-strain field underneath the indenter on the specific geometry tip during nanoindentation. There are two major difficulties encountered by nanoindentation of thin films which are (i) the thickness of the thin films and (ii) it is rather difficult to isolate a particular modulus when performing nanoindentation on thin films, especially in single crystals with different orientations.

Another issue with nanoindentation is isolating particular moduli especially in a single crystal. This is because, when the material is subjected to this test, the nature of loading during the test is a complex mixture of hydrostatic compression, tension and shear which results in the modulus properties of a material being independent from all three of these types of materials response. This is proven by the Hong et al.[123] study where obtaining elastic modulus for copper thin films from a parallel direction requires the micro cantilever bending test whereas, for perpendicular direction, nanoindentation was performed on it. This is because it is difficult to extract one particular modulus from the material[124].

Some of the material properties change drastically when the dimensions sample decreases. In a nanoindentation test, especially in a single crystal material when it is subjected to an indentation depth of less than 1 μm. This is because, when a single crystal is under nanoindentation, there is a relatively small, well-defined region beneath the indenter tip where dislocation nucleation is likely to occur where a fully atomistic treatment is necessary. This is proven by Feng and Nix[125], who found an overestimation of single crystal MgO modulus under nanoindentation test due to the modulus is not properly calibrated.

Recently, a new approach of obtaining Young's modulus of single crystal of thin films using a new method which is AFM nanoindentation. The AFM nanoindentation was introduced given the capability of the instrument to control a significantly smaller indentation load compared to

standard nanoindentation. This depth-sensing nanoindentation technique is now used not only for hardness but also for extracting compressive stress-strain curve for elastic modulus without the need for measuring residual contact[126–128].Gouldstone *et al.*[129,130] conducted the AFM nanoindentation on single crystal aluminium thin films of (110) and (113) orientation with thicknesses of up to 2000 nm and obtained a similar results of elastic modulus by their theoretical value, which is 75 GPa.

However, there are certain challenges with the interpretation of AFM nanoindentation data which are explained in detail by Zeng and Tan[119]. One instance is the distorted force-displacement curve and erroneous contact area, which might be the result of a blunt/damaged tip combined with intrinsic compliance of the AFM cantilever probe. Moreover, no matter how low of a force is applied to the indenter, there will always be a contribution from the substrate. This is because the indenter load is not only supported by direct compression in the vertical direction, but also by compressive stresses acting onwards the sides. This makes the contribution of the film somewhat more than expected from simple and straightforward compression in the vertical direction only.

Despite the popularity of nanoindentation, materials with complex crystal structure (i.e brittle materials) may experience deformation on both hard and soft slip systems when the flow is required to accommodate the multiaxial stress field created during nanoindentation. Therefore, to overcome this issue, simple uniaxial compression technique is introduced with a response of interest on the stress-strain curve in compression test.

Uchic and Dimiduk[131] developed a variant on nanoindentation technique, which is called micropillar compression. It was motivated by an engineering challenge to measure the single crystal mechanical properties from a fully processed, polycrystalline material. In this technique, a conventional nanoindenter sharp Berkovich tip is truncated, resulting in a flat-end

tip being used to compress the pillars. The use of a flat punch tip enables the diamond indenter to act as a compression platen, where the attachment of the micropillar to the bulk in essence functions as the other compression platen[132]. The resulting load and displacement are measured, thereby facilitating the determination of the engineering stress-strain curves. This technique uses a nanoindenter with a flat punch to compress a small cylindrical volume to obtain uniaxial stress-strain behaviour (Figure 1.11).

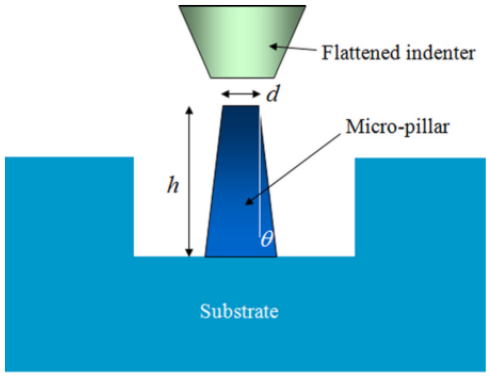


Figure 1.11: From Fei *et al.*[11]. Schematic of micropillar compression test

Microcompression has been widely used in electrical, optical and magnetic materials that are specifically linked with the microelectronic industry. One of the advantages of microcompression is that this technique can be used to study single crystal extensively, especially on the internal size effect even with the absence of grain boundaries which are strong internal barriers to dislocation glide. Compared to the nanoindentation technique, micropillar compression has the obvious advantage of creating a relatively uniform stress-strain field especially on thin film samples, which should ultimately lead to more accurate elastic constant measurements. However, since this technique uses a new method to measure stress-strain relationships, there is no standard procedure or body of reference yet. While most studies using compression testing focused on the onset plasticity, the elastic response of micropillars has received less attention[133].

Another advantage of using this technique compared to other established techniques include the ability to probe localised material properties that is measuring the single crystal in response of individual grains in a polycrystalline material[134–136]. It is also able to systematically evaluate intrinsic size effects related to the plastic deformation process. Localised material properties may also be measured by nanoindentation experiments; however, the complicated stress-strain states combined with possible strain gradient affects the interpretation of fundamental deformation process, which makes it difficult.

Introducing an indenter into a sample surface produces a complex stress field, which makes the determination of mechanical properties more challenging. A sharp indenter such as a Berkovich will drive plasticity almost immediately on contact. Whilst this is required in order to measure hardness, it does present limitations when material behaviour within the elastic limit is to be investigated. Additionally, as an indenter continues to penetrate a sample surface, an exponentially increasing volume material becomes involved in the deformation. As the indentation progresses, there will constantly be new material entering progressively advanced stages of deformation and this can create difficulties in understanding deformation mechanisms at work. Microcompression on the other hand, while performed on the sample, gives a constant stress at any given point along the specimen until, at least until plasticity is initiated locally. This technique is also useful when it comes to accessing plastic flow in brittle materials[130,137,138].

In addition, direct observation of an experiment in the SEM in combination with digital image correlation, offers the additional advantage of determining the deformation directly in the sample that was tested. For example, during microcompression test, the instantaneous pillar shape together with the load applied by the indenter gives much better access to the local and

instantaneous applied stress than the usually determined simple engineering stress, which assumes that the pillar deforms symmetrically.

While nanoindentation requires a minimum of five unique slip systems to be active for the material to accommodate strain, microcompression on the other hand induces a relatively uniaxial stress state in single crystal specimen. Moduli values for both techniques result in a load-displacement data. Unlike nanoindentation, microcompression data is independent on the platen size and not greatly influenced like others (i.e. indenter tip geometry, and dimensions between the indenter to the test samples)[117,132,139] which makes this method less complicated. Consequently, microcompression is the better method for analysing thin films.

Chapter 2

Experimental techniques

2.1 Epitaxial growth of Fe_xN

An epitaxial film is a film that is deposited on to crystalline substrate such that it has the same crystal orientation. There are two kinds of epitaxy which are known as homeoepitaxy and heteroepitaxy. Homoepitaxy is an epitaxy performed in which substrate or film of a crystalline film is grown on the same material, whereas heteroepitaxy is a crystalline film grown on a crystalline substrate or film of a different material.

Usually, epitaxial thin films are grown using techniques like molecular beam epitaxy (MBE), metallorganic vapour phase epitaxy (MOVPE), and hydride vapour phase epitaxy (HVPE). However, for this project, electron beam epitaxy (EBE) is the preferred growth technique due to the wide range of elements and compounds can be evaporated, since evaporation from multiple electron beam sources is possible with achievable high temperatures.

2.1.1 Electron beam physical vapor deposition (EBPVD)

Thin films samples of this work were grown heteroepitaxially on sapphire substrates by EBE at Imperial College by Dr. Robert Davies. EBPVD is a new method for the deposition of thin films of functional and electronic device materials. The technique uses an electron beam to heat solid pieces of individual elements or compounds in an ultra-high vacuum, evaporating them onto a substrate. There are several advantages over other thin film deposition techniques which are; (i) EBPVD has the capability to control individual parameters of electron beam with each evaporated material, (ii) a very wide range of elements and compounds can be evaporated

from multiple electron beam sources is possible and a higher temperature can be achieved than with conventional thermal techniques, (iii) it is possible to grown very pure films due to the direct transfer of heat from the electron beam to the material, with little heating of the surrounding areas, and (iv) it is able to have a precise control of film thicknesses and compositions through accurate control of the electron beam and shutters. Therefore, it allows the possibility of achieving very uniform material deposition by control and the relative target-substrate distances and angles [140].

EBE is a process in which a focused high energy electron beam is directed to melt the evaporant materials in a vacuum chamber. The substrates usually have already been pre heated for enhancing surface diffusion between the films and the substrates which results in the uniformity of the layer and creates smoother surface morphologies. The pre-heated condition of the substrate also promotes the removal of contamination from the surface. This surface material removal is the result of physical sputtering due to the momentum transfer between the energetic beam atoms and the substrate surface atoms [140–142] .

The evaporating material condenses on its surface resulting in the formation of depositions, which is known as thin films. Theoretically, because the electron beam only heats the source of material and not the entire crucible, a lower degree of contamination from the crucible will be present. By using a multiple crucible E-beam gun, several different materials can be deposited without breaking the vacuum.

Figure 2.1 shows a basic diagram of a simple of evaporation process between the materials in the crucible and the substrate. The materials (thin films) are placed in the crucible on top of the heated filament. By applying a high voltage, electrons are drawn from the filament and are focused as a beam on the source material. Basically, there are four main components in the EBE system; the first component is the EB gun assembly, followed by the crucible where the

materials to be evaporated are placed, the substrate table (where the substrate is placed), and lastly the vacuum chamber. The electron beam is created by thermionic emission from W filament and then aimed into the crucible by a magnetic field. The evaporant material is stored in a liner which sits inside the crucible.

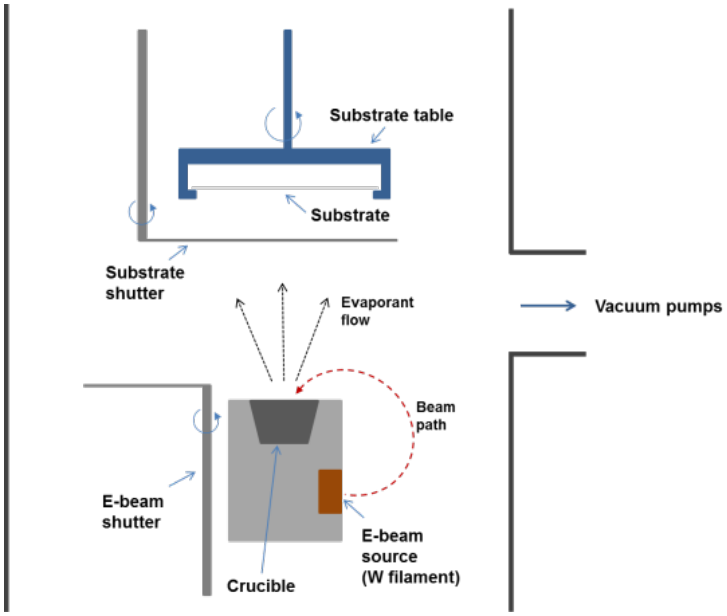


Figure 2.1: From Dr. Robert Davies. Schematic diagram of the EB-PVD process.

In this project, the crucible used for the growth of samples is alumina, while different parameters of nitrogen and iron are used to grow the thin film samples. The thin films that exhibit good properties in term of surfaces and microstructures are selected to proceed in the thin film compression testing.

2.2 Characterisation techniques

2.2.1 Atomic force microscopy

AFM or scanning probe microscopy (SPM) is a non-destructive technique used to image and measure surface properties of specimens at the nanoscale. The measurement relies on scanning a tiny and sharp tip (probe) that is attached to a cantilever beam that is brought across to be in

contact with the surface. The force and the distance between the tip and the sample surface are monitored and maintained by a force transducer. An optical sensor is commonly used as a force transducer where laser shines onto the tip and the reflection of the laser is monitored by a photodetector (Figure 2.2).

AFM probes the surface of the sample with a sharp tip which is located at the free end of the surface cantilever. The forces between the tip and the sample surface will cause the cantilever to bend. This cantilever deflection is detected optically by focusing a laser beam onto the back of a reflective cantilever. As the tip scans the surface of the sample, moving up and down with the contour of the surface, the laser beam is deflected off the attached cantilever into a dual element photodiode. This photodetector measures the difference in light intensities between the upper and lower photodiodes and then converts this signal into a voltage.

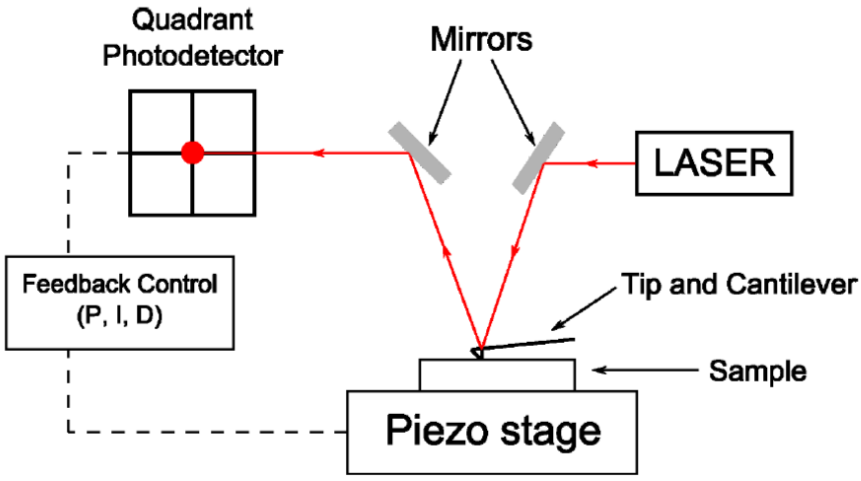


Figure 2.2: From Innova AFM Manual [12]. Schematic diagram of an AFM apparatus.

The AFM can be operated in three modes which are contact, non contact and tapping mode which is also called oscillation mode. Contact mode is done by the probe remain to be in contact with the sample all the time. Two techniques are used in this mode which are constant force and variable force. In constant force mode, the z-height is altered when the cantilever is

deflected. The changes of z is monitored and the topographical image of the sample surface is created. This method is often used in imaging; however, there is one main obstacle that arises from this method, which is the damage caused in the resolution of the images due to the adhesive or frictional forces between the probes and the samples. Deformation sometimes also appears on the sample due to this, hence giving an underestimation of the height of surface features [143].

As for the non-contact mode, the cantilever is oscillated near the surface of the sample (without making contact with the surface) in a smaller amplitude. As the probe reaches the sample surface, long range interactions (i.e van der Waals and electrostatic forces) occurs between the probes and the sample. The frequency of the cantilever's oscillations is detected. Phase changes between the driving and the oscillating frequencies permits the z=positioning of the cantilever to be modified in order to allow the cantilever to remain out of contact with the surface by the feedback loop. Due to the nature of this mode which does not allow the probe to be in contact with the surface, the area of interaction between the tip and the surface is usually minimised thus allowing a greater surface resolution[144].

Tapping mode is commonly used for inorganic thin films, and this mode has the cantilever oscillating up and down slightly below its natural resonant frequency during the scan. In this project, tapping mode is used to understand the surface features of the samples. It works by oscillating the cantilever assembly at or near the cantilever resonant frequency using piezoelectric crystal. The piezo motion causes the cantilever to oscillate with a large amplitude when the tip is not in contact with the surface. This amplitude is used as the feedback parameter and kept at a constant value. The lateral forces are considerably reduced compared to contact mode[144].The oscillating tip is then moved towards the surface until it begins touching gently or tapping the surface. As the oscillating cantilever begins to intermittently contact the surface the oscillation of the cantilever is reduced due to energy loss caused by the tip contacting the

surface. The reduction is oscillation amplitude is used to identify and measure the sample features[145146].

It is possible to control image size, number of lines in the image, scan speed, rotation angle and PID control is possible to be controlled in order to acquire good quality AFM images. The set point voltage represents the force between the tip and the sample surface, and this interaction force is used as the reference for the feedback loop to adjust the height of the stage. For tapping mode, a lower set point voltage means a greater interaction force where the tip is closer to the surface. However, the tip will be damaged if the tip is set too close to the surface.

Height, amplitude and phase can be obtained during an AFM scan. Surface morphology and roughness are usually obtained from the height information. The amplitude signal can be used to identify features and shapes and provides useful feedback while optimising image acquisition, while the phase signal gives information about the mechanical homogeneity of the sample and it can be influenced by the hardness and the adhesion of the surface. Data processing is normally required before presenting AFM results, typically image "levelling" and "flattening".

2.2.2 X-ray diffraction (XRD)

X-ray diffraction (XRD) is an analytical technique revealing X-ray scattering from crystalline materials. Each material produces a unique pattern of X-ray intensity versus scattering angle that is characteristic of its crystalline atomic structure. This standard technique is used for determining the crystallographic for thin films, powders and bulk samples in which parallel or slight divergent beam of monochromatic X-ray is directed at a specimen with known angles of incidence and the directions of the elastically scattered beams are then recorded for a range of scattering angles.

XRD involves probing a crystal with X-ray radiation having wavelength (λ) close to the crystal

lattice spacing as shown in Figure 2.3. When the material is radiated with a parallel monochromatic X-ray beam, the atomic lattice of the material diffracts the X-ray beam to specific angles. The diffraction pattern, including the position (angles) and intensities of the diffracted beams provides information about the sample such as the orientation of the grain and the phase of the crystal structure of an unknown material. All of these are based on Bragg's Law (Equation 2.2a), which states a specific condition of scattering that the angle of the incident beam is equal to that of the reflected.

Constructive interference occurs between the scattered x-rays when the path difference ($n\boldsymbol{\lambda}$) between the reflected beams is equivalent to 2d sin $\boldsymbol{\theta}$ (Figure 2.3) This will then results in a reflection to a particular set of crystal planes into diffraction spots (by measuring the angle of $2\boldsymbol{\theta}$ when the sample and/or the detector are moved), where n is an integer, $\boldsymbol{\lambda}$ is the wavelength of the incident X-ray beam, d is the distance between atomic layers in the crystal and $\boldsymbol{\theta}$ is the angle of the incident beam.

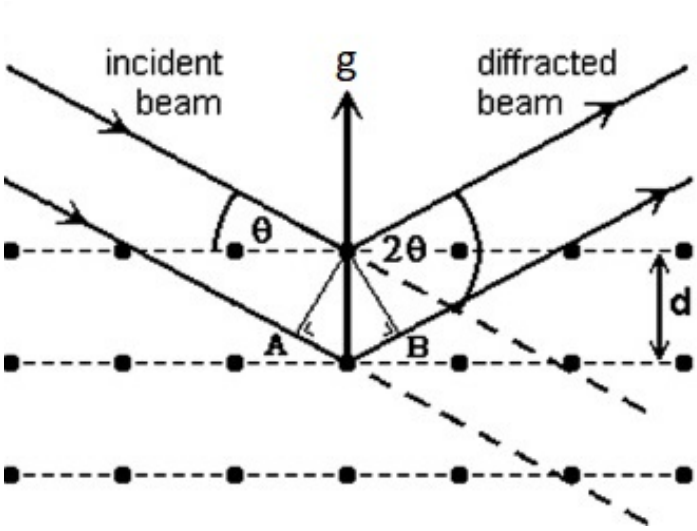


Figure 2.3: From M. Moram and V.Vickers [13] Schematic of x-ray diffraction where the condition required for Bragg diffraction to occur.

In the XRD, the instrument usually consists of five major components which are the xray source, incident optical system, goniometer, receiver optical system and detection system. The goniometer is the component, which is rotated or tilted in different axes, which allows different angles of the samples to be scanned. This condition also fulfilled the Bragg conditions (Figure 2.4). The basic instrument is called four circle diffractometer and that has been widely used. The diffractometer is usually composed of axes $\boldsymbol{\omega}$ axis (the sample rotation axis), axis is the in plane rotation axis.

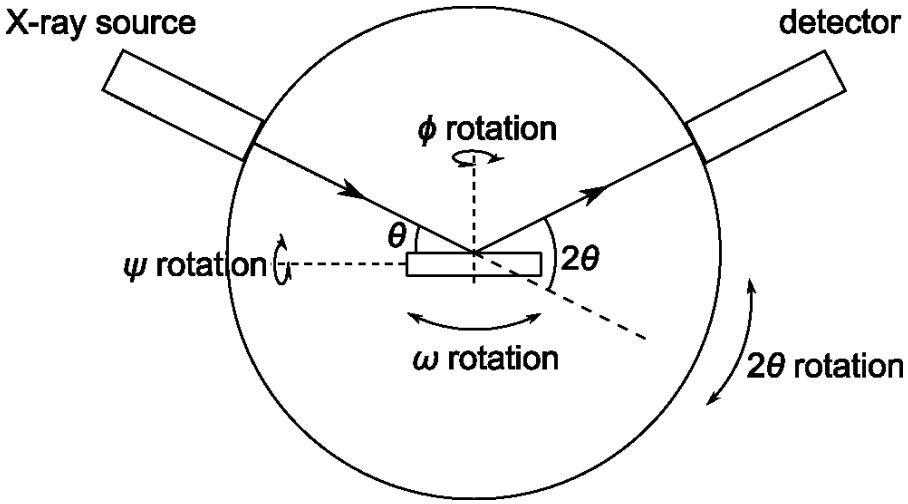


Figure 2.4: From T. Tsui [14]. Rotational axes of an X-ray diffractometer.

The reciprocal lattice and length can be altered by changing the 2$\boldsymbol{\theta}$ angle while $\boldsymbol{\omega}$ is the angle where the incident beam meets the sample surface. Since measurements are performed mainly by scanning roughly on the individual diffractions event and 2$\boldsymbol{\theta}$ axis, these two axes is known as the main axes. All XRD diffractograms presented in this thesis were obtained by using PANalytical MRD with a Cu Kα source with a step of 0.1° and counting time of 10 s per step.

2.2.3 X-ray photoelectron spectroscopy (XPS)

XPS is used for investigating the surface chemistry of electrically conducting and non-conducting samples. The use of ionising radiation of higher energy allows the probing of the core molecular electronic levels, which usually do no coalesce with neighbouring orbitals and therefore are non-binding orbitals in nature. Among several factors, the energy of the ejected photoelectron depends on which atoms are in the vicinity of the ejecting atom which is the energy of an x-ray photoelectron that is correlated with the electrostatic field created by the surrounding atomic species. This allows for chemical determination of the molecular structure of the sample and is one of the main advantages of the XPS technique.

The photoelectron emissions also leave behind ionised atoms. The ionised atoms are in a relaxation state which occurs when an electron drops from a higher energy to a lower energy. The atoms electron binding energy in the outermost shell are sensitive to the strength and the nature of the chemical bonds (chemical state). This condition will give rise to the Auger electron emission, because of which Auger peaks will also appear in the XPS spectra and may sometime overlap with the XPS peaks [147].

Where E_k and E_b are respectively the kinetic and binding energy of the emitted photoelectron and hv is the electron photon energy, the kinetic energy of the photoelectrons of the same and/or different atoms and orbitals have different binding states and binding energies. E_b is the binding energy of the electron and each one of it is unique to one another. Energy from the incident X-ray (hv) is absorbed by the core-level electron and this will affect the binding energy, leading the photoelectron to leave the atom with a particular kinetic energy (E_k) (Equation 13). W is the spectrometer work function. The work function is the difference between the energy of the Fermi level E_f and the energy vacuum level E_v, which is the zero point of the electron energy scale (Equation 14). This is determined by calibration of the spectrometer used. The electron binding energy in the atom increases as the energy of the emitted photoelectron decreases. A

schematic energy diagram for the emission [147–149]

$$Ek = hv - Eb - W \tag{13}$$

$$W = Ef - Ev \tag{14}$$

In basic understanding, the electrons are arranged in orbital levels (k, l, m and n) around the nucleus and they are bound by the electrostatic attraction. Each orbital level has an individual energy level that differ in value from the same orbital level in atoms of different elements, due to the different electrostatic attraction to the nuclei with a different number of protons. The amount of energy required to remove one electron from the atom which is the energy of its orbital level is directly affected by the binding energy of the electron. Therefore, XPS is used to interact with core electrons present around the nucleus of the different atoms present in the sample, and these electrons, if they escape the sample, are emitted at a kinetic energy and analysed by the electron spectrometer (Figure 2.5).

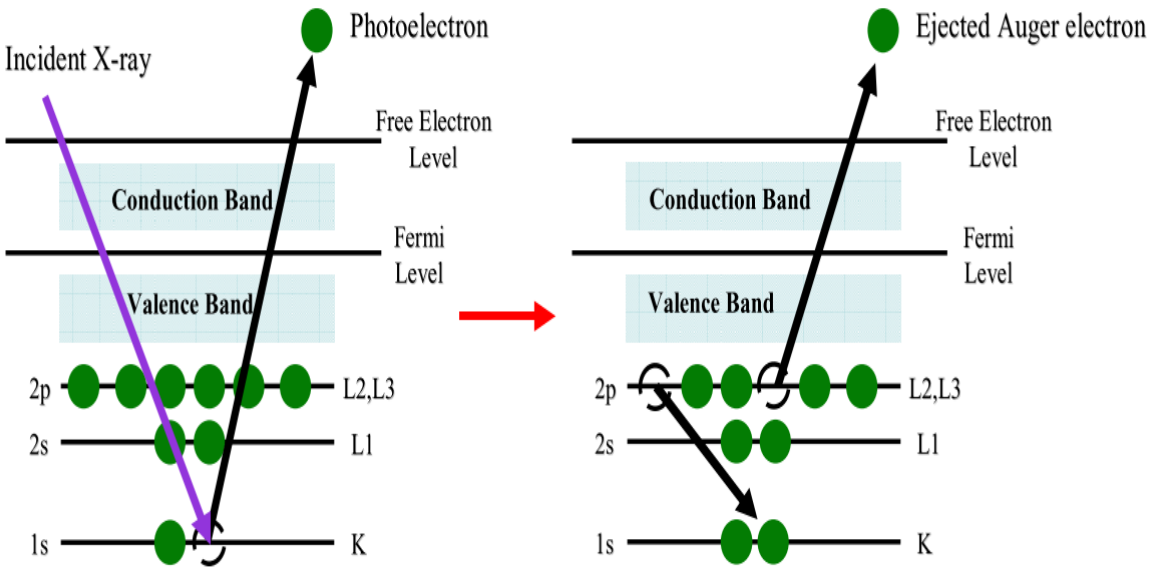


Figure 2.5: From L. Calvo-barrio and G. Vargas [15]. (a) X-ray induced photoelectron emission and (b) Auger effect in the photoelectron emission.

Multiple peaks of photoelectron signal are generated when the atom is in a different

coordination or binding state experienced emission from the photoelectron. For example, Figure 2.6 shows Fe $2p_{3/2}$ and Fe $2p_{½}$ of FeN sample which was fabricated under the N_2 partial pressure of 0.2 mTorr. The Fe 2p spectrum resembles the main peak and the neighbouring shoulder peak. It can be seen that the Fe $2p_{3/2}$ exhibits a stronger peak compared to Fe $2p_{1/2}$. For Fe $2p_{3/2}$ spectrum have three values of binding energy which are 707.2 for the highest peak, 708.5 eV for the second one and the last one is 710.5 eV respectively. Meanwhile for the Fe$2p_{1/2}$ the peaks are 719.8 eV, 721.0 eV and 723.5 eV.

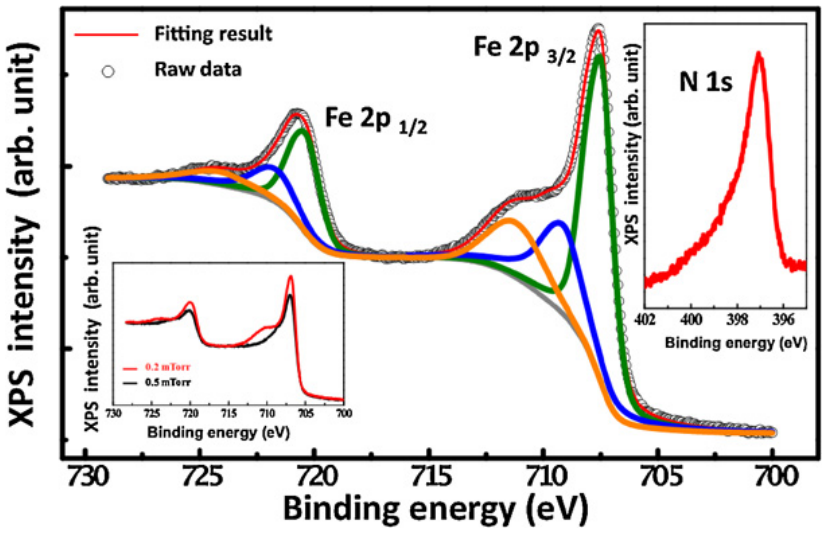


Figure 2.6: From Lin *et al.* [16] XPS spectrum Fe $2p_{3/2}$ and $2p_{1/2}$ of FeN sample fabricated under a N_2 partial pressure of 0.2 mTorr.

In the XPS spectra, the Auger peaks may overlap with the XPS peaks and cause a problem with the quantitative analysis. The generation of photoelectrons in XPS leaves behind ionised atoms. The Auger electron emission occurs when an ionised atom relaxes, which happens when an electron drops from a higher energy level to a lower energy level.

In this thesis, XPS spectra were collected from a Thermo Fisher K-Alpha spectrophotometer utilising a monochromatic Al-Kα X-ray source (Energy = 1486.71 eV). Samples were positioned at the electron take-off angle normal to the surface with respect to the analyser.

Survey spectra in the range 0–1300 eV were recorded for each sample (pass energy = 200 eV) followed by high-resolution measurements (pass energy = 50 eV) of core levels for C 1s, N 1s and Fe 2p for Fe_xN thin films and C 1s, N 1s, Fe 2p and W 4f for $Fe_xW_{y-1}N$ thin films. XPS spectra were calibrated to the adventitious C 1s signal (284.6 eV). The spectra analysis was carried out by Thermo Avantage Software (v. 5.948) using a Shirley background for the fitting of the spectra.

The depth profiling experiment was conducted using an EX06 Argon Ion Source to sputter samples for thin film samples. After various time intervals during the etching layer process, 'snapshots' of the relevant core level spectra were obtained (acquired by holding the analyser voltage constant and using the detector width to sample a binding energy window). The sputtering involved ion energy of 8000 eV with raster size of 1.6 mm. The thin films were etched up to 100 nm level and were run for 600 second for Fe_xN thin films samples and 60 second, 120 second and 180 second for thin films of $Fe_xW_{y-1}N$ thin films of etching cycle because the thickness of this ternary nitride is smaller compared to Fe_xN films. Survey scans and narrow scans (Fe 2p and N 1s) was conducted at 200 eV. Dr Anna Regoutz at Imperial College London, United Kingdom assisted with this experiment by monitoring the used of the instruments with the parameters provided while we handled the machines and analyses the data.

2.2.4 Secondary electron microscopy (SEM)

The SEM generates a beam of incident electrons in an electron column above the sample chamber. The electrons are produced by a thermal emission source, such as a heated tungsten filament or by a field emission cathode such as a LaB_6 crystal. The energy of the incident electrons can be as low as 100 eV or as high as 30 keV, but typically higher energies are preferred because this produces a shorter electron wavelength and therefore better diffraction-limited resolution. Although the image formation is different from transmission electron

microscopy (TEM), the image is easy to interpret, and these machines share a number of similar components such as the condenser lens and objective lens. However, TEM has a completely different image mode which will be further explained in the next subsection.

In SEM, the electron gun releases electrons, which are then focused into a small beam by a series of electromagnetic lenses in the column. The electrons will be focused into the electromagnetic lenses and the scanning coils will deflect the beam in the X and Y axes so that it scans in a raster pattern over the surface of the sample. The detectors in the SEM will detect the signal of electrons such as the secondary electrons (SE) and back scattered electrons (BSE) and will develop and image by synchronising the amplified current signal and the monitor. (Figure 2.7)

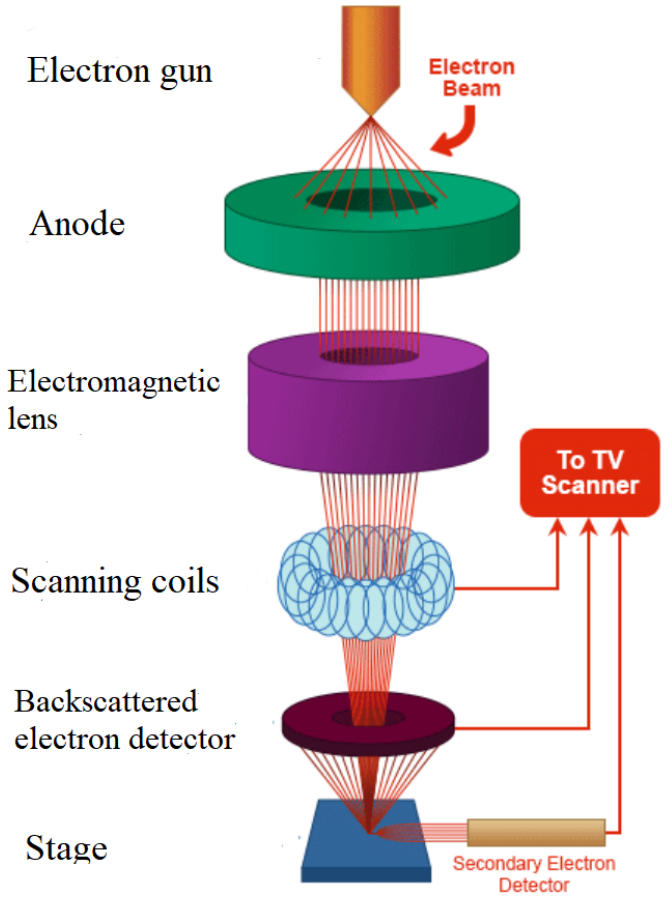


Figure 2.7: A basic SEM schematic diagram[17].

2.2.4.1 Imaging

In SEM, a beam of high energy electrons is focused to a point and scanned in a raster pattern across the surface of the sample. As these electrons hit the sample, they will enter the surface atom layers and they will interact as elastically or in an elastically scattered manner. Elastically scattered electrons lose little or no energy during the collisions. Meanwhile inelastic scattered electrons lose significant energy during the collisions and therefore have low energy when the escape the sample surface. These electrons are known as secondary electrons (SE). Meanwhile for the elastically scattered electrons that lose little or no energy during collisions, the electrons escape with high energy and there is a higher probability that their escape trajectories will be at a high angle (which means it will be back in the direction of the electron gun that produced them). These electrons are known as back scattered electrons (BSE). The difference in the energies of SE and BSE allows them to be separated by different detectors to produce different signals and images of the sample.

It is also helpful to understand the difference between images as it is useful to consider the interaction volume from which the signal is produced. Due to their lower energies, SE's usually are attracted towards a SE detector using a positive bias on the front of the detector and the electrons travel in a curved path to the detector. This makes it possible to see down holes and around corners, as the electrons are attracted from this region. Furthermore, by attracting the electrons the SE image appears to have been illuminated from the brightness of the SE image depending on the angle between the sample and the detector. The images therefore are highly topographical. SE can easily be deflected by regions where electric charge builds. In non-conducting samples, this may produce severe image distortion or in less severe cases charging will appear as bright regions.

In contrast, BSE are higher energy electrons that are more likely to be scattered at high angles. Therefore, the detector of BSE is placed directly above the sample as it travels in straight lines.

The resulting images contain less topographical information. However, the higher average atomic number of the area being analysed, the greater probability that the BSE will be generated. As a result, BSE images display atomic number contrast with brighter regions that arise from the areas of higher average atomic number. BSE are less affected by electric charge and there are more suitable for imaging samples with oxide layers or other thin insulating layers on their surfaces, which would interfere with SE images. However, the BSE detection efficiency is quite poor, therefore the signal to noise ratio in BSE images is usually worse compared in SE images.

The SEM used is the QUANTA SEM 650F to record and capture the in situ compression of the samples with SE image mode at 5 kV.

2.2.5 Transmission electron microscopy (TEM)

The electron beam in TEM, which is produced by a LaB_6 filament or field emission source, interacts elastically or inelastically with an electron-transparent specimen, and thus gives structural, compositional and electronic information of the specimen material. These high energy electrons (100 to 400 keV) constituting the beam are condensed into a coherent parallel illuminating beam by a set of condenser lenses and apertures The following section describes the method for sample preparation used in this study and descriptions of TEM-based methods used to characterise these Fe-N based thin film layers.

2.2.5.1 Sample preparation

One of the requirements of TEM samples is that it must be electron-transparent in order for the electron beam to be transmitted through the sample. Therefore, the specimen thickeness should be less than 100 nm for conventional TEM and less than 50 nm for high resolution transmission electron microscopy (HRTEM). A step by step approached is carried out to achieve this. The sample is prepared with lift out technique. Initially, a rectangle area of 10 µm x 2 µm x 10 µm was used for platinum deposition using the electron beam. Gallium is not used immediately as

it will induce more damage to the sample surface. After the platinum has been deposited on the surface with 0.69 nA, the stage is tilted to 52° in order to achieve a coincident point which is when both SEM and FIB images will image the same part of the sample. The Gallium is deposited on top of the sample with a lower current of 0.46 nA. After these steps have been taken, two regular trenches were milled on both sides of the platinum strap with a higher milling current, which is around 21 nA for approximately 30 minutes and the lamella is cut at 7°. The lift out is carried out with the OmniProbe needle with the stage is at 0°. Platinum is stuck between the needle tip and the lamella for the lift out to occur. Once it is done, the lamella is then welded to the grid by the platinum before proceeding to the specimen thinning. The final stage is specimen thinning where the stage is set at 52° and the specimen is milled on both sides until it is thin enough for TEM imaging to take place.

2.2.5.2 TEM imaging

A crystal can be described as lattice points of equal symmetry. It occurs when the constructive interference takes place, where it will form a reciprocal lattice. Reciprocal lattice points correspond to a plane in a real space (Figure 2.9). The reciprocal lattice points of a TEM specimen appeared as elongated rods (also known as relrods) due to the limited thickness of the sample. A diffraction spot is formed when the edge of an Ewald sphere cuts through any part of the relrod. If the relrod cuts through the reciprocal lattice point, the Bragg condition is satisfied and the Bragg condition will only be perfectly fulfilled if the relrods cut at the centre of the Ewald sphere and hence the planes will be strongly be diffracted (Figure 2.8) [18].

Electron diffraction in TEM is different from XRD as the process to obtain diffraction spots in TEM does not need a sample rotation (Figure 2.9). This is because the wavelength of high energy electron is much shorter than X-rays giving rise to a large Ewald sphere and making more room for the intersection for the edge of the Ewald sphere to occur, thus giving more lattice points. The diffraction spot intensities are highly affected by the specimen thickness and

also the electron wavelength because the length of the relrods depend on the thickness of the sample. In TEM, the electron has a higher inelastic scattering cross section compared to Xrays, which permits the electron beam to be re diffracted thus resulting in a double diffraction that deviates from the theoretical predictions for the crystal.

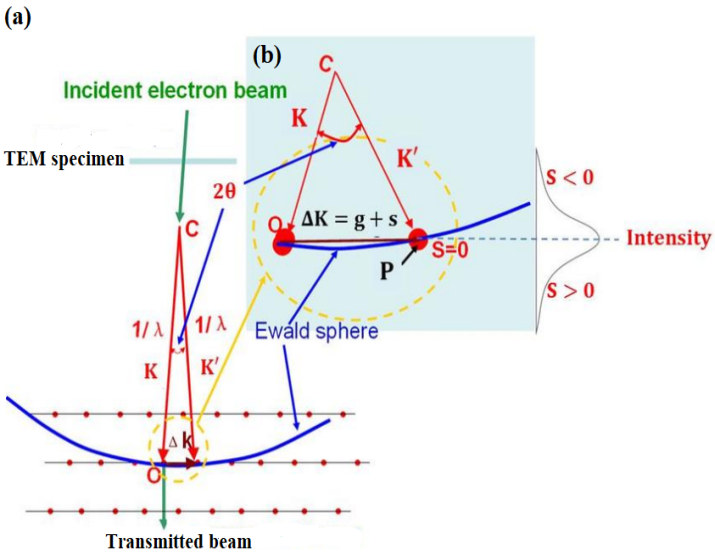


Figure 2.8: (a) Relrod in reciprocal space created from diffraction of a crystalline specimen and (b) The relrod when the beam is away from the exact Bragg condition. The Ewald sphere intercepts the relrod at a negative value of s which defines the vector **K = g + s** [18].

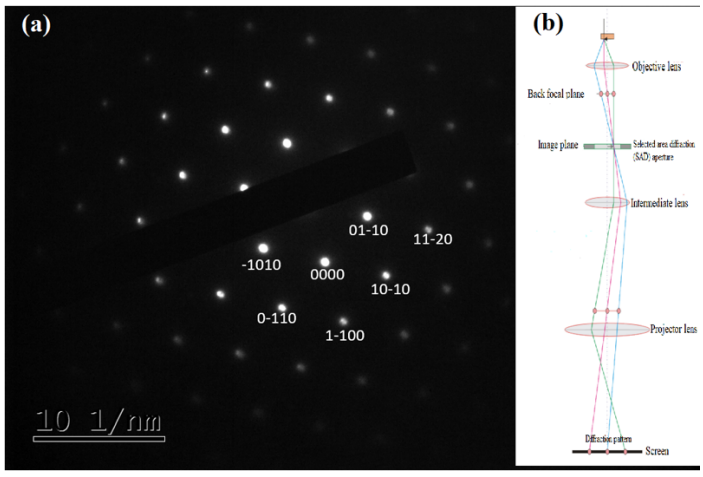


Figure 2.9: (a) An image of DP acquired along [0001] for a cross section sample of Fe_XN, showing the direct (0000) and (b) is a schematic diagram of the process to achieve a diffraction pattern.

2.2.5.3 Mass thickness contrast, diffraction contrast and phase contrast

Contrast in bright field and dark field TEM images is usually diffraction contrast or the variations in intensity of diffraction across the sample. There are two types of contrast that arise in TEM images due to the relative intensity difference between two adjacent areas which are amplitude contrast and phase contrast. The amplitude contrast consists of mass-thickness contrast and diffraction contrast.

When imaging in TEM, a few images that has fringes will appear. This is due to the phase contrasts, which are produced by the interference of more than one diffracted electron beam. The excitation error s and the thickness t of the specimen (Equation 15) will affect the intensities of the electron beams by changing them. Typically, three forms of phase contrast typically can be seen in TEM images: Moire patterns, including rotational and translational patterns which happen then the incident electron beam passes through two superimposed regions of different crystal structure and/or orientation, the lattice fringe, which occur when multiple diffracted beams interact to produce an image (also known as high resolution TEM), and lastly the Fresnel contrast occurs when the imaging of multilayers in which the electrons travel parallel to the interfaces between the two later materials. This happened because the electrons experiencing an abrupt change in the scattering potential parallel to the electron beam path [150].

$$I = A^2 + B^2 - 2AB \sin(2\pi g'x - \pi st) \quad (15)$$

Amplitude contrast results from the variation in mass or thickness. Mass thickness contrast is sensitive to the atomic number and thickness of the specimen. A higher number of incoherent elastic scattering occurrs when a constant mean free path electron passes through the specimen at a region with heavier mass or greater thickness, causing the electrons to be scattered off the optic axis. Therefore, in a BF TEM image, the regions associated with higher atomic mass or greater thickness appear to be darker (Figure 2.10).

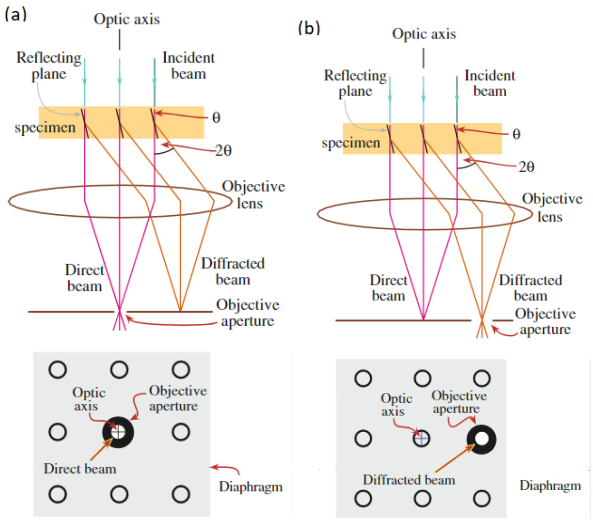


Figure 2.10: From Williams and Carter[18].Ray diagram showing how the objective lens and objective aperture is used in combination to produce (a) Bright field image that is formed from the direct electron beam and (b) a displaced aperture dark field image formed with a specific off axis scattered beam.

Diffraction contrast occurrs when the Bragg condition is satisfied which arose from the coherent elastic scattering. The two beam condition should be achieved in order to get the Bragg condition. This is caused by tilting the specimen where only the direct beam and one strong diffracted beam are seen. The diffraction contrast is sensitive to the crystal orientation and defects as both of them would change the diffraction condition, thus the intensity of the coherent scattered electrons beam contributed to the image.

2.2.5.4 High resolution imaging

The high resolution transmission electron microscopy (HRTEM) uses both transmitted and scattered beams to create an interference image. It is a phase contrast imaging technique where it uses multiple beams by the objective aperture to utilise interference between the selected beams to obtain images.

The contrast of HRTEM image arises due to interference in the image plane. Each imaging

electron interacts independently with the sample. As the electron penetrates the sample, the positive atomic potentials of the atom cores are attracted and channels along the atom columns of the crystallographic lattice. A large objective aperture has to be selected that allows many beams including the direct beam to pass. The image is formed by the interference of the diffracted beams with the direct beam (phase contrast). If the point resolution of the microscope is sufficiently high and a suitable crystalline sample oriented along a zone axis, then a HRTEM images is obtained. This interaction also gives rise to the Bragg's law. For example, when the intensity (I) arising from interference between two beams (transmitted and a single diffracted beam) is considered, it is governed by Equation 16 (where t is the specimen thickness and A and B are constants) which shows that the intensity due to interference is a sinusoidal periodic function on top of a smooth intensity of $A^2 + B^2$ with a period equal to $\frac{1}{(g+s)}$

$$I = A^2 + B^2 - 2ABsin(2\pi(g+s)x-\pi st) \quad (16)$$

When s = 0 (Bragg diffraction condition), the periodicity of the lattice fringe intensity is equal to $\frac{1}{g}$, which can be related to spacing between lattice planes (d_{hkl}) perpendicular to g as $\frac{1}{g(hkl)}$ is equal to d_{hkl} which is known as the lattice image.

On this project, the sample was acquired by high resolution images of the cross-sectional samples (along <11-20>) on the JEOL 2000FX. This technique was only employed for preliminary work to determine the thickness and also to understand the crystal structures of the thin film that has been previously grown via E-Beam method

2.3 Mechanical property measurement

2.3.1 Principle of focused ion beam (FIB)

The basic instrument of focused ion beam (FIB) consists of a vacuum system and chamber, a liquid metal ion source (LIMS), an ion column, a sample stage, detectors and gas delivery system. The FIB setup uses a focused beam of ion and can incorporated both electron and ion beam columns in its system.

The FIB system consists of a sample chamber which is always maintained under high vacuum, an ion column which consist of ion source, accelerating, focusing and scanning optics, a series of detectors which usually is secondary electron and secondary ion detection, and a stage which can be rotated. There is also an electron column which is usually mounted at the top of the chamber with the ion column. The position of electron and ion column are determined by the geometry of the two columns. This is because these two columns will have one point in the chamber where they focus at the same coincident point, which enables the two columns to be used simultaneously such as while the sputtering process is on going in the ion column, the electron column will be monitoring the sample to make sure everything is in order. One of other reason is that having an additional column will also prevent the sample from being damaged by the beam because the electron column provide a non-destructive imaging of samples[151].

The liquid metal ion source is one of the important parts in the focused ion beam system. It is an ion source which uses metal that is heated to the liquid state and used to form an electrospray to form ions[152]. According to Gholinia[151], Gallium ion source is the most commonly used source compared to other sources for a number of reasons which are:

i) Ga+ has lower melting point (Tmp = 29.8^{o}C) and therefore Ga will remain liquid even at quite low operating temperatures. This will minimise any reaction or

interdiffusion between Ga liquid and the tungsten needle substrate.

ii) Ga has a very low vapor pressure of melting point, which will conserve the supply metal and therefore yield a long source life (up to 1500 hour sources).

iii) The low vapor pressure of Ga means that it can be used in its pure form instead of in the form of an alloy source.

iv) It has ion emission characteristics that enable a high ion flux within a small solid angle with a small energy spread.

Figure 2.13 shows a basic schematic diagram of a Ga ion column. The ion source sits at the top of the column. The accelerating voltage is controlled by the extractor while the ion current flow that is allowed to be spread down the column is controlled by the beam aperture. The beam of this machine is achieved by the series of lenses. One of the uniqueness of FIB is its ability to prevent the sample from being exposed by the beam while the milling takes place. The Ga ions will be emitted from the end of the cone and accelerated into the column once the voltage of the extractor is increased

The extractor (shown in Figure 2.11) is positioned close to the tip to enables the ions from the tip to be pulled by the electric field that exists inside the extractor. A balanced of two forces occurrs when the surface tension of the liquid Ga repulses the process of the extractor to pull the ions from the tip thus governing the formation of a cone shape with convex sides and a rounded tip.

The whole system of FIB is kept under vacuum (lower than at most 1×10^{-7}) by the ion pumps and another column of vacuum isolation valve that govern the system from being vented when opening the specimen chamber to air.

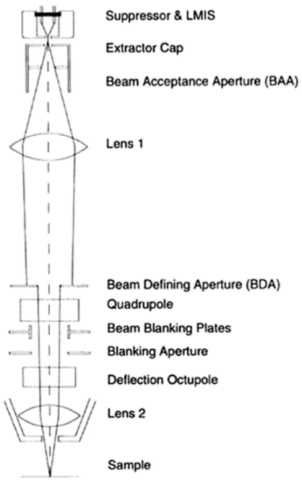


Figure 2.11: A basic schematic diagram of a Ga liquid metal ion source in FIB column [152].

2.3.1.1 Fabrication of micropillars with focused ion beam

Pre-fabrication of the sample is carried out by making sure that the sample is free from any contaminates and water to prevent them from getting vaporised in the vacuum. The bulk sample is placed onto the stub with conductive silver paint before placing it in FIB.

The FIB is used to machine a pattern in a cylindrical shape with a specified inner and outer radius (ri and r0 respectively) that is centred on a given area of interest. Micropillars were fabricated in several stages carried out at 30 kV. Once in the chamber, the sample stage was tilted to 52° (with respect to SEM column) to place normal to the FIB column in the Helios Nanolab. For each time, different ion beam and size are used in order to get flat and straight cylinder shape of micropillars. After the final milling process, the base and the top of the micropillar have approximately the same width, i.e. the pillar has a round, columnar shape. Usually, the approximate aspect ratio of the final pillars 1: 3 was chosen.

The first stage was under the high beam currents to increase the rate of sputtering and reduce the fabrication times. This process is called the rough machining step. Subsequently, a lower current was executed on these pillars to minimise ion damage and in order to obtain the milling resolution that allows the edges to be shaped with sufficient quality. Therefore, for the second

milling stage, a current of 7.8 nA is used and for the last milling the probe current is reduced to 0.92 nA, the last milling is crucial in order to clean all the sidewalls and reduce tapering on the micropillars. Table 1 shows a summary of the milling process of making micropillars for MgO and sapphire.

Alternatively, some of the milling procedures in the FIB instrument can be automated with programs written in a scripting language since some of the samples are very hard to be fabricated by the FIB using the manual milling process (i.e. the material is conductive hence making it unstable in the FIB system or/and the material has a higher strength and it is difficult to mill them manually). For this project the program used is NanoBuilder software script and it was written by Dr Giorgio Sernicola.

The NanoBuilder program was used on the FIB system where the system is aligned along the axis of the micropillar and milled a fiducial mark (which in this project is a cross pattern) into the top of the sample's surface (Figure 2.12). Before proceeding to the milling process, the fiducial mark is protected by the platinum deposition layer in order to protect the mark from beam damage during the pillar milling process. The parameters of the pillar fabrications are as mentioned above. The pillars were first milled at a higher current of 21 nA at the beginning of the fabrication process, and as the pillar becoming a circular pillar, the milling current is decreased up to 0.92 nA.

Table 2.1: Summary of milling process of micropillars on MgO and sapphire.

Samples	Milling stage	Ion beam current	Time
(material)	(number)	(nA)	(sec)
MgO	First	21.0	240
	Second	7.8	360
	Third	0.92	600
Sapphire	First	21.0	300
	Second	7.8	900
	Third	0.92	1200

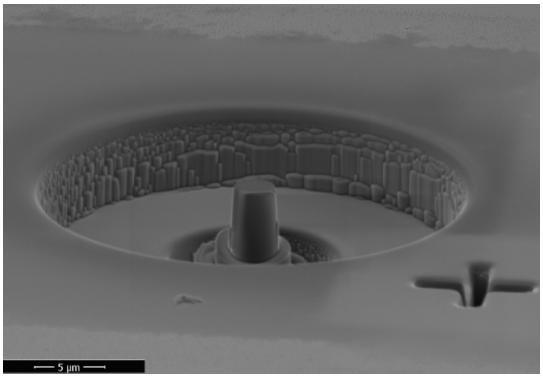


Figure 2.12: Image of a sapphire 0001 pillar with a cross pattern fiducial mark. Platinum deposition is placed on the fiducial mark to protect it from the beam damage during milling.

During the fabrication of pillars on MgO, sapphire and thin films, there were a few techniques and precautions that are crucial to produce smooth and better cylindrical shape pillars. These are:

i) Aspect ratio plays an important role in the pillar fabrication. A higher aspect ratio tend to buckle during compression, whereas a smaller aspect ratio will introduce

non uniform stress along the length. Therefore, selecting a suitable aspect ratio with the height and diameter of the pillar is very important[153]. For our project 1 : 3 ratio is expected on the micropillars.

ii) Closer observation on the pillars revealed surface asperities and imperfections over the range of pillars after fabrication. This is typically seen on the top of the pillars. Therefore, it is important to take great care during the fabrication process to minimise these surface imperfections in order to produce a regular pillar that deforms uniformly as expected.

iii) One of the major issues when performing microcompression is the misalignment between the indenter and the top surface of the pillar. Therefore, the surface of the samples should always be as flat as possible and clean (i.e. no inclusions and impurities) in order to get even pillars.

iv) Between each step of pillar fabrication, an image correlation alignment procedure was used to correct the beam shift due to the change of current or stage movement[154]. This is done by focusing on "marker" which is the fiducial mark. Therefore, it is suggested to protect the fiducial mark with platinum deposition to maintain the fiducial mark size from the beam damage during the milling process.

v) During FIB fabrication for pillars, these processes should be performed by reducing the ion beam current incrementally to minimise the potential FIB damage in the micropillars[155]. This will also help to fabricate a smooth and clean pillar.

vi) Due to the nature of the samples, the design parameters for each material varies. For example, the fabrication of one pillar on sapphire takes a longer time compared to MgO and silicon. Therefore, trial and error shall be conducted on these materials to find the suitable gap distance, milling current, cross section shape and size of the pillars during each of the milling session (Refer to Table 2.1)[156].

2.3.2 Microcompression

The Young's modulus is measured by using the micropillar compression technique. This technique is adapted from a standard nanoindentation system equipped with a flat diamond punch. A typical loading and unloading curve is obtained during this micropillar compression, where the displacement plotted represents the total compression relative to the initial position of the indenter at the sample surface. The curve shows both elastic region with respect to stiffness, which is obtained from the tangent of the unloading curve in the load-displacement curve obtained by the microcompression technique. The load displacement data obtained during the mcirocompression are then converted to the stress and strain with the assumption that if there is any plastic deformation, the plastic volume is conserved throughout mostly homogeneous deformation [157].

This method combines nanoindentation and focus ion beam (FIB) micro fabrication techniques to probe the possible stress-strain curve in order to study and understand the elastic modulus of these materials (MgO 100, MgO 110, Sapphire and Fe_xN). The microcompression experiments were performed on a Quanta SEM 650F with an Alemnis Nanoindenter. It uses displacement rate controlled mechanism as the system is moved by a piezoelectric transducer with a maximum displacement of 35 μm and load of up to 500 mN. Samples were mounted on top of the calibrated load cell with a tilt of 30º between the sample and the horizontal plane of the chamber (Figure 2.13a and 2.13b).

The flat diamond punch of 10 um in diameter is used to press the pillar top. This diameter of the flat punch was chosen to ensure that it is larger than the diameter of the pillar and smaller than the perimeter of the surrounding material from which the pillar was milled. The punch is placed parallel to the pillars prior to the microcompression experiments. This is to ensure that the perimeter of the contact between the punch and the pillar is symmetric, indicating a good alignment of the surface normal and loading axis [158].

The displacement rates of 5 nm s^{-1} was used to compress the micropillar with the diamond flat punch tip. For each cycle, the micropillars were near uniaxially compressed by the flat punch. In standard mechanical experiment, the compliance of the machine is eliminated either by using extensometers or strain gauges. Therefore, during compression of the pillar, the punch was withdrawn and held with $1/10^{th}$ of the maximum displacement to measure thermal drift and also to correct the load displacement results. The indenter was also left to stabilise in the vacuum chamber around 1 hour ,to stabilize instrument especially effect from thermal drifts[154,159].

The SEM was used to generate an in situ video of the microcompression process with a reduced window and a frame capture time of 500 ms. .Each of the segment of loading displacement step starts at 0 µm and is increased by 0.2 µm for each of the steps, while as for the unloading it is increased by 0.1 µm for each of the steps until it reaches the fifth cycles which will be back to 0 µm (Figure 2.13c).

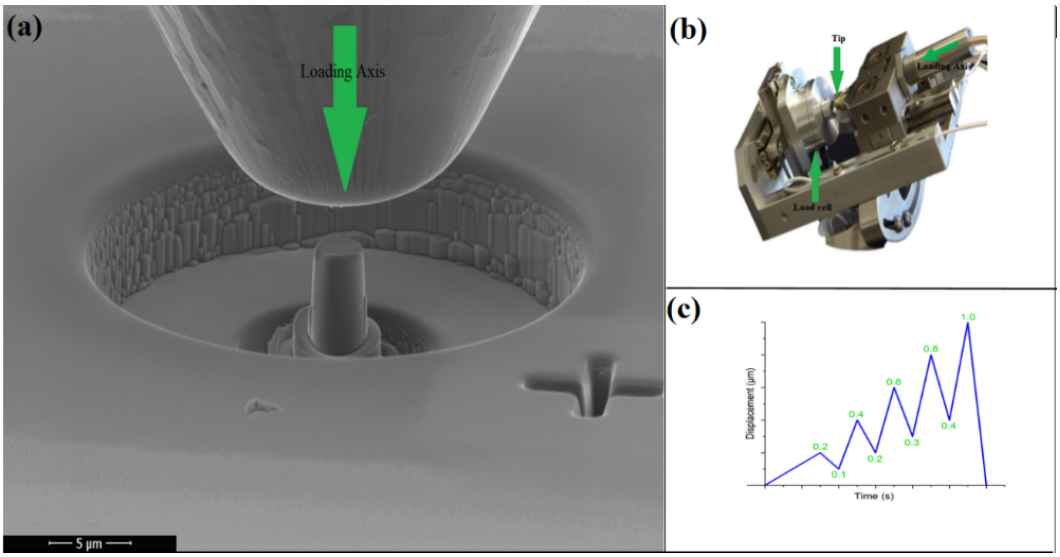


Figure 2.13: (a) SEM micrograph showing a flat punch tip of 10 µm in diameter parallel to micropillar with (b) inserts of Alemnis nanoindentation platform for in-situ compression test and (c) the load-test conditions of loading and unloading of the tip displacement

As for data analysis, it should be noted that the pillar displacement cannot be measured directly in the microcompression experiment. Instead, the displacement of the top surface of the indenter with respect to the rigid base underneath the substrate should be taken into account when measuring the pillars displacement. In other words, the total displacement of the system, including indenter, pillar and substrate is the directly measurable quantity, which is given by

$$\Delta x_{total} = \Delta x_{ind} + \Delta x_{pillar} + \Delta x_{sub} \tag{17}$$

where Δx_{total} in the indentation depth and Δx is the deformation of each part in the microcompression test which is "ind", "pillar" and "sub" denoted as indenter, pillar and substrate respectively shown in Equation (17). The deformations of indenter and substrate from the displacement should be eliminated to accurately quantify the pillar deformation which is Δx_{pillar}.

Sneddon correction consider the sinking effect of a cylindrical punch indenting into an elastic half space, where the half space material compliance[160] is denoted as $C_{Sneddon}$. E is the Young's modulus, v is the Poisson's ratio and A_p is the contact area between the punch and the half space material which is given in Equation (18) by assuming the punch to be the pillar, and the half space material to be either the indenter and/or substrate, Equation (18) can be applied to the microcompression test.

$$C_{Sneddon} = \frac{(1-v^2)\sqrt{\pi}}{2E\sqrt{A_p}} \tag{18}$$

While Equation (19) is the deformation of indenter and the substrate given in term of their compliance by assuming that the system acts as a series of springs consisting of indenter, pillar and substrate where f is the applied force on top of the indenter[11].

The deformation of indenter and substrate are given in terms of their compliance by considering

that the system acts as a series of springs consisting of the indenter, pillar and substrate. Thus, given the true pillar deformation by[161,162] where r_{top} and r_{base} are the radius of the top and base surfaces of the pillars in Equation (20)

$$\Delta x_{ind} = C_{ind} \cdot f,\ \Delta x_{indsub} = C_{sub} \cdot f \tag{19}$$

$$\Delta x_{pillar} = \frac{(1-v_{sub}^{2}).f}{2E_{sub} \cdot r_{base}} - \frac{(1-v_{ind}^{2}).f}{2E_{ind} \cdot r_{top}} \tag{20}$$

Finally, the load displacement curve is plotted and converted into stress strain curve (by taking the diameter and length of each pillar into account) in order to obtain the elastic modulus of all pillars from the stiffness of the stress and strain curve in the unloading cycle[163].

Based on the work of finite element model carried out by Zhang *et al.,*[139] a correction factor is used when pillar and substrate are from the same materials. This finite element model is based on aspect ratio, specific geometry, and sometimes material of the pillar. Factors such as the fillet radius (or the curvature at the bottom of the post connecting to the base) of the sample before and after the compression is taken into consideration when calculating the correction factor. Besides that, material properties of the pillars are also considered such as strain hardening and strain rate sensitivity. The work of this finite element analysis of microcmpression is supported by a study conducted by Lee *et al.*[164] on the Magnesium based bulk metallic glasses (Mg BMG) pillar where it stated that when the pillar and the substrate is of the same material, under such condition, based on the finite element analysis of micromcompression, the actual Young's modulus should be corrected by the factor of 1.25. This then changed the Young's modulus value Mg BMG pillar from 41.0 GPa to 51.3 GPa.

The method used in finite element analysis on elastic modulus is not suitable for this project. One of the reasons is the difficulty to determine the exact fillet radius as the bottom of the pillar is sometimes very hard to measure after the compression. However, this can be solved by using

the area that can be measured and is visible before and after the test which is usually the middle of the pillar. Secondly, the model assumed the pillar to be in axisymmetric in shape. In our study, although the pillar is asymmetric, but we should also consider the fabrication effect that will lead to sample tapering. In real mechanical work, even when the automated fabrication is employed on the pillar, it is not possible to have a perfect axisymmetric pillar with an accurate fillet radius. Furthermore, this calculation is also limited to a specific range of geometry that has considered the base, pillar and the fillet as the main components for elastic modulus calculations which was not the case in this project.

Chapter 3

Analysis study of Fe_xN thin films and $Fe_xW_{y-1}N$ thin films

3.1 Introduction

In this study, the growth of Fe_xN thin films was carried out by the electron beam vapour deposition process which has the advantage of fabricating dense, high purity films with the flexibility to vary orientation by tuning the deposition parameters.

The first part of the experiments varies the N_2 flow rate given to three samples, and from there we compare the crystallinity by looking at the XRD spectra. The best processing conditions are then used to produce a thick sample for microcompression tests. In order to obtain this, for the second part of the experiment, different temperatures and times were used for these films. Surface tests such as atomic force microscopy (AFM) and X-ray photoelectron spectroscopy (XPS) were used to study the surface morphology of these temperature-dependant thin films and to understand how much iron is incorporated within the film.

Lastly, as we managed to grow a thicker sample so that (TEM) samples could be prepared to check the atomic structure. The experiments were continued to a try to grow a ternary nitride with Tungsten (W) as the second element based on the parameter of Fe_xN thin films which was selected for the compression test. The surface analysis was carried out for these samples to check that tungsten was being incorporated.

3.2 Growth of Fe_xN thin films

Iron based nitrides has been produced using many methods such as dc magnetron sputtering[165] and chemical vapour deposition[97]. However, to our knowledge, none of the iron based nitrides thin films have been synthesised by the electron beam vapour deposition technique. The aim of this study was to prepare the Fe_xN thin films and analyse the structure and composition of the films. Therefore, a number of deposition experiments were carried out with different deposition parameters.

3.2.1 Growth conditions for Fe_xN with different iron (x) content

Iron based nitrides were synthesised using the electron beam vapor deposition technique on a (0001) sapphire substrate in two series. The first one was grown with different target ratio of iron which were x = 0.30, x = 0.33 and x = 0.35. The nitrogen flow rate varies for each of the samples between 1 sccm to 3 sccm respectively. During deposition, the RF power used was 345 W while the temperature was 600°C with varied base pressure of 3.5 x 10^{-4} Torr, 1.0x10^{-4} Torr and 7.5x10^{-5} Torr. The thickness was observed with Dektak profilometer after deposition with a deposition rate of around 2.3 nm/min. The parameters of the samples are presented in Table 3.1.

Table 3.1: Growth series of Fe_xN with x = 0.30, 0.33 and 0.35 grown on sapphire substrate

Fe target ratio	**N_2 flow rate**	**Base pressure**	**RF power**	**Temperature**	**Growth time**	**Thickness**
(x)	(sccm)	(Torr)	(Watt)	(°C)	(min)	(nm)
0.30	3	3.5 x 10^{-4}	345	600	30	72
0.33	2	1.0 x 10^{-4}	345	600	30	68
0.35	2	7.5 x 10^{-5}	345	600	30	70

3.2.1.1 Surface morphology

Figure 3.1 shows AFM images of the different ratio of iron nitrides films. It can be seen that the AFM images exhibit a uniform granular structure as the Fe content increase with the surface which are made from closely packed spherical grains. The root-mean-square (rms) of roughness were around 10 nm, 17 nm and 2 nm for samples with x = 0.30, 0.33 and 0.35 respectively. It shows decreased surface roughness of Fe_xN films with increased of Fe content.

The effect of N_2 flow can also be seen which is presented in Figure 3.1a where when x = 0.30 with 3 sccm of N_2 flow, there were clusters of particles observed on the thin film which may be due to particles agglomeration. As the N_2 flow given to the samples were reduced (3 sccm to 2 sccm) for both iron content of x = 0.33(Figure 3.1b) and x = 0.35 (Figure 3.1c) the shape of the grains became more spherical. It also shows that higher flow rate give a coarser surface on thin films.

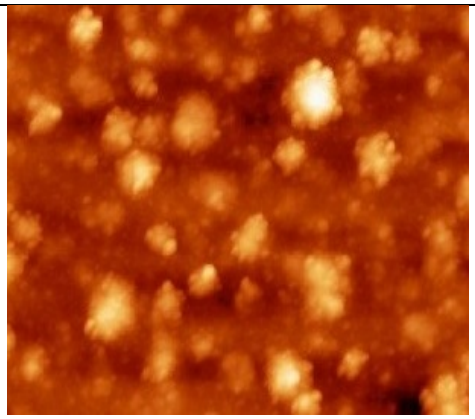
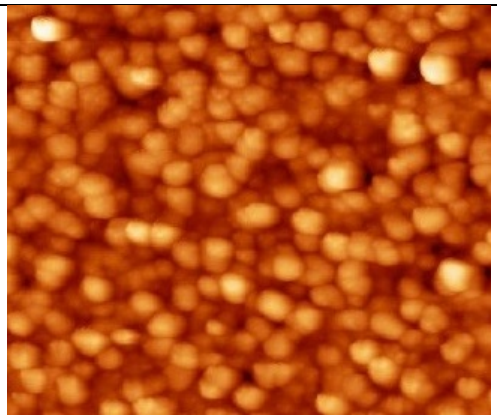
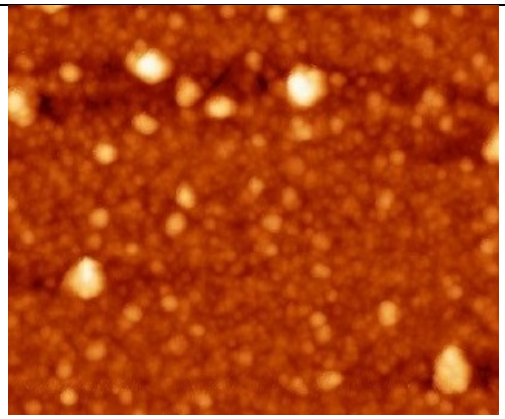
x (Fe content)	on (0001) Sapphire substrate
x = 0.30 N_2 flow = 3 sccm	 Z-scale =34 nm
x = 0.33 N_2 flow = 2 sccm	 Z-scale = 18 nm
x = 0.35 N_2 flow = 2 sccm	 Z-scale = 16 nm

Figure 3.1: 2 x 2 um AFM images of Fe_xN films on sapphire (0001) substrate. All images were processed using parabolic flattening.

3.2.1.2 Structural determination

X-ray diffraction is used to determine the crystal structure and evaluate the crystal quality Figure 3.2 shows a XRD diffractogram of Fe_xN grown on sapphire with different contents of iron which is x = 0.30, 0.33 and 0.35 with N_2 flow of 3 sccm and 2 sccm respectively.

All of the samples had the preferred orientation of iron nitride (Fe_3N) in the (002) plane at 41.65° referring to PDF 00-049-1664 with a hexagonal crystal structure. The peak sits on the same value for these three samples which is shown in Figure 3.2a for x = 0.30, Figure 3.2b for x = 0.33 and Figure 3.2c for x = 0.35. The peak intensity increased with higher content of iron and lower content of nitrogen flow. It shows that for iron content of x = 0.35, the peak is most intense, which indicates a good crystal growth of thin film Fe_3N.

However, as the content of iron increased to 0.33 and 0.35, there was presence of another peak at 89.67°. This peak represents the iron (Fe) (106) planes with a hexagonal crystal structure. This reference was taken from PDF 00-050-1275. The intensity of the iron peaks rises as the iron content increased. The increased content of iron will exhibit more than one phase in a thin film and the nitrogen flow given to the samples were seen to have no effect as there were no iron nitride peak observed.

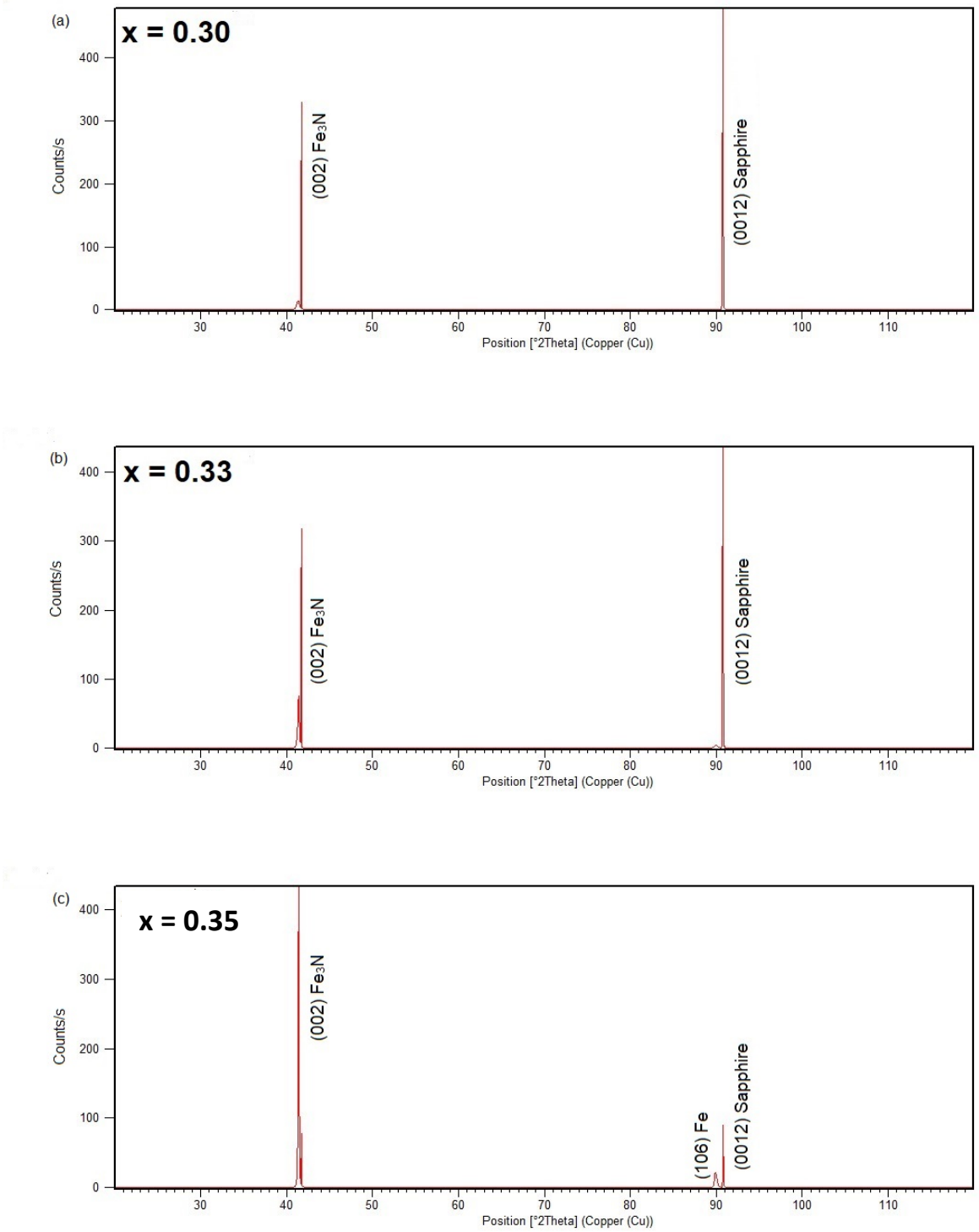


Figure 3.2: XRD peaks of different target ratio of Fe which (a) x = 0.30 with a flow rate of 3 sccm, (b) x = 0.33 with a flow rate of 2 sccm and (c) x = 0.35 with a flow rate of 2 sccm grown on (0001) sapphire.

In order to obtain information about the surface atomic composition on the samples, XPS analysis was performed on the samples with different iron content x= 0.30, 0.33 and 0.35 respectively. Due to the fact that we are focusing on the iron and nitrogen elements on the sample surface, XPS analysis in the binding energy region of these elements was carried out.

The wide scan in XPS measurements for Fe_xN samples can be used to determine the film composition, and the narrow scan to analyse the chemical bonding among the atoms. Since all the Fe and N atom films in the explored samples are within the escape depth of the photoelectrons excited by the incident x-rays, the ratio of Fe $2p_{3/2}$ and N 1s peak areas (Figure 3.3) can be used to determine the average chemical composition of the films.

Figure 3.3 shows the surveys of different Fe contents of the thin films with 1 eV of energy resolution that gives an overall indication of the elements present in the sample being analysed. It can be seen that the content of carbon and oxygen is high due to impurity. There are only small amounts of iron (Fe 2p) and nitrogen (N 1s). There is no peak of nitrogen for iron content of 0.33 with nitrogen flow of 2 sccm. The reason might be that there was not enough energy for the incorporation of nitrogen in the sample with lower gas flow.

For iron content of 0.30, the oxygen peak of O1 s has around 38.04 at.%, carbon peak of C 1s with 29.66 at.%, nitrogen peak with N 1s with 27.76 at.% and iron peak of Fe 2p with 4.54 at. %. As the flow rate was decreased to 2 sccm for x = 0.33, the O1s increased to 58.01 at.%, a similar amount of C 1s of 29.26 at.% and Fe 2p peak at 15. 70 at.%. However, there was no nitrogen peak detected on the XPS spectrum for x = 0.33 sample. This may be due to the fact that there was not enough energy given to the synthesis to break the triple bond of N_2 in order for it to be incorporated in the thin film for the nitrogen to be present on the surface of the films. The content of iron increased up to 0.02 at the same N_2 flow rate and gave the highest

percentage of Fe 2p with 19.11 at.%, low content of nitrogen with 6.65 at.% and lower purity of oxygen and carbon with 52.55 at.% and 21.69 at. % respectively.

From the survey scan of iron with different ratios shown in Figure 3.5, the atom ratio of every element in the samples are given in Table 3.2. Obviously, higher content of iron will give more iron peaks in the XPS spectra. It supported the XRD data which showed no peaks of Fe-N compositions as the N_2 is very little by looking at the N1s peak. There were some peaks that were unidentified. Nitrogen content increased as the flow gas increased but the percentage of iron is very little. Carbon and oxygen appear to be in every sample which indicates contamination.

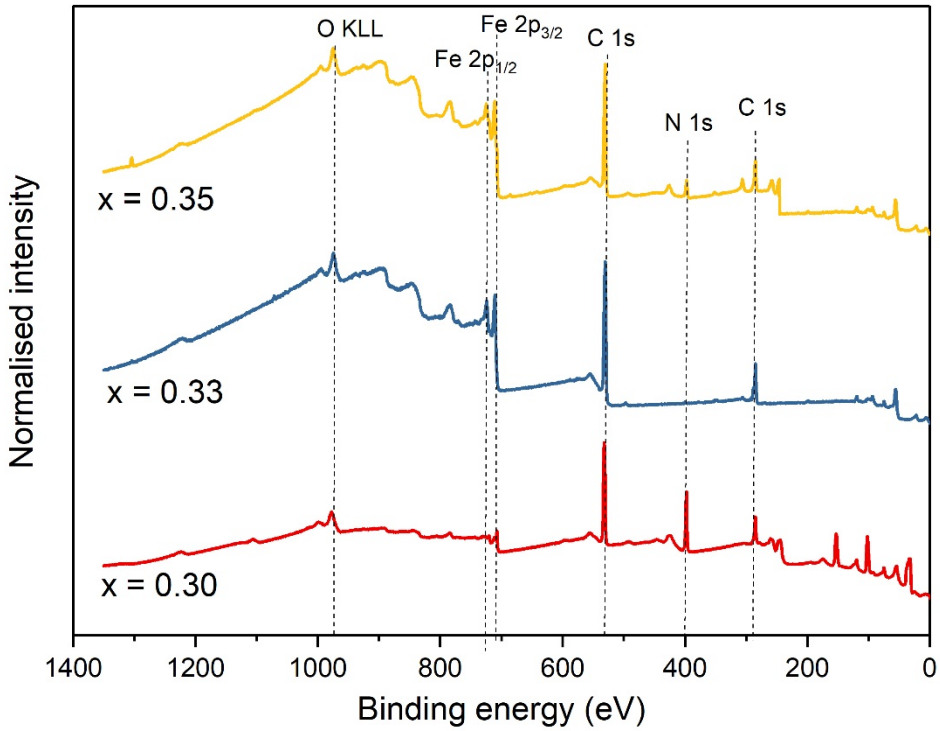


Figure 3.3: XPS survey spectrum for Fe_xN where the target ratio of Fe are (a) x = 0.30, (b) x = 0.33 and (c) x = 0.35 grown on sapphire (Al_2O_3).

Table 3.2: Atomic percentage based survey scan spectra

Fe content (x)	at.%			
	O 1s	**C 1s**	**N 1s**	**Fe 2p**
0.30	38.04	29.66	27.76	4.54
0.33	58.01	29.26	-	15.70
0.35	52.55	21.96	6.65	19.11

Based on the first series of iron-based nitrides growth, it can be concluded that the highest iron target ratio (x = 0.35) with a nitrogen flow of 2 sccm was ideal to proceed with the next growth series. This is because from the XRD data it showed, the highest content of target content of iron and exhibit very intense peak compared to other two ratios. Furthermore, only little peak broadening was observed, which suggests a good crystal quality. Peak broadening in the diffractogram may indicate smaller crystallite size in nanocrystallline materials, more stacking faults, microstrain and an inhomogeneous composition in the material[166].

Although the target ratio of Fe of x = 0.3, the sample did not show nitrogen presence in the XPS analysis, we believe that the nitrogen incorporation is there as the XRD diffractogram showed similar peaks compared to other two parameters (x = 0.30 and x = 0.35). Furthermore, XPS analysis conducted on these samples were only a survey spectrum which only occurred at the surface of the films.

Thin films with target iron ratio of x = 0.35 were selected as they showed a good crystalline thin film quality based on the XRD and showed the presence of nitrogen element on the thin film surface. Furthermore, we selected x = 0.35 growth parameters as the next series due to the fact that we believe that the synthesis used much lower base pressure compared to the other two samples and we believed that lower base pressure with higher temperature will hinder the presence of oxides and contamination on the thin films.

3.2.2 Growth conditions for Fe_xN with different growth time

As the crystal quality and the elemental presence in these films were investigated using XRD and XPS, the highest content of iron was selected to proceed with the next series of growth. These thin films were grown with a higher deposition rate in order to achieved thicker samples with a constant temperature of 1000°C for 30 minutes and 3 hours of deposition time with a deposition rate of 3.6 nm/min. All the parameters were shown in Table 3.3.

Table 3.3: Growth series of Fe_xN (x = 0.35) at 1000°C for 30 minutes and 180 minutes grown on sapphire substrate

Fe target ratio	N_2 flow rate	Base pressure	Temperature	Growth time	Thickness
(x)	(sccm)	(Torr)	(°C)	(min)	(nm)
0.35	2	7.5×10^{-5}	1000°C	30	108
0.35	2	7.5×10^{-5}	1000°C	180	653

3.2.2.1 Surface morphology

AFM images of samples with higher temperature (1000°C) with two different growth times, 30 minutes and 3 hours respectively is shown in Figure 3.4. It can be seen that as the temperature is increased to 1000°C, there was formation of small grains on the sample surface with the height of grains more than 100 nm (Figure 3.4a and Figure 3.4b). This occurred because as the growth temperature increased with longer growth time, the lateral growth was enhanced, and coalesced film was formed as presented in Figure 3.4b for the sample with 3 hours of growth time.

The root-mean-square (rms) of roughness value of 30 minutes is 106 nm while for 3 hours is 80 nm respectively. A similar trend was observed on the different growth temperature of Fe_3N by Tao *et al.*[167]

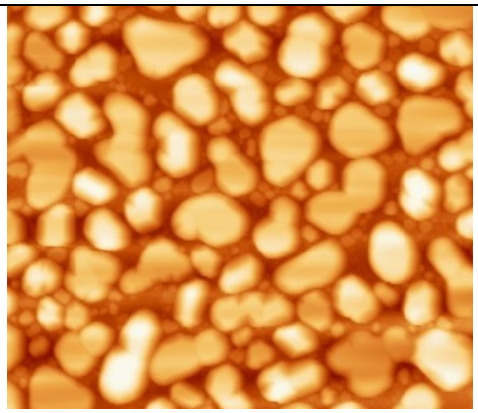
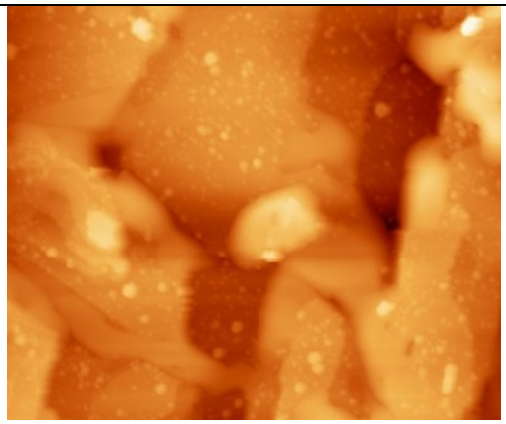
x = 0. 35	on (0001) Sapphire substrate
Time = 30 minutes	 Z-scale = 269 nm
Time = 3 hour	 Z-scale = 306 nm

Figure 3.4: 2 x 2 um AFM images of Fe_xN films on sapphire (0001) substrate under 1000°C with (a) 30 minutes and (b) 3 hour of growth time with FexN (x = 0.35) in N_2 flow of 2sccm. All images were processed using parabolic flattening.

3.2.2.2 Structural determination

Figure 3.5 shows a Fe_xN growth with 1000°C with different growth times. A longer deposition time gives higher intensity peaks in the diffractogram. There are two phase presence in both of the samples. One can assumed that another phase may have developed during the growth of this thin films as the intensity of the peaks was higher with increasing temperature. The peak at 41.58° and 44.64° is labelled as Fe_3N in (002) and (200) planes. These planes are referred to as PDF 00-049-1664 and have a hexagonal crystal structure. One more ferrite peak is present

in the 98.94° in the (220) with a cubic structure with a reference of PDF 00-006-0696. The diffraction peaks shift towards low angles with increasing iron content which is shown in Figure 3.4b. This indicates the incorporation between N atoms to the Fe_xN results in the expansion of unit cells[168,169].

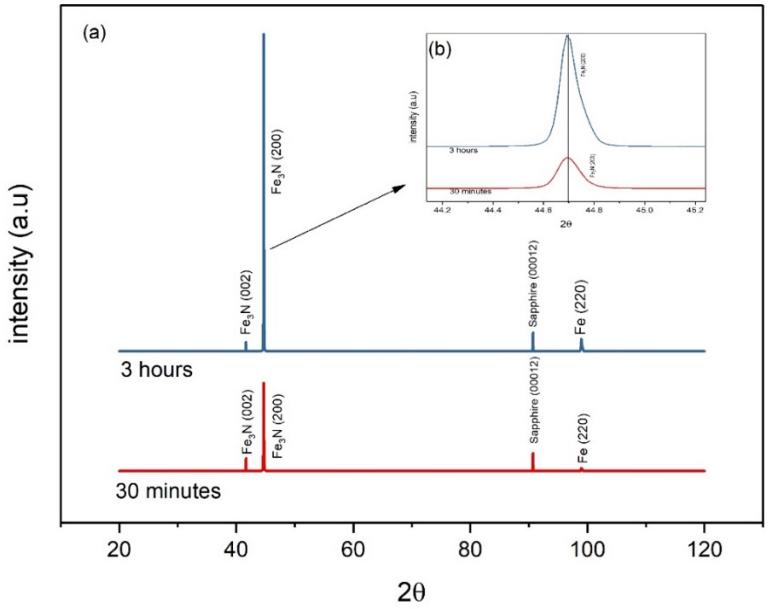


Figure 3.5: XRD peaks of Fe_xN thin film grown on (0001) sapphire for (a) different growth times of 30 minutes and 3 hours at 1000°C and (b) enlarged peak of Fe3N (200) where it shows the occurrence of small peak shifts occurred.

Prolonged growth time produced intense peak, and this will affect the quality of the thin films, which clearly from the XRD data shows better crystalline film. This might be because more active adatoms between iron and nitrogen are present which leads to smoother surface and it also gives more time for iron and nitrogen to be fully incorporate compare to 30 minutes sample. However, we did not manage to grow an epitaxial film as there were other phases were present. Despite the general diffraction pattern of Fe_3N, the diffraction peaks of the films deposited at higher temperature exhibited gradual shifts towards the lower angle values,

indicating lattice expansion of the obtained Fe_3N thin films which is in agreement with a previous study[170]. The issue was also seen in the thin film grown with pulsed laser deposition (PLD) method. Usually, for a good epitaxial growth, method like molecular beam epitaxy (MBE) is more preferable.

XPS analysis of two samples with different growth times at 1000°C was carried out to analyse the elemental contents and chemical states in the samples and is presented in Figure 3.6. The XPS analysis of Fe and N was conducted and it can be seen that there was presence of N1s, O1s, C1s, Fe2p and Fe3s and Fe3p peaks on both of the sample. The different N1s bonding energies represent the different environments around the nitrogen atoms in the film[27,71].

For thin film with 3 hours growth, oxygen peak (O 1 s) is minimal, which indicates that the prolonged growth time has exhausted the extraneous oxygen. Hence, minimal oxygen is detected with thicker thin film. It can be indicated that only one chemical bonding state occurred as there was only one main peak of Fe 2p for 30 minutes of growth time of Fe_xN, meanwhile two or more bonding states may occur in the 3 hours growth as there was more than one main peak that appeared on the XPS spectrum. One main peak for Fe 2p and N 1s indicates that there is only one chemical bonding state in the film which is shown in the 30 minutes XPS survey.

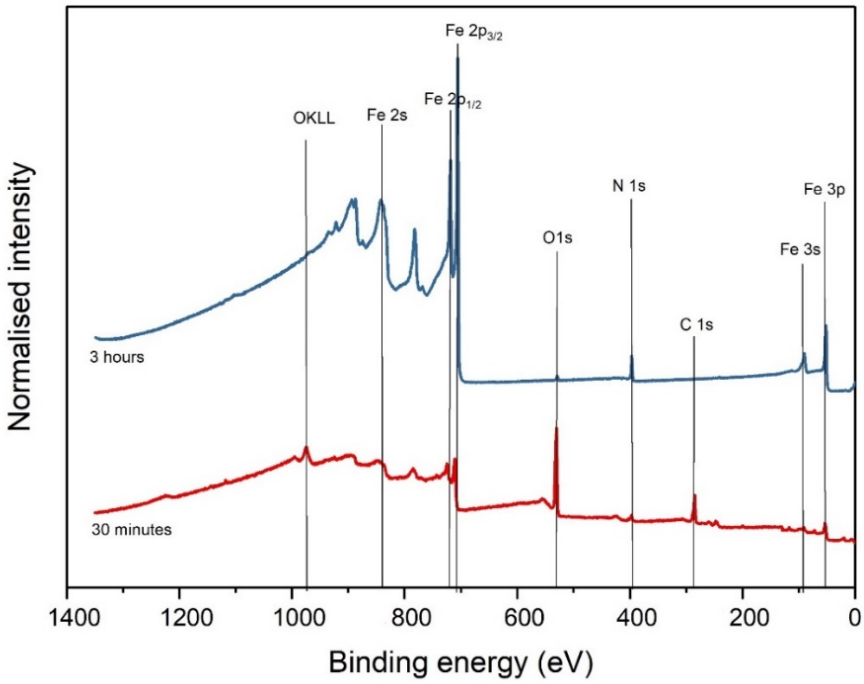


Figure 3.6: XPS survey spectrum for Fe_xN where x = 0.35 at 1000C for (a) 30 minutes and (b) 3 hours.

The high resolution scan for Fe 2p of both 30 minutes and 3 hours samples were shown in Figure 3.7a. For both samples, Fe $2p_{3/2}$ band gives the binding energy of 711.3 eV and 710.8 eV which can be assigned to the binding energy of Fe^{3+} and Fe^{2+}. For the peak of Fe 2p1/2, the peak of 3 hours (732.2 eV) and 30 minutes (732.8 eV) may described as Fe^{3+}. The binding energy of Fe 2p could be related to the N coordinated Fe^{3+} or Fe^{2+} which is supported by previous references[171,172]. After the samples were etched for 600 seconds, which is shown in Figure 3.7c, Fe $2p_{3/2}$ peaks give the value of 706 eV for both of the samples, while for Fe $2p_{1/2}$, the 719.9 eV and 719.9 eV binding energy were found. Both of the peaks may be attributed to the orbitals of metallic iron[173].

Figure 3.7b presents the core line spectra of N 1s as the received sample which gave a peak of 396 eV for the sample with 3 hours growth and 396 eV and 402 eV for the sample with 30

minutes growth. Hui et al.[174] reported four types of nitrogen species which are pyridinic with the range of binding energy between 397 eV to 399 eV, pyrolic between 400.2 eV to 400.9 eV and quaternary/oxidised is between 401 eV to 403 eV respectively. Some of the binding energy between 396 eV to 399.5 eV may also include the contribution from metal nitrogen bound to metal[175], which is also found in this study, where the N 1s peak of 396 eV in both samples.

The peak of 402 eV of the 30 minutes sample can be assigned to the quaternary or oxidised nitrogen (3.7 (b)). The presence of oxygen on the surface of thin films is possible because of the exposure of the samples in the atmosphere during and after thin film deposition. However, when the thin film is etched for 600 seconds (Figure 3.7 (d)), the reduction of the oxidised peak suggests that the oxidation layer is removed from the sample's surface and suggests that the thin films is of iron-nitride species and not iron-oxides.

As the samples undergo etch treatment for depth profiling, the N 1s spectra shows the main peak shifting to 397 eV and 396 eV, for both the 3 hours and 30 minutes samples, that is assigned to the pyridinic nitrogen group. These peaks correspond to metal-nitrogen bonding as reported by previous researcher. Interestingly, post-etching of 600 seconds for 30 minutes samples shows a presence of a peak at 393 eV. According to Prieto *et al.*[166], this could be due to the establishment of artefacts/impurities of the sample surface as the top layer being etched. During the depth profiling, this layer removal which consists of these impurities on the film surface was sometimes accidentally measured together with the photoelectron signal which is reflected in the XPS spectra.

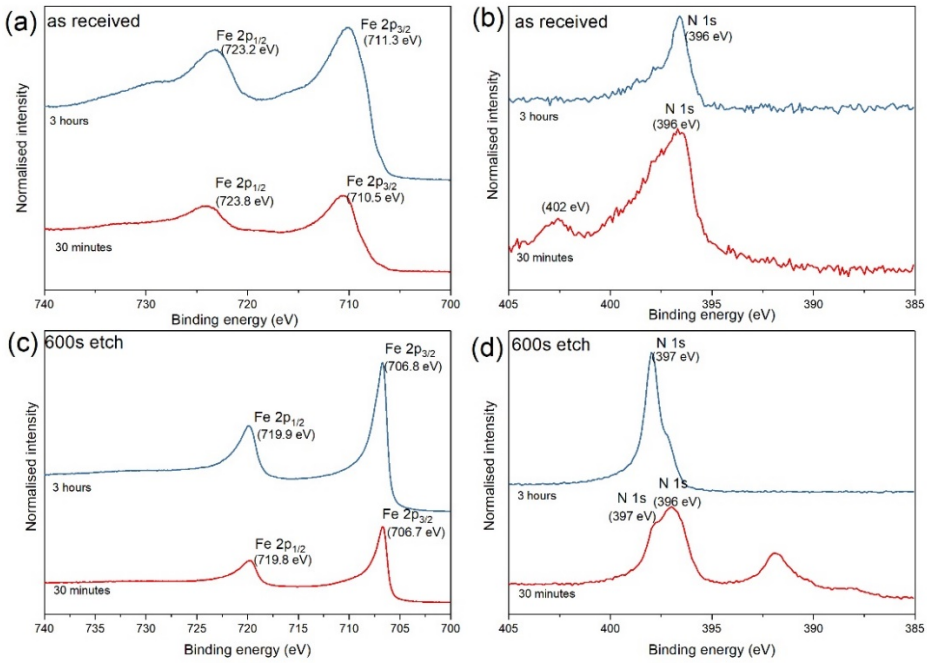


Figure 3.7: XPS core line spectra of Fe2p (a) 30 minutes and (b) 3 hour of growth time for x = 0.35 at 1000°C. The red line is as the received sample while the blue indicates after 600 seconds of etching.

The sample with longer growth time was taken for further investigation with TEM in order to determine the thickness and crystal structure as this sample will be subjected to microcompression test. The microstructure of Fe_xN of x = 0.35 with 2 sccm of N_2 flow at 1000°C for 3 hours grown on sapphire is shown in Figure 3.8. The bright field image shows the thin film with a thickness of 600 nm. It was also observed that some beam damage occurred on the sample especially on the substrate area.

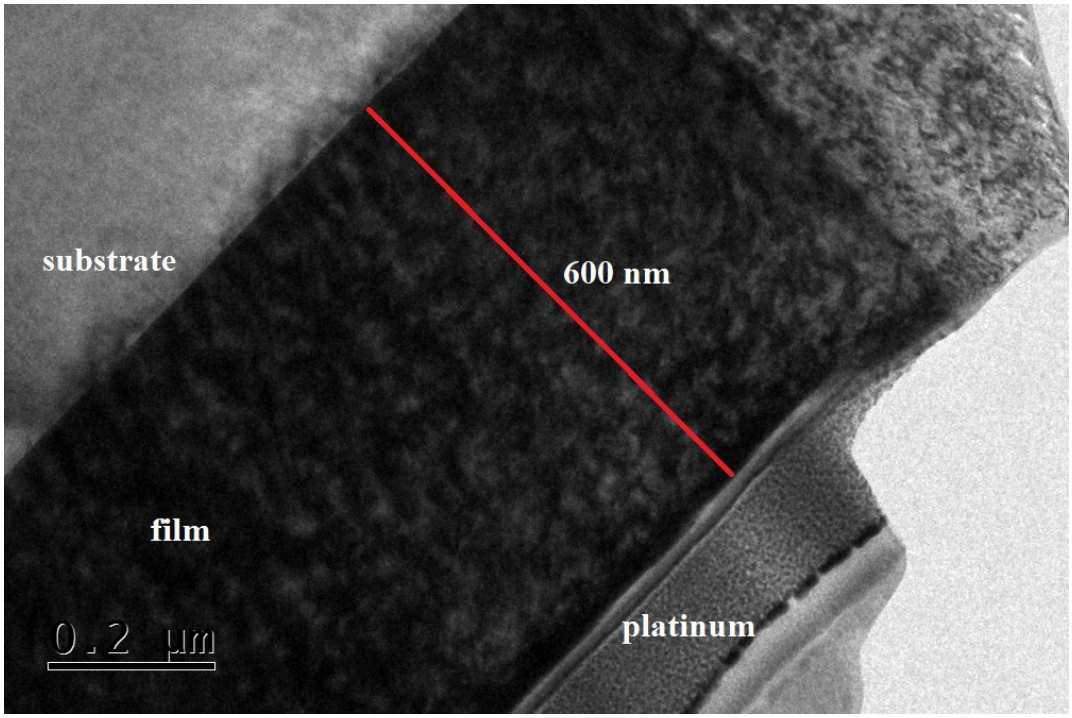


Figure 3.8: TEM Bright field image of Fe_xN (x=0.35) thin films on sapphire showing thickness in the range of 600 nm.

Figure 3.9 presented a selected area diffraction pattern (SAED) of both thin film and substrate. The SAED of film shows a hexagonal crystal structure with a [0001] beam directions is observed in Figure 3.9a. Considering the corresponding selected area diffraction patterns for the cross section of the film with highest amount of iron content x = 0.35 with temperature of 1000°C for 3 hours, it shows hexagonal diffraction patterns and this agrees with the XRD results indicating that it is Fe_3N structure. Meanwhile the diffraction pattern of substrate is shown in the zone axis of [-12-16] in Figure 3.9b which is also in a hexagonal crystal structure.

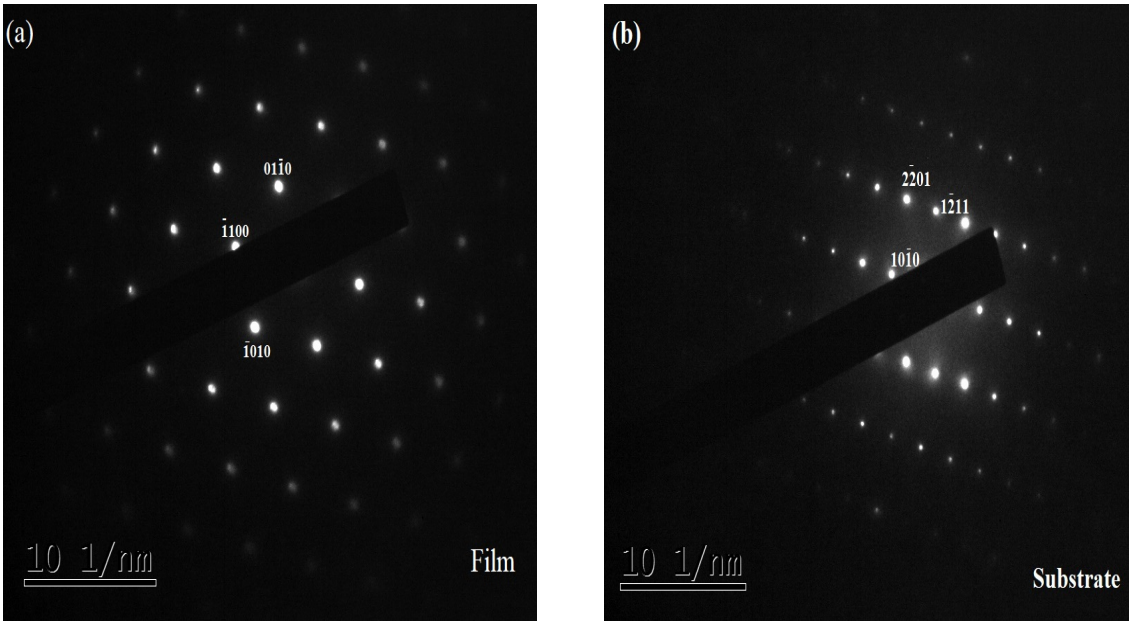


Figure 3.9: Selected area diffraction pattern of (a) film with zone axis of [0001] and (b) substrate with zone axis of [12-16]. Both of the images are showing diffraction of hexagonal crystal structure.

High resolution images were further demonstrated to observe the fine structure of Fe_xN thin film. The result in Figure 3.10a shows that both film and substrate have hexagonal crystal structures. Further investigation was carried out to determine the d spacing of the thin films and it was found that there were two different distinct areas with d spacing of 0.23 nm and 0.29 nm which corresponds to [01-10] and [1-100] directions. The values obtained were then compared to PDF 00-049-1664 of XRD reference and it was found that both of d spacing values of [01-10] and [1-100] directions of 0.21nm and 0.29 nm correspond well to (11-20) and (10-11) crystallographic plane of hexagonal Fe_3N.

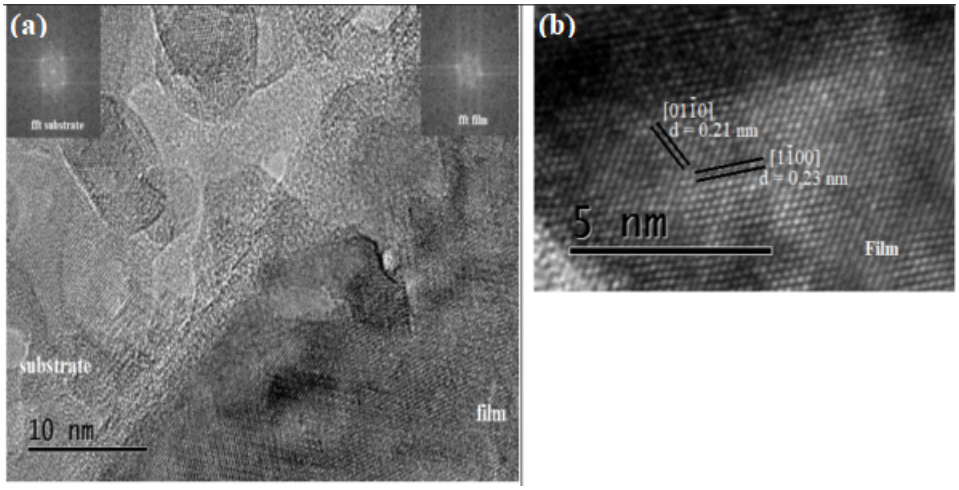


Figure 3.10: HRTEM images of sample with (a) film and sample shows a hexagonal crystal structure and (b) and higher resolution on the film to check the d-spacing for both [01-10] and [1-100] film directions.

3.3 Growth of $Fe_xW_{y-1}N$ thin films

Recently, few ternary nitrides have been synthesised and fully characterised, in part because the nitrides have low decomposition temperatures and it is believed that these ternary nitrides developed a MAX phase which exhibits better properties compared to its binary materials. This Fe-W-N nitrides were previously obtained by the temperature programmed reaction (TPR) by using appropriate amounts of Na_2Wo_4 and $FeSO_4.7H_2O$ with varied atomic ratio of Fe/Fe-W [176] and ammonolysis of transition metal tungstate ($FeWO_4$)[177], both on thin films. No research or study has been conducted on the attempt of the synthesis of $Fe_xWy_{-1}N$ to date. Therefore, this preliminary study is crucial in order to understand what parameters are suitable to obtain the single phase of FeWN thin films.

3.3.1 Growth conditions of $Fe_xW_{y-1}N$

A set of $Fe_xW_{y-1}N$ samples were grown where the total flux of Fe+W is kept as close to constant as possible, but the relative proportion of Fe and W are changed, to produce a composition series. The iron (Fe) was kept constant while the target ratio of tungsten is varied to y = 0.32,

0.33 and 0.34 respectively. The temperature and base pressure of these series were kept constant throughout the experiment with a deposition rate of 2.3 nm/min. Table 3.4 shows all the parameters for these three ratios. Further investigation was carried out for general characterisation to determine whether we are able to synthesise $Fe_xWy_{-1}N$ thin films such as AFM to check the surface morphology and XRD and XPS for structural determination and to have an overview of what materials were formed during the synthesis of these thin films.

Table 3.4: Growth series of $Fe_xWy_{-1}N$ with different ratio of y = 0.32, 0.33, 0.34 grown on sapphire substrate

W target ratio content	**N_2 flow rate**	**Base pressure**	**RF power**	**Temperature**	**Growth time**	**Thickness**
(x)	(sccm)	(Torr)	(Watt)	(°C)	(min)	(nm)
0.32	2	7.5×10^{-5}	400	600	30	68
0.33	2	7.5×10^{-5}	400	600	30	64
0.34	2	7.5×10^{-5}	400	600	30	62

3.3.2 Surface morphology

The surface roughness of the $Fe_xW_{y-1}N$ films decreased as the W content increased. There were only small changes of the AFM images between these three samples (Figure 3.11). The samples with lower W content have lower roughness which is around 0.98 nm, 0.69 nm for W of y = 0.33 and 1.56 nm for W content of y = 0.34. It is also can be seen that the W rich samples have higher roughness due to the higher grain size and the continuous bombardment which results in collisions and finally produced a rougher surface. The same behaviour was also observed in other ternary nitrides such as Ta_xMe_{1-xN} where M = Hf, Nb, Mo and W[178].

A similar trend has been reported from metalorganic chemical vapour deposition (MOCVD) grown films of Sc_xGaN on sapphire[167] where the decrease of lateral feature size was attributed to the decrease in average surface adatom mobility. The decreasing of feature size will correspond to the higher diffusion barrier height related to the increased of surface concentration of the transition metal elements, as well as the lower mobility of the transition metal atoms on the surfaces[85,179]. The low surface roughness of lower Fe content is resultant of low deposition rate which in turn ensured the stoichiometry throughout the film[180].

The growth in particle size of each sample is influenced by the increased strength of the bonding between nitrogen and the tungsten material where a similar trend was observed in the growth of WN film with dense plasma focus method[181]. It was reported when using ions with different energies will give different surface roughness on the thin film samples.

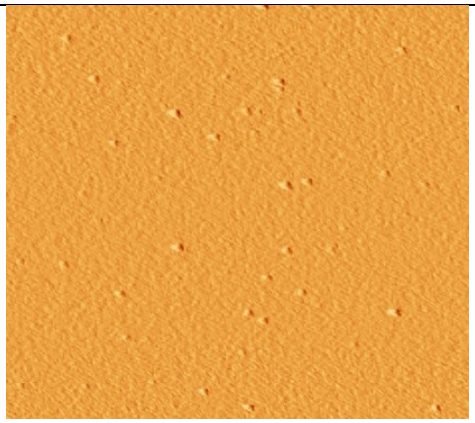
y (W content)	on (0001) Sapphire substrate
0.32	 Z-scale = 17 nm
0.33	 Z-scale = 18 nm
0.34	 Z-scale = 20 nm

Figure 3.11: 2 x 2 um AFM images of $Fe_xW_{y-1}N$ films on sapphire (0001) substrate. All images were processed using parabolic flattening.

3.3.3 Structural determination by XRD and XPS

Figure 3.12 shows XRD diffractogram of different tungsten ratio. We can see the presence of iron nitride (WN) in the (111) and slight grown of WN in (222) plane for all samples with y content of 0.32, 0.33 and 0.34 of tungsten. The peak intensity of Fe_3N in (002) is observed in the samples which indicates that the films were grown on these plane directions. However, as the percentage of tungsten is at y = 0.34, the intensity of WN decrease with the presence of tungsten in (110) plane.

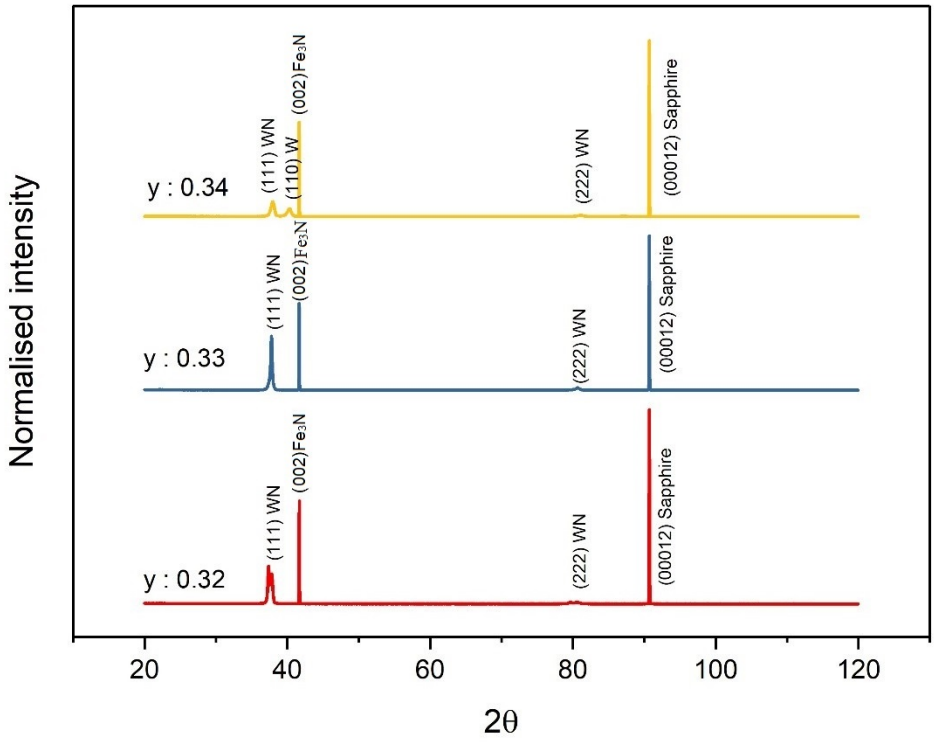


Figure 3.12: XRD of $Fe_xW_{y-1}N$ with (a) y = 0.32 (b) y = 0.33 and (c) y = 0.34 with 600°C with 7.5 x 10^{-5} of base pressure.

The XPS spectra of wide scan for three samples with different tungsten ratio is presented in Figure 3.13. It can be observed that the presence of a few elements which are carbon, namely nitrogen and tungsten. There were no peaks for elemental iron which indicates that the iron

was not incorporated into the surface of each samples. For the lowest tungsten ratio, the C1s peak indicate around 85.13 at.%, O1s peak around 9.15 at.%, N1s peak around 4.78 at.%, and W4d peak around 0.94 at.% for carbon, oxygen, nitrogen and tungsten element. As the tungsten ratio increased y = 0.33, carbon percentage is around 72.07 at.%, oxygen percentage is around 9.82 at.%, nitrogen peak is around 6.52 at.% and tungsten peak is around 1.58 at.% respectively. Lastly, for the tungsten ratio of y = 0.34, the atomic percentage were 38.85 at.%, 17.98 at.%, 20.84 at.% and 2.52 at.% for carbon, oxygen, nitrogen and tungsten respectively. Table 3.5 summarizes this data.

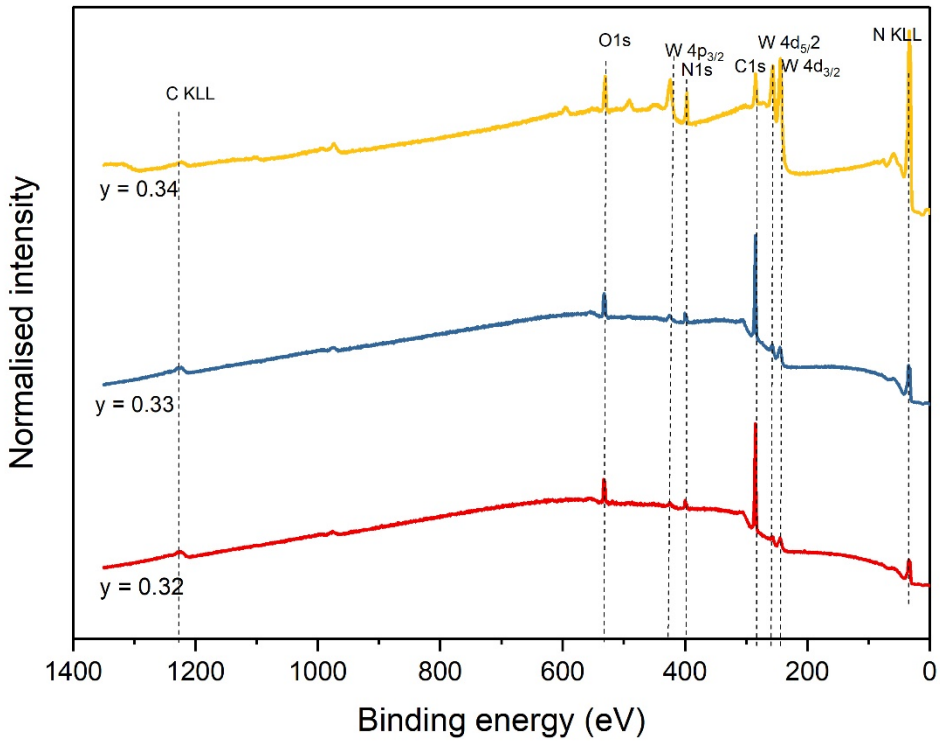


Figure 3.13: XPS survey spectrum for Fe_xN where (a) y = 0.32 (b) y = 0.33 and (c) y = 0.34 with 600°C grown on sapphire (Al_2O_3).

Table 3.5: Atomic percentage of $Fe_xW_{y-1}N$ based survey scan spectra

W (y)	at.%				
	O 1s	**C 1s**	**N 1s**	**Fe 2p**	**W 4f**
0.32	9.15	85.13	4.78	-	0.94
0.33	9.82	72.07	6.52	-	1.58
0.34	17.99	38.65	20.84	-	2.52

From Table 1, it is obvious that the ratio of iron in the synthesis is not proportionate with tungsten ratio for the iron and tungsten binding to take place. Oxygen percentage is proportional to the tungsten ratio. However, we could not confirm is there is any formation of tungsten oxide because from the XPS, there is no peak of tungsten oxide present. This may be due to the fact that it is very hard for the Fe-W-N to take place as one of the challenges of growing nitrides is their strong bonding and it is very unstable[61]. Furthermore, the synthesis of ternary nitrides is not straightforward as the free energies of formation are small, thus hindering the direct synthesis using elemental nitrogen at high temperatures especially via EBPVD technique [29,182].

Figure 3.14 shows three samples of y = 0.32, 0.33 and 0.34 of as received, 60 second of etching, 120 seconds of etching and 180 seconds of etching. After 180 second of etching, carbon contamination was removed, and the concentration of W became uniform for all of the samples. For the tungsten y = 0.32 which is shown in Figure 3.14a, there was no iron peak observed.

A small peak of Fe 2p with spin orbital was observed only in tungsten with y = 0.33 after 60 seconds of etch (Figure 3.14b). A higher content of tungsten is observed even in as received samples of y = 0.34 (Figure 3.14c) which indicates that the presence of tungsten is abundant in the thin film especially in the W 4d spin orbitals.

One more characteristic highlighted in the XPS depth profiles, is initially strong and stable oxygen concentration which indicates the formation of stronger iron and tungsten bonding to oxygen rather than Fe-N and W-N bond[183]. The absence of iron in the system maybe contributed to nitriding mode during the deposition, in which nitrogen ion is dominating the growth. Thus, capable of diminishing a weaker bond which is reactive Fe ion emission instead of W ions.

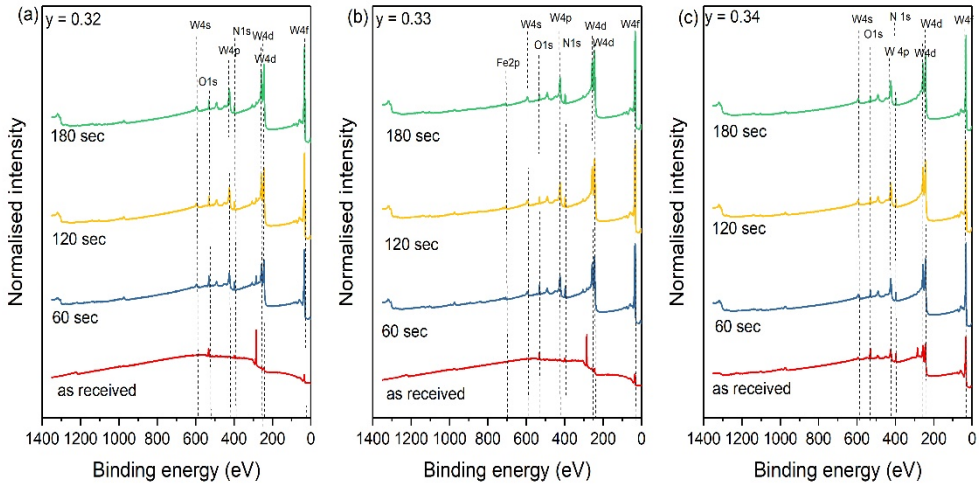


Figure 3.14: XPS depth profiling spectra of $Fe_xW_{y-1}N$ film on (a) y = 0.32 (b) y = 0.33 and (c) y = 0.34 at 600°C. The red line is as received sample, blue indicates after 60 seconds of etching and yellow and green indicates 120 second and 180 second of etching.

3.4 Discussion

From all the data presented above, the first series of growth results in the formation of Fe_3N thin film. This can be seen by the results in both XRD and XPS. The first series of growth on the different percentages of iron target ratio with x = 0.30, x = 0.33 and x = 0.35 showed that parameters with lower base pressure is subjected to a good vacuum system, which is capable of eliminating contamination of other elements in the system before, during, and after the deposition such as oxygen and carbon.

Furthermore, a lower base pressure also leads to the formation of a lower nuclei density on the thin films which results in a better crystallinity, while a higher base pressure correlates with the formation of defects, which is also supported by previous research on the effect of base pressure on the thin film development[184,185]. For example, thin films with iron target ratio of x = 0.33 has a higher base pressure compared to iron target ratio of x =0.35. It also has highest oxygen content (O 1 s) with 58.1 at. %, while no nitrogen peak is present in the XPS survey scan spectra.

Although for the iron target ratio of x = 0.33 there was no nitrogen presence, it can be predicted that there is still nitrogen existence in the thin films if depth profiling is carried out on the sample. Such a test was uncritical as this preliminary study was carried out to provide basic information on the reliability of the growth parameters and see whether we have succeeded in the growth of iron-nitrides based thin films. The focus of the project is on the development of iron nitrides thin films with higher growth temperatures.

Furthermore, the influence of base pressure on the growth of thin films is supported by Frankel *et al.*[186], who reported that when comparing the performance between thin films and bulk samples, the quality of the vacuum in the deposition chamber plays an important role. This is because, the pressure increases during deposition but the residual contaminant gas in the system will depend on the base pressure prior to deposition.

Increasing N_2 flow will result in high dissociation energy of N_2, which also leads to decrease in the deposition rate of thin film[187]. A similar trend was also observed in the study of magnetic properties of iron nitride films via DC sputtering with different flow rates of nitrogen and iron[80], where higher content of iron will increase the deposition rate, thus resulting in thicker samples.

The major influence of temperature is reflected on the samples once the samples were grown from 600°C to 1000°C. For the second series, Fe_3N thin film were grown on a sapphire substrate. However, we did not grow epitaxial thin film as there is another phase of iron present. Based on the phase diagram, growth temperature that is higher than 600°C is predicted to form alpha phase of iron species. Similar phenomena is also observed by a work conducted by Prieto *et al.*[166]. The rise of temperature will also increase grain size, which reduces the available surface of the nitrogen uptake[188]. This latter effect can be seen with the increase of peak intensity in the XRD data which is sharper and more pronounced compared to samples with lower temperature.

From the XRD diffractogram, it was also observed that there were peak shifts between thin films grown at 30 minutes and 3 hours. A similar trend was also observed in the growth of TaN films where the peak shifts to a lower angle, indicating a change in composition, and there was also presence of residual stress in the thin films[189].

A study conducted by Rissanen *et al.*[90] reported that the pure FeN phase changed to ε-phase when the temperature applied to the samples is higher than 400°C. The changes in phase were also contributed by the increased content of Fe incorporated in the thin films. A higher temperature also shows a homogeneous growth compared to a lower temperature.

Nitrogen is highly mobile within the Fe-N lattice owing to its interstitial character and the presence of a large number of vacancies on the octahedral sites and it is interstitial with the Fe-N lattice. This will lead to the diffusion between the different crystallographic sites with prolonged growth condition is given to the structure[190]. That is why we can see the presence of Fe_3N on the samples as the increase of growth rate will help to make nitrogen be fully incorporated with the structures.

This is also supported by the presence of Fe 2p species in the XPS spectrum which indicates that there is presence of Fe-N bonding; that is, when the peaks are shown to be at 723 eV, this usually indicates coordination between nitrogen to Fe $^{3+}$ or Fe^{2+} species. Oxygen was also not visible in the spectrum for both samples in the spectrum. The reason may be attributed to the use of lower base pressure, which results in the sample containing a lower amount of oxygen and as the system chamber is already stabilised and free from extraneous impurities.

A thicker thin film was grown by prolonging the growth time up to 3 hours. It is observed that the main active material during the growth process is ionised Fe atoms in the presence of nitrogen gas. As the growth time increases with high temperatures, the nitrogen ions are more active in the chamber and the intensity of nitrogen emission increased during depositions. This is supported by recent observations[191] which show that the degree of filling in the non-metallic sub lattice of the nitride increases linearly as the parameters such as time and temperature increases. This results in the higher content of nitrogen in thin films for a thicker thin film[192,193].

As we are also interested in the ternary nitrides compositions, it was found that tungsten content of y = 0.34 with iron content of 0.35 is more favourable, as from the XPS data it can be seen that there was presence of nitrogen, iron, and tungsten elements even after 180 seconds of etching.

However, a ternary nitride thin film ($Fe_xW_{y-1}N$) growth was unsuccessful. One of the issues is the synthesising routes. Ternary nitrides have successfully been grown by synthetic methods such as $LiMoN_2$ and $CoMoN_2$[182,190,194]. Bem *et al.*[177] chose ammonolysis approach to grow ternary nitrides of $FeWN_2$ by using oxide precursors, $FeWo_4$ in order to obtain $FeWN_2$. The inductive effect of the route plays an important role in stabilising the metal to nitrogen bond by the donation of electrons from an electropositive element. During ammonolysis, it offers the inductive effects during the process which stabilised the metal to nitrogen bond by donation

of electrons from an electropositive element which occurred during ammonolysis routes for example.[27,55,195].

In the absence of this induction effect stabilisation, the formation of binary nitrides is rather in favour compared to ternary nitrides. This approach limits the number of potential new ternary nitrides to be developed by other thin film techniques such as sputtering, MBE, and MOVPE. Due to its complication in synthesising ternary nitrides, no research has been conducted on the growth of $Fe_xW_{y-1}N$ thin films using EBPVD technique to date.

3.5 Summary

The synthesis of Fe_xN were carried out in two parts where the first part was increasing the iron content with 2 sccm N_2 flow. It was found that only ferrite was formed but, the XRD data indicates a good crystalline structure with the intense peak given by the samples of Fe (x=0.35). Further investigations were carried out with higher temperature using the same parameter with target iron content of x = 0.35 for two different growth time which are 30 minutes and 3 hours.

It was found that with a higher temperature, Fe_3N compositions were developed but it was not in a single phase as another ferrite peak was observed in the XRD data. Supported by the XPS data, it was indicated that there was formation of either Fe^{2+} or Fe^{3+} in the samples. Furthermore, TEM images confirmed that the film is in hexagonal structure which corresponds to Fe_3N.

As we selected the 3 hours growth time for the microcompression test, an attempt to grow ternary nitrides was carried out with a different iron-to-tungsten ratio. However, we only managed to obtain Fe-N and W-N composition and a limited amount of iron presence on these samples. It was found that either the iron has been oxidised or some iron oxides or tungsten oxides were formed during the synthesis.

Chapter 4

Preliminary study of microcompression:MgO (100) and MgO (110)

4.1 Introduction

This preliminary study was conducted by using one material in two orientations MgO (100) and MgO (110). To allow elastic modulus measurements to be carried out, micropillars were fabricated into each sample using a focused ion beam.

This initial stage of experiment was required and crucial because there are only few available references that conducted studies on microcompressed thin films. Furthermore, these studies did not concentrate on the thin films' elastic modulus measurements. Therefore, by using microcompression of MgO as the control experiment, one will be able to know whether the microscopic sample is acceptable and in agreement to its macroscale sample by comparing the value of their elastic moduli.

Among the families of MgO (100), (110) and (111), MgO (100) is the softest amongst them, while MgO (110) is the midpoint of stiffness between MgO (100) and MgO (111). One of the reasons the testing was conducted on MgO (100) and MgO (110) is because this material has a cubic structure, therefore, the calculation of its Young's modulus will be straight forward and their references in terms of elastic moduli are widely available from previous studies.

The experiments were conducted to compare the Young's modulus obtained for both MgO (100) and MgO (110) under microcompression with the available references. We also want to

make sure this method is relevant to use for thin films as Chapter 5 will be focusing on the thin films' microcompression.

4.2 Micropillar fabrications and microcompression experiment

MgO bulk samples were obtained directly from Pi KEM and were cut to 1 mm x 1 mm and placed onto the stub before placing them into the FIB chamber. Pillars were fabricated on both of the samples with FIB (Helios NanoLab 600) using NanoBuilder software. Each samples had three micropillars that were approximately in 3.0 ± 0.5 μm in diameter and 9.0 ± 0.5 μm in height which follows the aspect ratio of 1 : 3 (diameter to length of the pillar ratio). For all the pillars, in this project, the diameter of the pillar is taken from the average of top, middle and bottom part of the pillars.

There are two micropillars in total for each of the samples. Each pillar underwent 5 cycles of loading and unloading compression, which gave the load-displacement relationship. This curve is then converted to a stress-strain curve with the assumption that the pillar is uniformly deformed.

The cycles typically consist of three segments during microcompression which are (i) the loading segment, (ii) an intermediate segment where the maximum load is held constant and (iii) the unloading segment. The purpose of introducing a hold time at maximum compression load is to minimise any adverse effects on the measurement of stiffness on the curve. During the loading, the material deforms vertically downwards vertically beneath the indenter until maximum load is achieved.

4.3 Results

4.3.1 Microcompression of MgO (100)

The load displacement curves obtained during 5 loading cycles of the three micropillars samples which were loaded under the displacement control and to a maximum set of displacements are shown in Figure 4.1.

The graph in Figure 4.1 represents the load-displacement curve of one of the pillars after it has been corrected by a surface test (which was carried out by placing the flat punch on the sample flat surface) that was conducted before microcompression was carried out. The surface test was conducted for correcting not only the initial misalignment issue between the pillars and the flat punch, but also the compliance given by indenter system. The stiffness obtained from the surface test was then accounted for by the analysis of the load-displacement curves. Similar approach is conducted on all the microcompression samples throughout the course of this project.

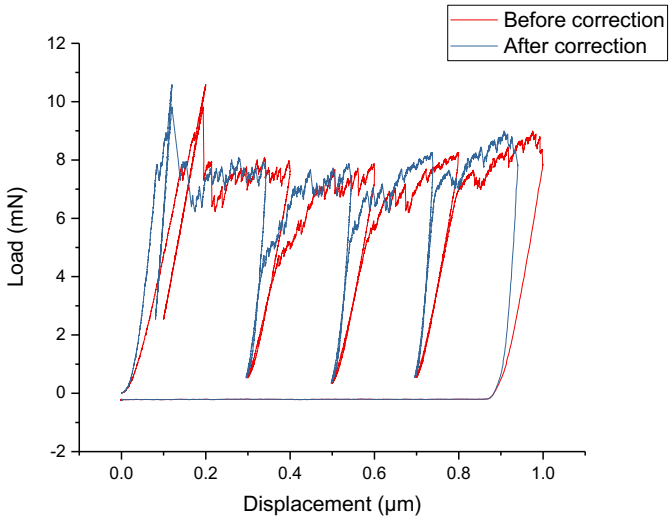


Figure 4.1: Load-displacement graphs of one of the MgO (100) pillars before and after the pillar correction when the stiffness of the surface is taken into account.

The curves of loading-unloading become stiffer after the stiffness of the surface deflection was taken into account. The curves show an elastic loading region where the load increases linearly with increasing displacement for each cycle followed by plastic deformation.

The Young's modulus is calculated with the tangent of the unloading segment for each of the of the cycles and from there, the average value was taken in order to get the elastic modulus of the MgO (100). During loading of the flat punch indenter, both samples initially deforms elastically and then yields and experiences work hardening, while during unloading, the elastic displacement is recovered.

Figure 4.2 demonstrates the representative of stress-strain graph in response to two cylindrical micropillars with five cycles of loading and unloading curve, which is derived from their straightforward microcompression load-displacement results. The pillars experiencing stress increased linearly up to 1 % of strain at the stress level of 1.4 GPa for Pillar 1 and 0.8 GPa for Pillar 2 in the first cycles. The pillars for the rest of the cycles experienced hardening from 0.6 GPa to 1.3 GPa at 2 % strain approximately for each cycle for each pillar.

The value increase in the flow stress over a particular strain of MgO (100) pillars is in agreement with previous research which was around 0.67 GPa and the experiment was conducted on four series of micropillars with consistent values. However, this is contradicted by a similar experiment conducted on the 2 μm diameter MgO pillars which obtained yield stresses at 1.9 GPa[196,197].

Observing the trend of the stress-strain curve for all of the pillars, it was clear that some deformations occurred while the compression took place. Figure 4.2a shows the stress and strain curve of Pillar 1 during microcompression while Figure 4.2b presents the fitting we conducted on the unloading side in order to obtain the Young's modulus. In the first cycle of Pillar 1, it experienced higher stress in the elastic region which is around 1.1 GPa before it

dropped to 0.6 GPa for the second cycle and initially increased up to 1.0 GPa for the subsequent cycles. The reason for this behaviour occurring in the first cycle is because of little contact happening between the pillar and the punch. However, as the test proceeded to the second cycle, it starts to show a steady increment in terms of the stress applied as we believed that the punch had been fully in contact with top part of Pillar 1.

Based on the still images provided from the microcompression video, a small amount of deformation initially started to develop during the third cycle which is proven by the drop in the cycle's load. This will then give way to the deformation to continue as what is presented in the two last cycles until the compression stopped.

Figure 4.2c and Figure 4.2d show a similar graphs and fitting of Pillar 2 during the microcompression test. Unlike Pillar 1, in the first cycle of Pillar 2, the pillar and the punch seem to be in a better contact as there is an increase in stress as the number of cycles increased. In the first cycle, the elastic regions stop at 0.65 GPa and increased to 0.8 GPa in the second cycle before dropping again in the third cycle which is around 0.6 GPa. The last two cycles seem to recover in terms of stress as these cycles linearly increased in stress, which is around 0.7 GPa and 0.8 GPa respectively.

From the graph presented, it can be seen that there is some sudden drop in the third and second cycles which was predicted when deformation took place in Pillar 2. The initial stage of plastic shear starts to develop during the third cycle (which can be seen with a drop in stress). Referring to the video taken during the experiment, this stage was initiated in the middle of the pillar and started forming a group of shear band which is localised at the middle of the pillar wall as the cycles increased. The morphology of these pillars before and post micrcompression will be discussed in the next subchapter.

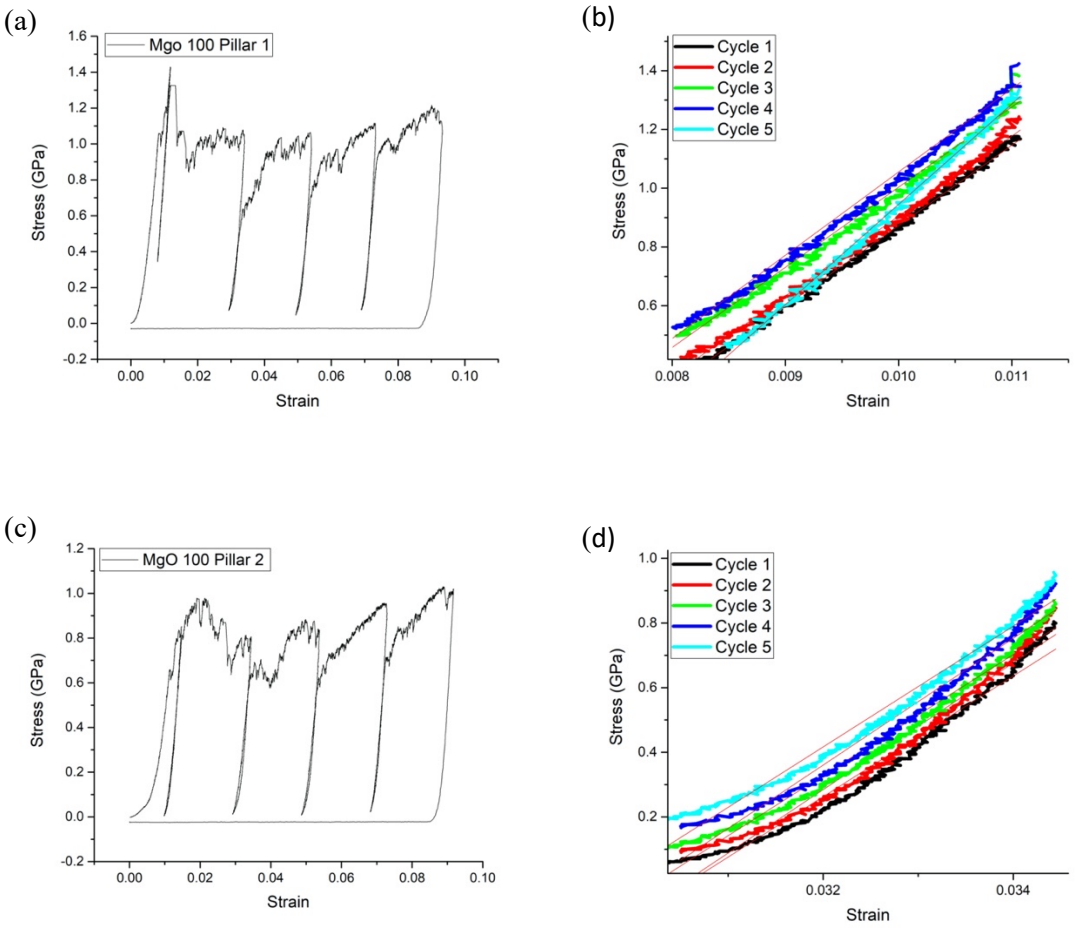


Figure 4.2: The stress-strain curve of two pillars with an average diameter of 3 µm and 9 µm in diameter of height with five cyclic loading and unloading of MgO (100) with just the elastic portion plotted and then the Young's modulus fitted on (a) and (b) for Pillar 1 and (c) and (d) for Pillar 2.

Figure 4.3 presented the Young's modulus of MgO (100) for both pillars. It can be seen that the Pillar 1 starts with a higher modulus compared to Pillar 2 in the first cycles. As the cycles increased, both pillars show an increase in terms of the modulus and starts to have a similar modulus in the third cycles and fourth cycles. However, in the last cycles, Pillar 2 has a lower value than Pillar 1 but still increased in terms of the cycles. Based on the data presented, the Youngs's modulus for Pillar 1 is around 274 ± 1.9 GPa and 265 ± 1.9 GPa for Pillar 2, which give an average of Young's modulus of 270 ± 1.9 GPa.

For all of the samples, the stiffness tends to increase with each cycle, where it could be due to the fact that as the compression test progressed, the contact area is increased. The biggest jump often occurred after the first cycle, which could be the consequence of misalignments between the samples and the punch. As the issue has been aligned, the pillars were then being deformed by the compressed load. Similar behaviour was also reported by Byer and Ramesh[11] on the compression of nanoscale nickel.

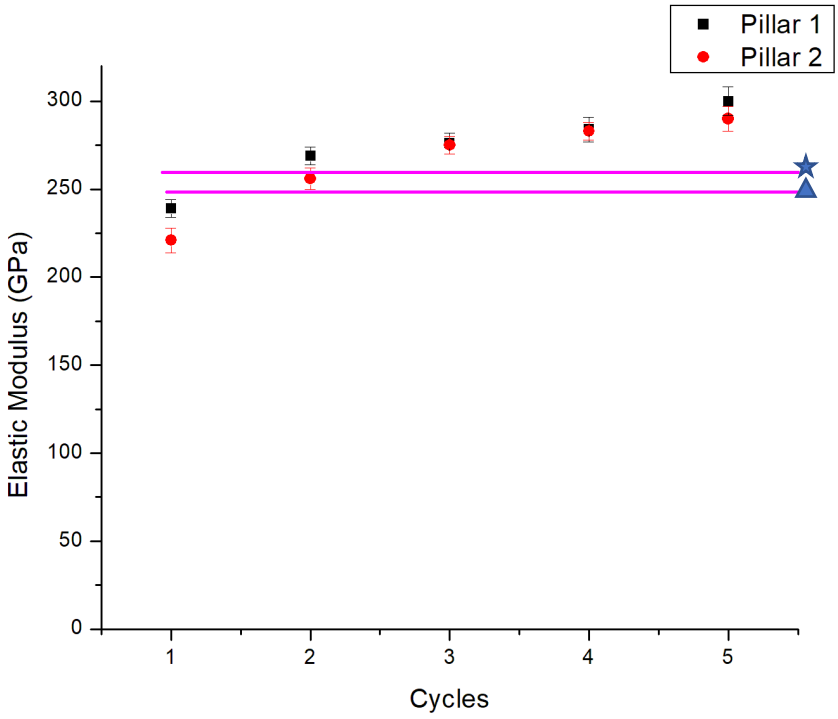


Figure 4.3: Young's modulus (GPa) of Pillar 1 (black square) and Pillar 2 (red circle) of MgO (100) for five cycles during microcompression with two magenta lines that show literature value that was obtained from Chung[19] (indicated in triangle) and Baudson *et al.*[20] (indicated in star) which is between the values after second cycles for both pillars.

The elastic modulus value obtained from this experiment is in agreement with previous data that were carried out with different method such as ultrasonic measurement (251 GPa)[20] and around 248 GPa to 260 GPa by the resonance technique[19,198]. However, it was contradicting with a test carried out by Korte et al.[14] which is around 139 GPa which is considerably lower than those measured by ultrasonic and resonance techniques.

4.3.2 Morphology of MgO (100) micropillars

The micropillars were cyclically loaded at different stress amplitudes until the amplitude decreased to 0, which will correspond to series of deformation into the samples. MgO (100) were investigated by Quanta SEM 650F, which was taken before and after the microcompression took place.

Figure 4.4 presents two micropillars of MgO (100) pre and post compression. These pillars were affected by the FIB fabrication process, which results in some inclusions on the sides of each pillars. The length of both pillars were decreased after microcompression was conducted. From Figure 4.4a and Figure 4.4b, there are visible deformations that consist mostly of shears and thin slip bands traversing all the pillars which were presented with the red arrows for each of the deformations. The still images from the microcompression video also were used in order to understand the behaviour of these micropillars during loading and unloading cycles.

Pillar 1 (Figure 4.4a) has around 0.02 % of strain during compression. Only small changes of height were noticed. The pillar was affected by deformation, which was proven by the presence of some slip bands on the pillar wall. Small thin slip bands were also visible at the top area which was assumed to have been initiated during the third cycle of the experiment, where the deformation starts to take place on the pillar. This might be due to the fact that for the first two cycles, misalignment issues is still needed to be corrected and when there is a better contact between the punch and the pillar surface (assuming in the third cycle), plasticity and deformation such as slip bands starts to initiate on the pillar. This may also be the reason of the higher Young's modulus value compared to the other four cycles because only little deformation took place during this cycle and was influenced under a small strain percentage.

As for the second pillar presented in Figure 4.4b, 0.06 % of strains were observed to have extensions from both sides of the pillar. Slip bands were observed on the wall of this pillar in

the downwards direction, which predicted that some hardening took place during microcompression. Similar to the first pillar, the deformation also took place in the third cycle where shear was nucleated from the middle of the wall, as the load applied to the pillar top, the shear was expanded until it formed a visible group of shear band at the lower part of the pillar wall.

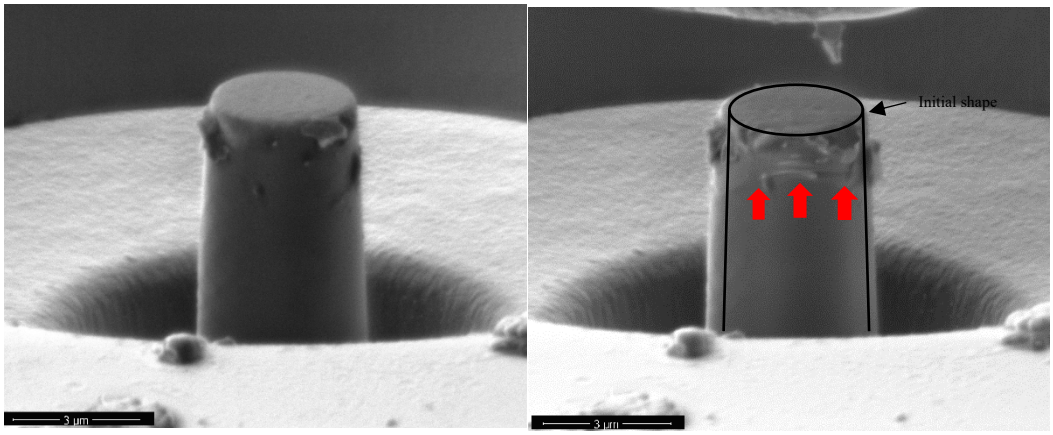
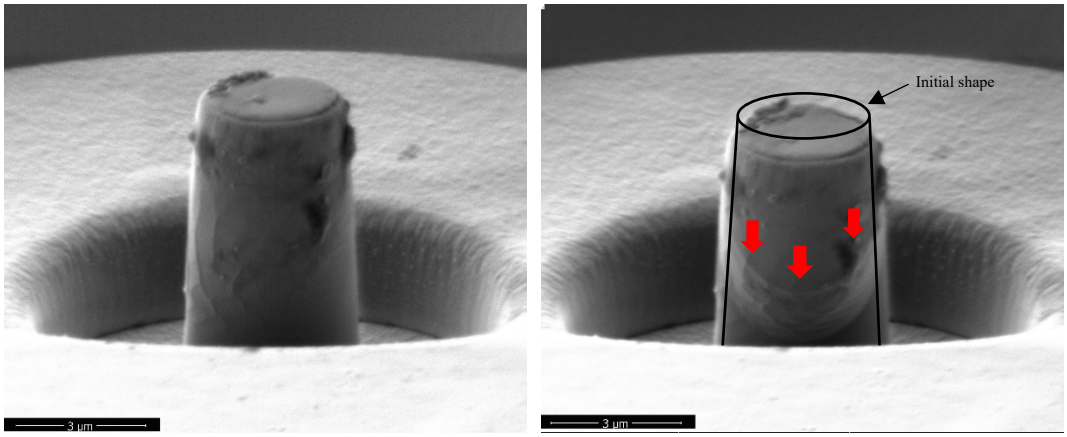
Pillar	Before	After
(a)		
(b)		

Figure 4.4: Micropillar of MgO (100) of before and after compression for (a) Pillar 1 and (b) Pillar 2 with Quanta SE, 650F with the red arrows depicting changes of the behaviour of the pillars.

There was another pillar on which we conducted the microcompression test on it. However, the value of Young's modulus for this pillar had to be eliminated due to the fact that the pillar experienced failure earlier which in the first cycle compared to Pillar 1 and Pillar 2, thus making the value not reliable.

For the sake of understanding the behaviour of MgO (100) under compression, this pillar is included in the morphology. Figure 4.5 presents images of (a) stress-strain curve, (b) third cycle of the curve and images of (c) before and after microcompression on the MgO (100) pillar. It was observed that the pillar experienced a pop in phenomenon drastically in the third cycle. Pop in phenomenon is when the nucleation and propagation of dislocation take place on the pillar. According to Amodeo et al.[13], when the pop in event occurred, the pillar will have a transition from an elastic behaviour to an elasto-plastic regime. Deformation were visible in the other cycle, where there is a sudden drop in the stress-strain curve, which results in the pillars deformation, which leads to easy sliding during microcompression test, thus leading to a decreased in effective area on the pillar, which contributed to a lower elastic modulus.

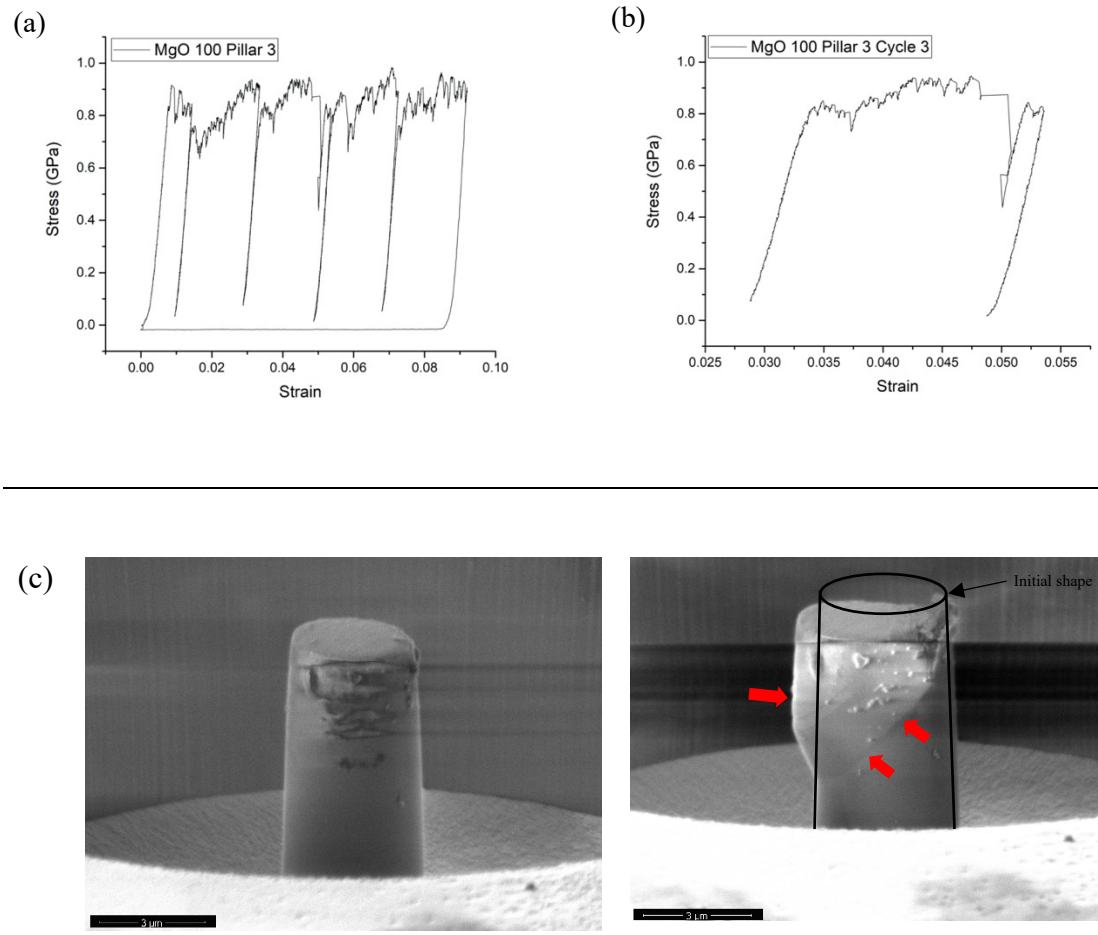


Figure 4.5: Micropillar of MgO (100) which was under microcompression test where (a)stress-strain curve, (b) pop-in phenomenon in the third cycle of the sample and (c) image of before and after microcompression took place.

4.3.3 Microcompression of MgO (110)

Figure 4.4 shows typical load-displacement curves of 5 cycles of microcompression on one of the three pillars of MgO (110). The graphs of load-displacement for the three pillars show a similar trend of loading and unloading MgO (100) pillars, where the cycles tilted to become stiffer as the stiffness of the surface was calculated in order to remove any drift or compliance from the materials.

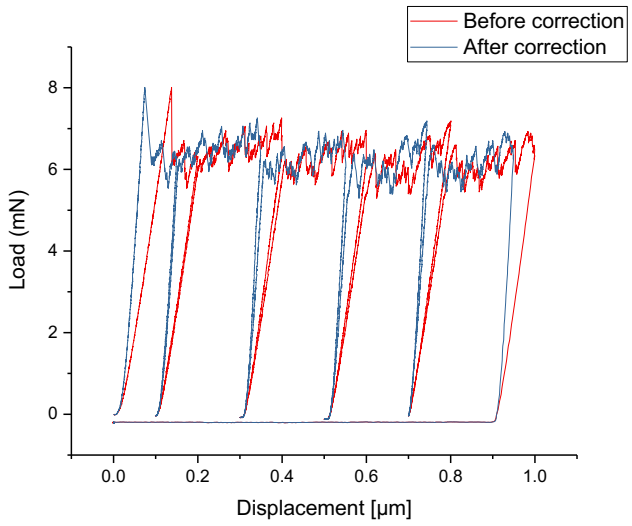


Figure 4.6: Load-displacement graphs of one of the MgO (110) pillars before and after the pillar correction when the stiffness of the surface is taken into account.

The same technique is used to calculate the average elastic modulus which is by calculating the tangent of unloading cycles for each pillar. Based on the Figure 4.3, the compression and pillar axes can be said to be well aligned, as is evident from the linear initial loading segment and how the peak graphs of the cycles are almost consistent with one another.

The stress increased linearly in the loading compressions with a strain rate of around 1 % at the beginning of the cycle and has 2 % of strain in total for the rest of the cycles. The stress obtained in the first cycle was higher from Pillar 1 and Pillar 2 which are 0.9 GPa and 1.0 GPa respectively. For Pillar 2, compression took place at a higher stress for the first cycle and decreased at an almost constant rate for the other remaining cycles.

Figure 4.7 shows (a) stress strain curve and (b) fitting for Young's modulus of MgO (110) Pillar 1. In the first cycle, the stress was higher compared to the other which is around 0.9 GPa and starts to drop in the second cycle (0.78 GPa). Both the third and fourth cycles ended their elastic region with the same value of 0.7 GPa before increasing in the last cycle, which is around 0.8 GPa respectively.

The micropillar of MgO (110) Pillar 1 was expected to have only a small misalignment by referring to the stress-strain curve and the image of the precompression test. Small strain bursts were present in the third and fourth cycles and it does not really affect the behaviour of the pillar under compression. The rest of the curve trend was quite linear until the compression stopped.

Stress strain curve with fittings of MgO (110) for Pillar 2 (Figure 4.7 c and Figure 4.7d) show a high peak in the initial cycle which might be due to the punch already touching the pillar when the experiment started. This very close contact between punch and pillar will lead to overestimation of stiffness. Almost similar behaviour with Pillar 1 was shown in Pillar 2 where, the stress increased up to 1,.0 GPa in the first cycles and dropped to 0.6 GPa in the next cycles. The three last cycles have 0.65 GPa (third cycle), 0.7 GPa (fourth cycle) and 0.76 GPa in the last cycle.

One of the reasons of this behaviour is that, when the punch is already in position (misalignment has been removed in the initial cycle), deformation of the pillar starts to play its role. Some pop in displacements were shown in the second and fourth cycles. As it reached the fifth cycle, the trend starts to become quite linear again

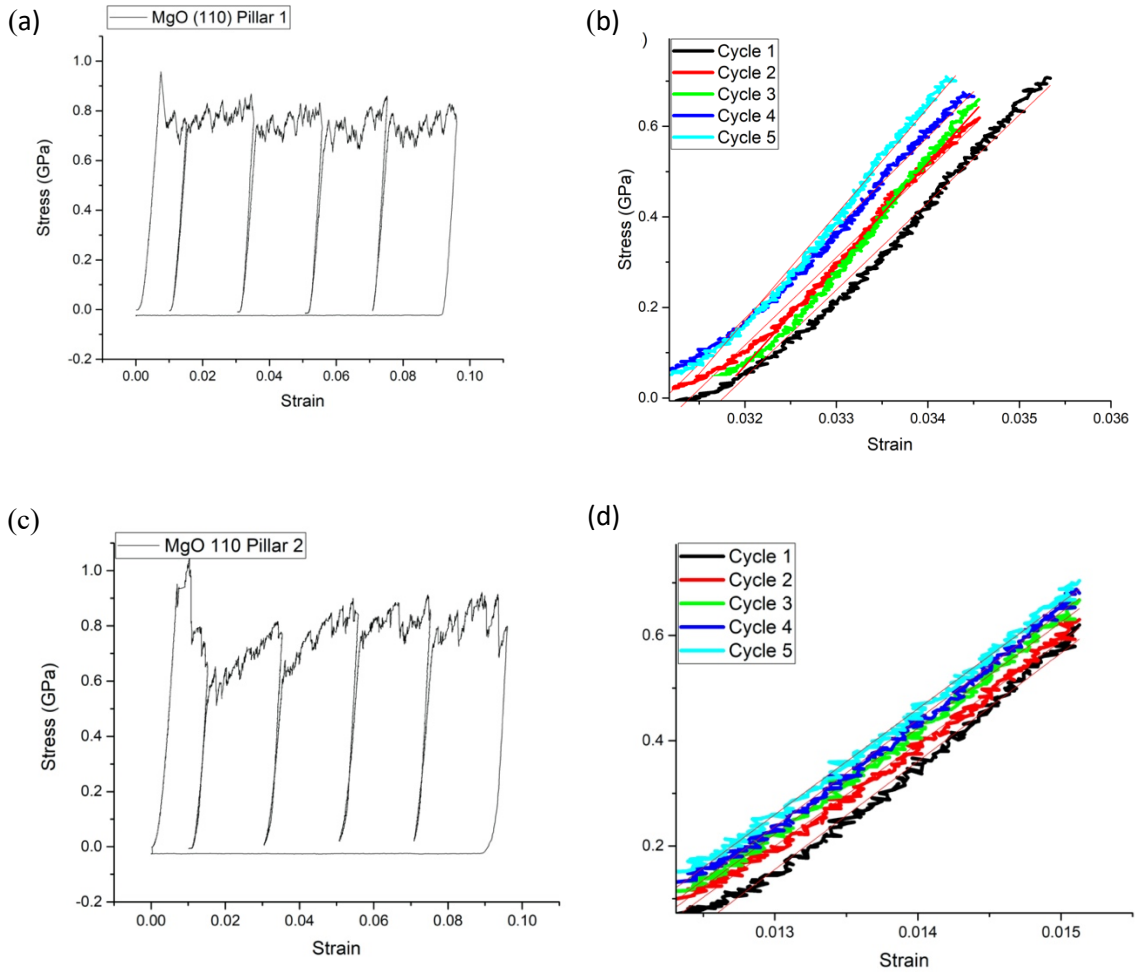


Figure 4.7: The stress-strain curve of two pillars with an average diameter of 3 µm and 9 µm in diameter of height with five cyclic loading and unloading of MgO (110) with just the elastic portion plotted and then the Young's modulus fitted on (a) and (b) for Pillar 1 and (c) and (d) for Pillar 2.

Figure 4.8 shows Young's modulus for both Pillar 1 and Pillar 2 of MgO (110) with five cyclic loads. Pillar 2 starts with a lower Young's modulus compared to Pillar 1. However, when it starts to be compressed in the second and third cycles, the value of Young's modulus for both pillars became almost similar. This could be the fact that the misalignment has been corrected and both pillars were in better contact with the flat punch indenter. However, in the final cycles, Pillar 1 shows an increased in value which is around 20 GPa more compared to Pillar 2. For MgO (110), Pillar 1 has an average of 275 ± 1.5 GPa and 269 ± 1.5 GPa for Pillar 2, which

makes the average Young's modulus for MgO (110) around 272 ± 1.5 GPa by microcompression.

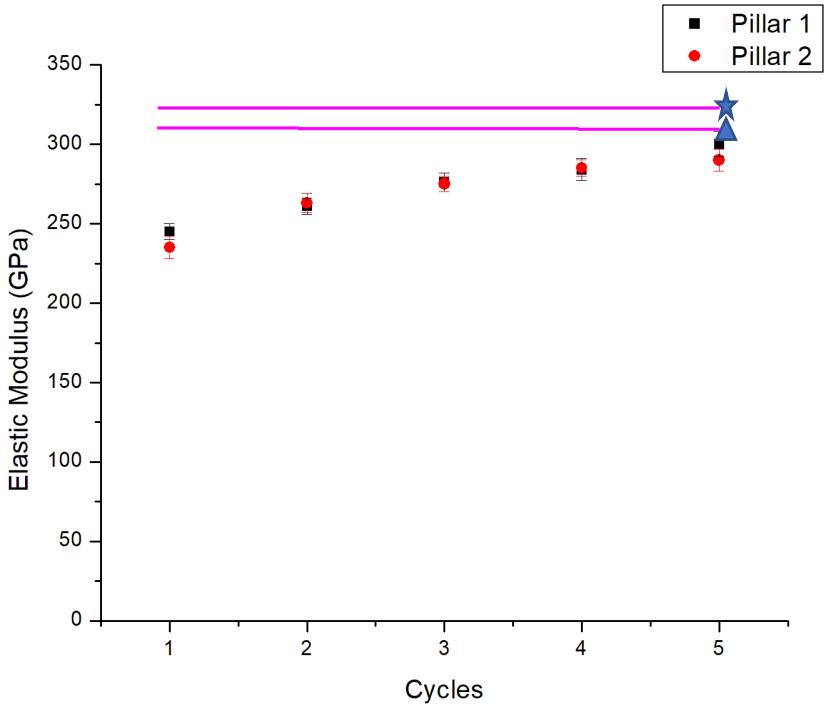


Figure 4.8: Young's modulus (GPa) of Pillar 1 (black square) and Pillar 2 (red circle) of MgO (100) for five cycles during microcompression with two magenta lines that show literature value that was obtained from Isaak[21] (indicated in triangle) and Chang *et al.*[22] (indicated in star) which is between the values after second cycles for both pillars.

The elastic modulus of MgO (110) is only higher by 2 GPa compared to MgO (100), which deviates significantly from the actual elastic modulus of bulk samples measured by other methods such as nanoindentation, resonance and ultrasonic measurement which is 316 GPa and 323 GPa[21,22,199].

Another reason of MgO (110) Young's modulus being lower than expected is due to the calibrated centre of the compression punch, which was moved in transverse direction in a successive compression mode, away from the pillar position, which results in stiffness

reduction in the unloading section and allowing initiation in plastic deformation. The initial deformation gave a low stiffness, suggesting that the curve was dominated by plastic realignment in order to give a more uniaxial stress state, which is consistent with imperfect contact due to punch misalignment and/or inclination of the punch surface towards the edge of the pillars [21,22,42].

As similar trend was observed in tungsten carbide micropillar [200] where the stress-strain curve showed strain bursts on each cycle, which is in response to their mechanical behaviour. MgO (110) is stiffer than MgO (100) and theoretically. Therefore, from seeing this situation this might explain why the value elastic modulus is higher compared to MgO (100). However, this value is only increased by 2 GPa which does not show a significant increase in the elastic modulus, where it could be assumed that this occurs due to increased strain in the pillars, the stiffness decreases during the microcompression test.

Furthermore, the change in Young's modulus during each cycle is presumed to have something to do with the change of geometry due to deformation. A huge jump between the first cycle and the second cycle for Pillar 1 is due to the elastic loading in the combination with "early plasticity" effects. A similar trend was observed in gold micropillars[161], where this early plasticity was affected by the surface roughness and the position of the punch on the top of the column was not in a perfect condition. The elastic modulus increased up to the fourth cycle before dropping in the final stage. This occurred due to the pillars having started to be fully deformed and eventually failing.

4.3.4 Morphology of MgO (110) micropillars

Figure 4.9 shows the morphology before and after microcompression test was conducted on the three pillars of MgO (110). All of these images were taken from a still video image that was captured during the microcompression test. It is visible that the length of the pillar

decreases over displacement for all the pillars and that these pillars were not in a flat surface at the top of the pillar, which might result in the deformation occurring on them. The deformation on these samples are much more interesting compared to MgO (100) because of their strength which is supposed to be higher.

The red arrows presented in the pictures show the deformation on the pillars. Deformation on Pillar 1 which is seen in Figure 4.9a experienced crack formation on the surface of the pillar, which some shear has been introduced on the middle wall of the pillar. The pillar had undergone 0.2 % of strain during the compression. Although some mechanical behaviour occurred on the pillar, the pillar was able to withstand the stress and therefore no obvious changes of the cylindrical shape happened.

Pillar 2 (4.9b) showed a slip band on the side wall of the cylinder and showed slip bands on the right side of the cylindrical wall. This can be observed by looking at a few glide events in the stress-strain curve which is the dislocation avalanches and also underwent 0.1 % strain. These dislocations avalanches are also due to larger strain bursts observed during the inhomogeneous loading in the microcompression in other metals[201,202]. The strain bursts were initiated by the plastic instability where the motion of a few individuals dislocations sets off an avalanche dislocation nucleation and glide events[203]. The stress applied around 0.8 GPa to 1.0 GPa introduced this kind of deformation on the pillars.

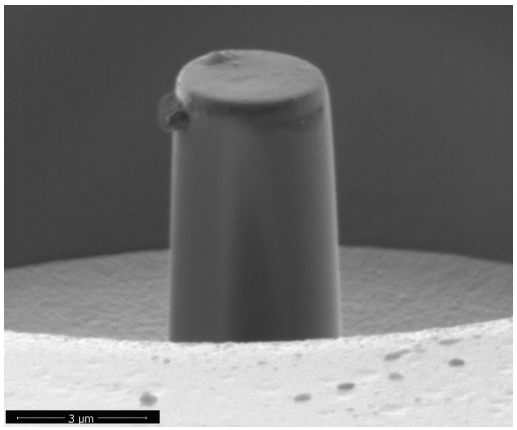
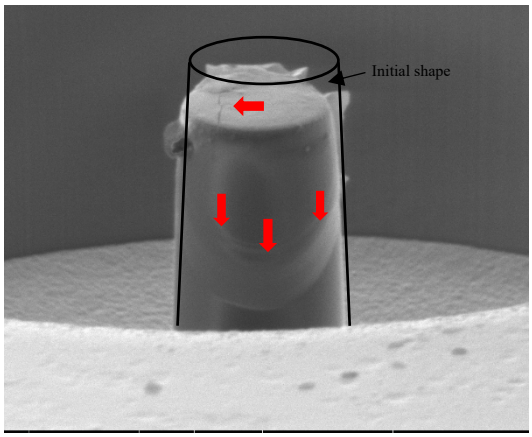
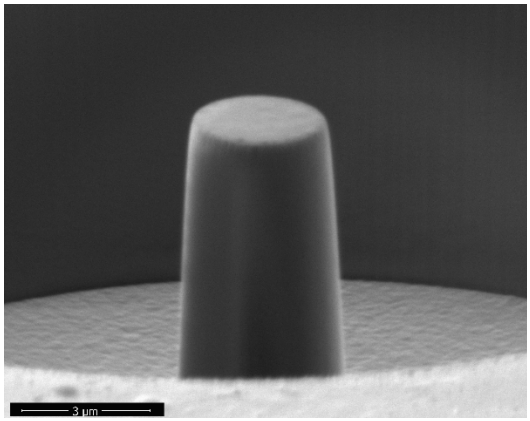
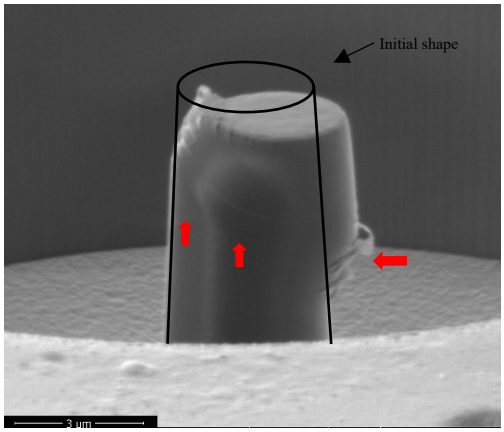
Pillar	Before	After
(a)		
(b)		

Figure 4.9: Micropillar of MgO (110) which was under microcompression test where (a)stress-strain curve, (b) pop-in phenomenon in the third cycle of the sample and (c) image of before and after microcompression took place.

Similar to MgO (100), there was one pillar that was not included in the Young's modulus calculation. The pillar experienced failure earlier than expected, which gave the value for each cycle lower by half than the expected value. The value obtained from this particular pillar is 163 GPa which is the lowest compared to other micropillars. However, the post-microcompression behaviour of the pillar was rather interesting (Figure 4.10). This pillar showed surface splitting with 1.0 % of strain.

This pillar shows a linear trend in the stress-strain curve (Figure 4.10a). However, the initial cycle showed a higher start in stress compared to other cycles which was may be contributed to misalignment between the pillar and the indenter. Similar behaviour in a study of nickel microcompression conducted by Frick *et al.*[161]. Due to this misalignment, the pillar has already been affected by deformation, which was presented by strain bursts and dislocation pop in the second and third cycles. The dislocation avalanches were happening in the last cycle (Figure 4.10b). These cycles show an increment of stress as the percentage of strain increased, despite of the bad contact position of the pillar and indenter.

Figure 4.10c shows a top surface splitting with 1.0% of strain. The same behaviour was observed on the MgO (100) micropillar with a 2 μm diameter [204]. This type of fracture mode usually will cause the shape of the cylinder to become more oval in cross section due to a slip on the intercepting of slip planes. The friction between the pillar and the punch leads to fracture due to the constraint on the top surface of the pillar. According to Howie *et al.* [205], tensile strain will be imposed on the constrained surface as the whole pillar deforms, which will then relax when the punch is removed, giving rise to the observed cracking and they also predicted that the top surface cracking will occur during the unloading of the punch.

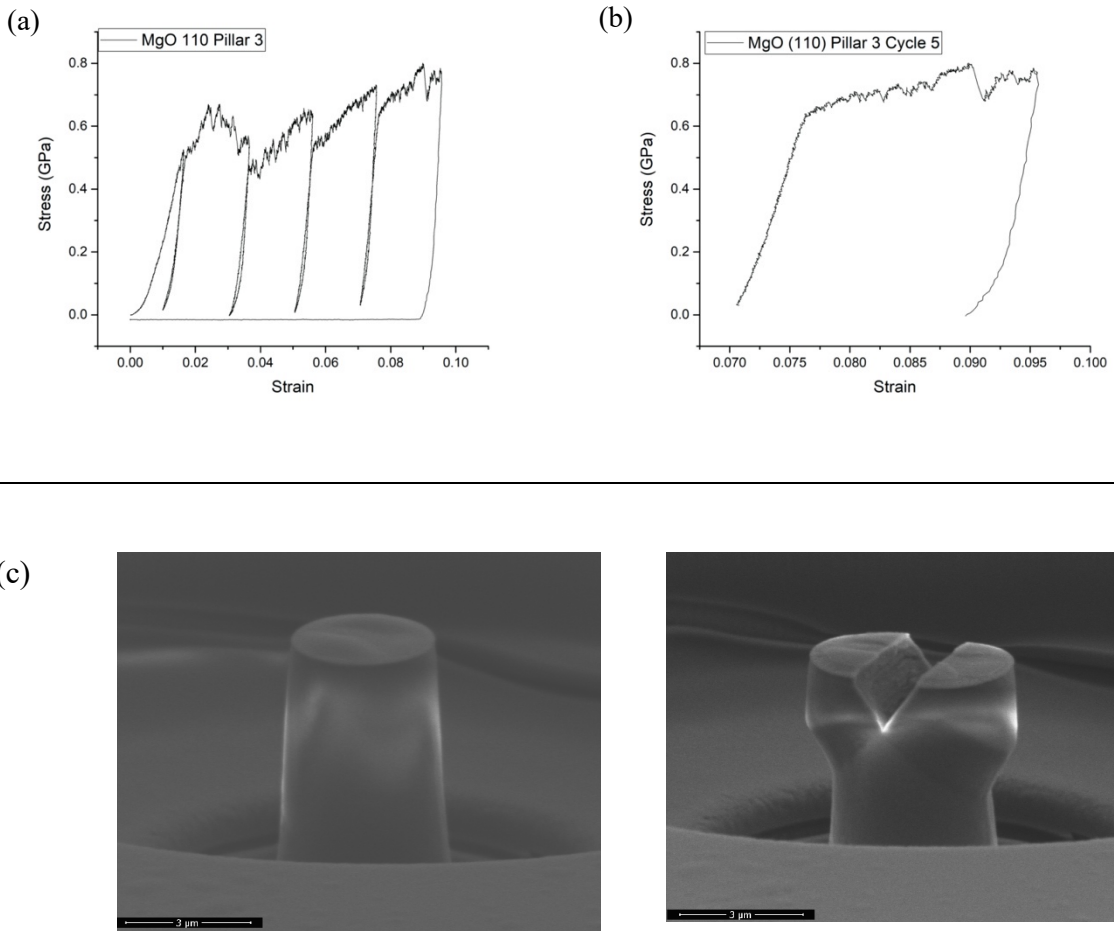


Figure 4.10: Micropillar of MgO (110) which was under microcompression test where (a) stress-strain curve, (b) dislocation avalanches in the fifth cycle of the sample and (c) image of before and after microcompression took place.

4.4 Discussion

Referring to the video taken during the experiment, it was found that the elastic modulus of MgO (100) and MgO (110) gave value which is around 274 ± 1.9 GPa and 265 ± 1.9 GPa for both pillars in MgO (100), which is in agreement with the literature review (248 GPa to 260 GPa) and 275 ± 1.5 GPa and 269± 1.5 GPa in Pillar 1 and Pillar 2 of MgO (110). During microcompression test, both pillars from two different orientations were seen to be in good contact between the flat punch indenter and the top surface which corresponds to better measured elastic modulus.

The position and contact between the flat punch indenter on top of the pillar surface plays a crucial state when performing microcompression on micropillars. Early deformation might be introduced on the sample if the punch was too in contact with the pillars that leads to early failure of the sample. Meanwhile, if the punch is out of contact with the pillars, the stiffness obtained from the first few cycles will be lower, which might affect the value of Young's modulus. Therefore, it is really important to position the punch at the right position in order to avoid these issues especially misalignments between puncher and the sample.

Theoretically, the Young's modulus of MgO (110) is higher than MgO (100). The results obtained from this present work show that the microcompression test gave an average value of elastic modulus for MgO (110) around 272 ± 1.5 GPa. Although MgO (110) elastic modulus is lower compared to technique like nanoindentation, which is around 315 GPa for MgO (100) and 321 GPa for MgO (110), we are able to avoid occurring issues during nanoindentation test on samples such as overestimation of hardness and modulus values due to small indentation depth and also the sink in or pile up effect which is expected with the nanoindentation test.

Furthermore, orientation of MgO (100) gives a higher value when compared to techniques like resonance and ultrasonic measurement, which is around 248 GPa to 260 GPa. MgO (100) pillars also seem to be in a stable state compared to MgO (110) based on this experiment. This can be proven by the load-displacement curve having higher displacement on MgO (100) compared to MgO (110). This action also indicates the reduction in misalignment between the pillar and the punch and it gave only a small effect in the stiffness in response to their unloading curve.

Based on the stress strain curve, MgO (100) was able to withstand the applied stress from 1.0 GPa to 1.6 GPa per cycle; whereas for MgO (110) the highest applied stress given was only 1.0 GPa. However, changes started to arise in pillars from MgO (110) in the third cycles where

the elastic modulus values started to be stable for both of the pillars. This might indicate that the top surface is becoming flatter which leads to stable value of Young's modulus.

Micropillar tapering also may have contributed to underestimation of elastic modulus during this experiment. It is almost impossible to get a straight circular pillar by using the FIB technique; therefore, these pillars were tapered when the test was conducted. This is because, tapered sample leads to uneven distribution of stress during microcompression test due to the cross section of the area increasing from the top to the bottom of the pillar. This will then leads to barrelling of the sample that is established due to the friction between the pillar top and the diamond tip being relatively high, while the other end was fixed and gave rise to deformation[132,206].

Consequently, the morphologies from both MgO show that, unlike MgO (110), after yield point, MgO (100) pillars do not experience catastrophic deformation such as strain burst. However, it is predicted that if a significant increase of applied load is given to pillars of MgO (100), further deformation would have been seen and results in final failure stress. Furthermore, the behaviour during deformation of micropillars on different orientations is attributed to dislocation mobility which affected the elastic modulus value. The discrepancy of the data for MgO (110) was also seen on the microcompression of single crystal LiF which it was suggested that the extra compliance established during the first stages of the cycle is attributed to the lower measured stiffness[133,207].

4.5 Summary

The microcompression of two different orientation of MgO (100) and (110) were conducted with the aspect ratio of diameter to length of 3:1. The measured elastic modulus of MgO (100) and MgO (110) are 270 ± 1.9 GPa and 272 ± 1.5 GPa. Microcompression on the MgO (100) pillars are in a good agreement with the value of elastic modulus with the previous technique such as ultrasound measurements. MgO (110) has higher elastic modulus compared to Korte *et al.*[208] but is still lower than studies conducted by nanoindentation technique.

The choice of taking an average diameter for the calculation of the stresses, rather than the top diameter used to calculate the Young's modulus reduces the discrepancy, but other factors such as misalignment and material deforming plastically in different parts of pillars may also play a role. The results obtained are the most accurate measured by micropillar probably because of the small scale mechanic techniques, however, this is not accurate enough to be able to discern between different orientations.

Chapter 5

Microcompression study of Fe_xN thin films on sapphire

5.1 Introduction

In this study, we describe the microcompression of Fe_xN thin films that were grown on sapphire (0001). By conducting this study, we hope to identify the films potential interest as structural materials.

Fe_xN has been grown as an epitaxy layer using the EBE technique, where the parent material (Fe) was sputtered on the sapphire substrate in the chamber with specific parameters under the influence of Nitrogen monoatoms. The thin films thickness was about 600 nm which was supported by the TEM images presented in Chapter 3. Similar to the preliminary study, micropillars were fabricated using FIB before we proceeded to the microcompression test. This microcompression method is used to extract the relationship between compressions of thin films from the substrate so that the elastic modulus of the thin films may be estimated.

Only few references are available on thin film microcompression and this is one of the reasons that motivates this study, which aims to understand the behaviour and morphology of thin films with a certain thickness after applying microcompression. The results and discussions of both thin films and substrates are then presented and we are able to establish the relationship between the elastic modulus of the film under the influence of compressions.

5.2 Micropillar fabrications and microcompression experiment

Sapphire (0001) (which is also known as the c plane) was used as a substrate for thin films. It was obtained directly from Agar scientific and were cut to 1 mm x 1 mm and placed into the FIB chamber to proceed with pillar fabrications. The pillars were milled by using the Nanobuilder script which is similar to MgO pillars. However, a few alterations have been made in order to achieve the 1:3 aspect ratio of diameter to length for example by prolonging the milling time and using a lower beam current. The average diameter of all the pillars is taken by measuring the top, middle and bottom parts of the pillar.

The sapphire micropillars were measured in this project, where two of the pillars have an average diameter of 3 ± 0.5 μm and around 10.25 ± 0.3μm in height. This is one of the obstacles of fabricating micropillars on the sapphire, as the sapphire is well-known for its hardness and strength. The time taken to fabricate these pillars was also longer compared to other softer samples used such as on silicon or MgO substrates. This also leads to the variation of diameter to height ratio due to the instability of the milling process corresponding to the area that the pillar is fabricated on, such as had happened with the last pillar.

Unlike the sapphire pillars, the fabrication of Fe_xN thin films on sapphire for the rough machining step of the first milling used a lower current around 6.9 nA rather than 21 nA which is commonly used in the first procedure. This rough machining step uses a lower current because we are trying to avoid excessive beam damage from ion milling. Due to the thickness of the thin films which is around 600 nm, pillar fabrication was carried out carefully because the thin films will be sputtered away by the ion from FIB and could potentially result in pillars that only contain sapphire.

Figure 5.1 shows the pillar of Fe_xN thin film with sapphire. The pillar consists of thin film (Fe_xN) at the top and the rest of the pillar is sapphire. Unlike sapphire, the average diameter and height of the Fe_xN thin film micropillars were between 2.77 ± 0.3 µm to 2.89 ± 0.5 µm and the height were around 7.22 ± 0.2 µm to 8.31 ± 0.5 µm as presented in Figure 5.2. Each of the pillars was given five cycles of loading and unloading with the rate of 5 nm s^{-1}.

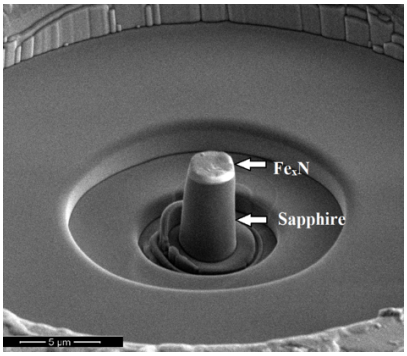


Figure 5.1: Fe_xN thin films with sapphire as the substrate. As presented, the sapphire is part of the pillar and also acted as a base for the thin film sample.

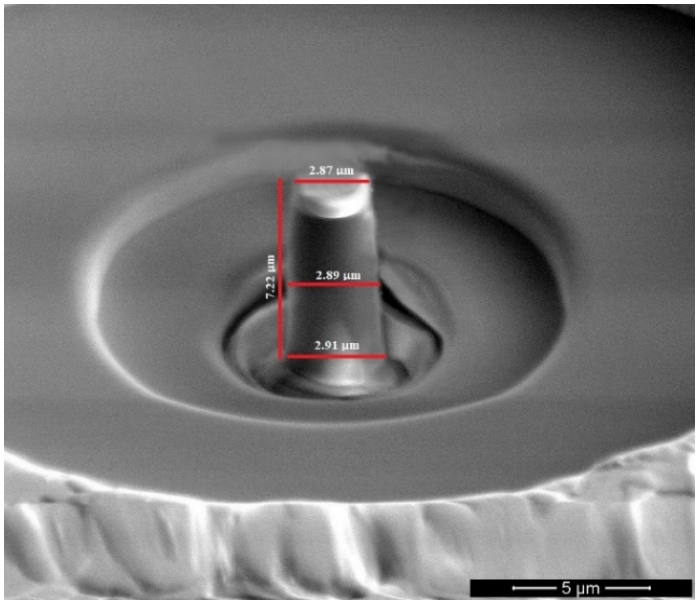


Figure 5.2: Micropillar of Fe_xN thin films on sapphire as substrate where Pillar 1 shows the average diameter and height.

5.3 Results

5.3.1 Microcompression of Sapphire (0001)

Figure 5.3 shows the load displacement of one of the three sapphire micropillars. The red curve indicates the load-displacement curve that was extracted directly from the experiment while the blue line was constructed after we have corrected the compliance of the system, the substrate and the load frame where it can be seen that the curves become 30% stiffer compared to as received stress-strain curve (red line). During the compression test, the load-displacement data obtained was influenced not only by the pillar deformation, but also by the whole compression sample because the pillar was pressed into the underlying material [136].

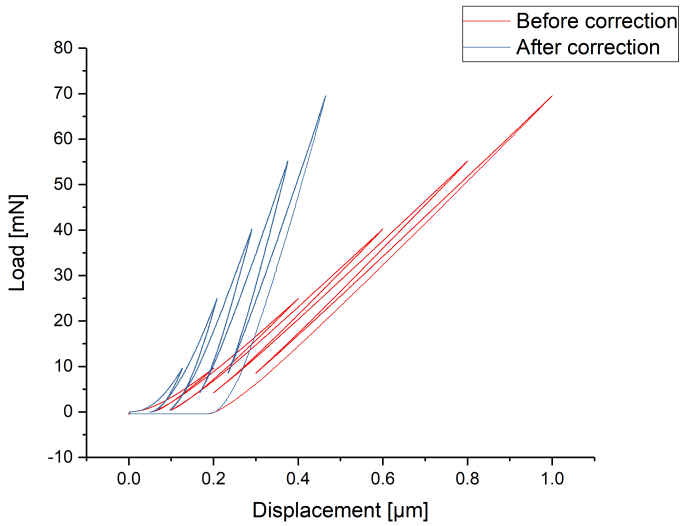


Figure 5.3: Load-displacement graphs of one of the sapphire (0001) pillars before and after the pillar correction was applied on them.

Micropillar compression tests were performed on the C orientation (0001) of sapphire and the atypical stress-strain curves are shown in Figure 5.4. The stress calculated corresponds to the uniaxial stress calculated using the top pillar diameter as the stress is higher at this point due to the taper in the pillars [209,210].

The stress-strain curve of Pillar 1 is reported in Figure 5.4a where the initial cycle starts at a lower applied stress compared to Pillar 3 with 1.0 GPa for 0.02 % strain with maximum stress of 7.5 GPa for the last cycle. Strain percentage was increased with each subsequent cycle, which resulted in an increase of stress. Pillar 2 (Figure 5.4b) starts at the applied stress of 2.5 GPa. The difference of applied stress in the first cycle indicates the contact between the indenter and the punch. By looking at the still image captured in the microcompression video (Figure 5.6 and Figure 5.7) it appears that Pillar 2 was in perfect contact between the pillar top and the bottom of the indenter which was not the case in Pillar 1.

It is also noticeable that unlike the MgO stress-strain curves, the sapphire pillars experience very little plastic deformation during the experiment. There was only an elastic curve to peak stress and the stress starts to drop before proceeding to the next cycle. This could also be attributed to the increase in depth with each cycle that exhibits plasticity or some deformation on the surface of the pillar. The linear increases between cycles in the curves indicate that as the misalignment between the punch and the pillar was corrected, the pillars start to deform in uniaxial manner until the experiments stopped[211].

These graphs also demonstrate that the unloading and reloading curves of two sapphire pillars are nearly the same. The value of elastic modulus was calculated from the unloading slope for each cycle, where the unloading curve is assumed to be linear as the contact area between the punch and the pillar remain in contact. The Young's modulus of both pillars are presented in Figure 5.5.

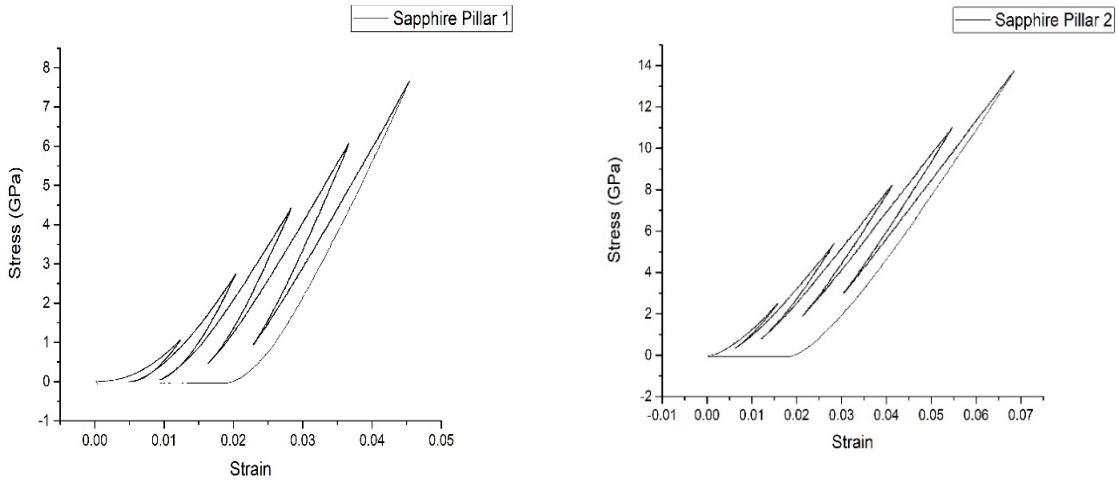


Figure 5.4: The stress-strain curves of three pillars with a different diameter of height with five cyclic loading and unloading cycles for (a) Pillar 1 and (b) Pillar 2.

Figure 5.5 presents the Young's modulus of Pillar 1 and Pillar 2 of sapphire after microcompression tests. By looking at the trend, Pillar 2 starts with a higher modulus which is around 265 GPa and 339 GPa compared to Pillar 1 (188 GPa and 262 GPa) for the first two cyclic loads. This inconsistency of the elastic modulus value may be due to the misalignment and poor surface contact between the flat punch and indenter. However, as the cycles increased, the elastic modulus for Pillar 1 shows a higher increment, which is around 19 % compared to Pillar 2. It is also noticeable that after the fourth cycle, both pillars drop in the Young's modulus by 15.5 % for Pillar 1 and 4.45 % for Pillar 2, which give the average elastic modulus for Pillar 1 as 317 ± 0.24 GPa and 320 ± 0.24 GPa for Pillar 2.

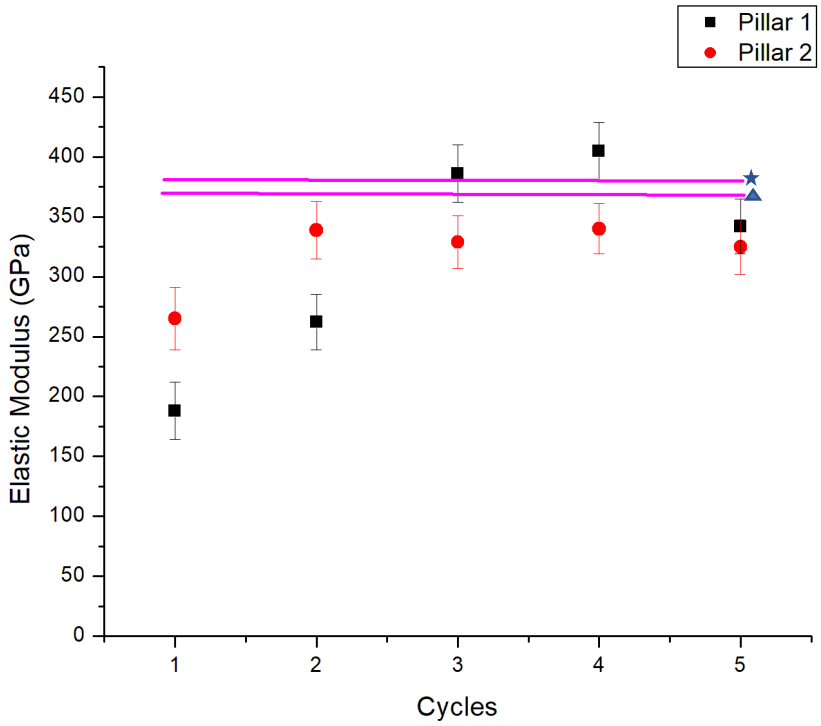


Figure 5.5: Young's modulus (GPa) of Pillar 1 (black square) and Pillar 2 (red circle) of Sapphire (0001) for five cycles during microcompression, where the magenta lines indicate the sapphire literature data that was obtained from Saha and Nix[23] (indicated in star) and Zoubolis *et al.*[24] (indicated in triangle) which is between the values of third and fourth cycles for both pillars.

The elastic modulus of sapphire obtained by other methods such as nanoindentation and Brillouin scattering reported the value to be 370 GPa and 386 GPa[23,212]. The average data of these five cycles showed a lower elastic modulus compared to the reference value. However, as the cycle increased to the third and fourth cyclic load, the average of elastic modulus value of these two cycles is very close to the reference where for Pillar 1, the elastic modulus in the third and fourth cycle are higher than the reference data, which will be explained in the discussion section. Furthermore, no value on sapphire was reported on the microcompression method to date. This gives an idea on improving and revising the techniques and methods in order to get a better outlook of elastic modulus performed on thin films.

5.3.2 Morphology of Sapphire (0001) micropillars

Microcompression testings were performed in situ in a scanning electron microscope, which provided high spatial and temporal resolution imaging of the loading. This proved beneficial, not only aligning the sample and loading geometry but also providing a direct observation of the sample under load during the test.

The pre and post compression test of both Pillar 1 and Pillar 2 are presented in Figure 5.6, where these two pillars showed similar SEM images. Therefore, it can be assumed that the elastic modulus data points are more reliable when the pillars undergo compression during the third and fourth cycles. The graph provided in Figure 5.5 is raw data but it can be seen from the SEM images that there was deformation on the top of the pillar which makes the top surface flatter.

The presence of a crack on Pillar 2 could be due to the substrate effect of the thin films' behaviour where there is the release of elastic energy in the regions of the film still bonded to the substrate. Thus, the more compliant the substrate is compared to the film, the more energy is released from the film[141,213]. This energy release will initiate the formation of cracks on the interface between a stiff film and a high strength substrate, which reflects on the lower Young's modulus of the thin films.

The morphology of the Sapphire (0001) of Pillar 1 is presented in Figure 5.7. Each of the red circles depicting the image was taken at that point. The first cycle observation is not provided as the first load is usually focused on the alignment of the sample with the flat punch. In the second and third cycles, which are shown at point (a) and point (b) (Figure 5.7a and Figure 5.7b), there were no apparent changes on the pillar. Point (c) in Figure 5.7c also exhibited similar behaviour during the loading stage. However, in the last cycle (Figure 5.7d), the pillar was believed to be in a relaxed state at point (d) where the indenter was unloaded from the

sample surface. This post compression image shows a small tilt at the top of the pillar. It was also predicted that if the cycles were added to the experiment, most probably some deformation will be visible on the pillar.

Pillar 2, which is presented in Figure 5.8 shows a similar behaviour to Pillar 1. However, at points (a) and (b), deformation occurred at the top of the pillar side which introduced a little bending on its surface, which is presented in Figure 5.8a and Figure 5.8b. In addition, as the cyclic load progressed at point (c), the deformation took place at a smaller area than Pillar 1 and we can see the deformation propagation from Figure 5.8b starting to elongate to the bottom side of the pillar which is presented in Figure 5.8c. As the pillar was in the unloading state in point (d) and shown in Figure 5.8d no other apparent changes occurred on the pillar.

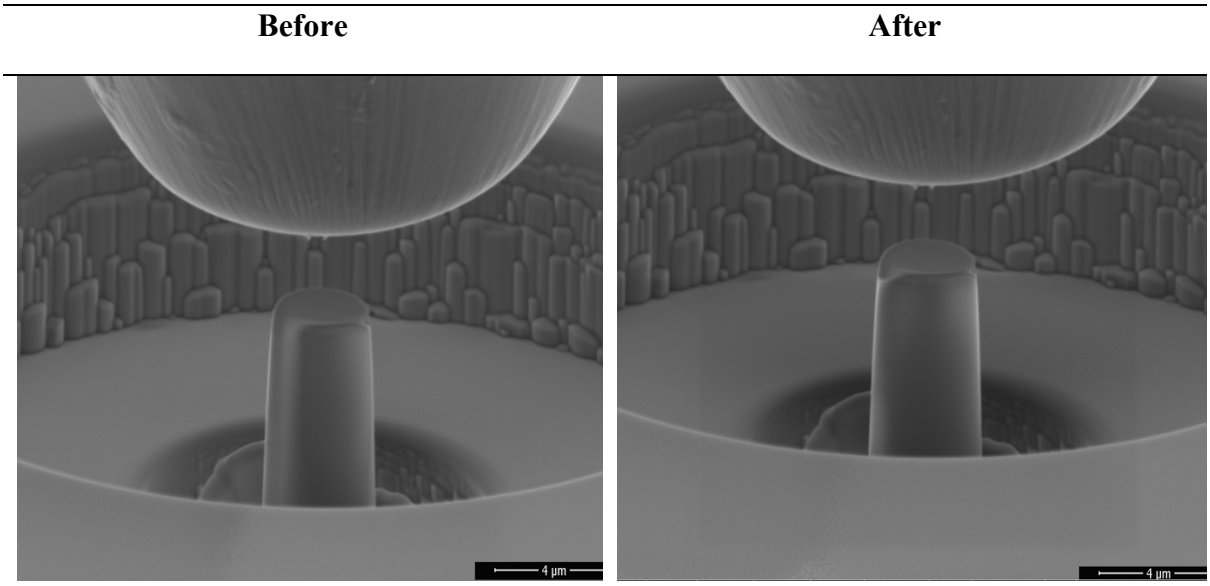


Figure 5.6: Before and after for both Pillar 1 and Pillar 2 of Sapphire (0001) that shows similar SEM images of pre and post microcompression test.

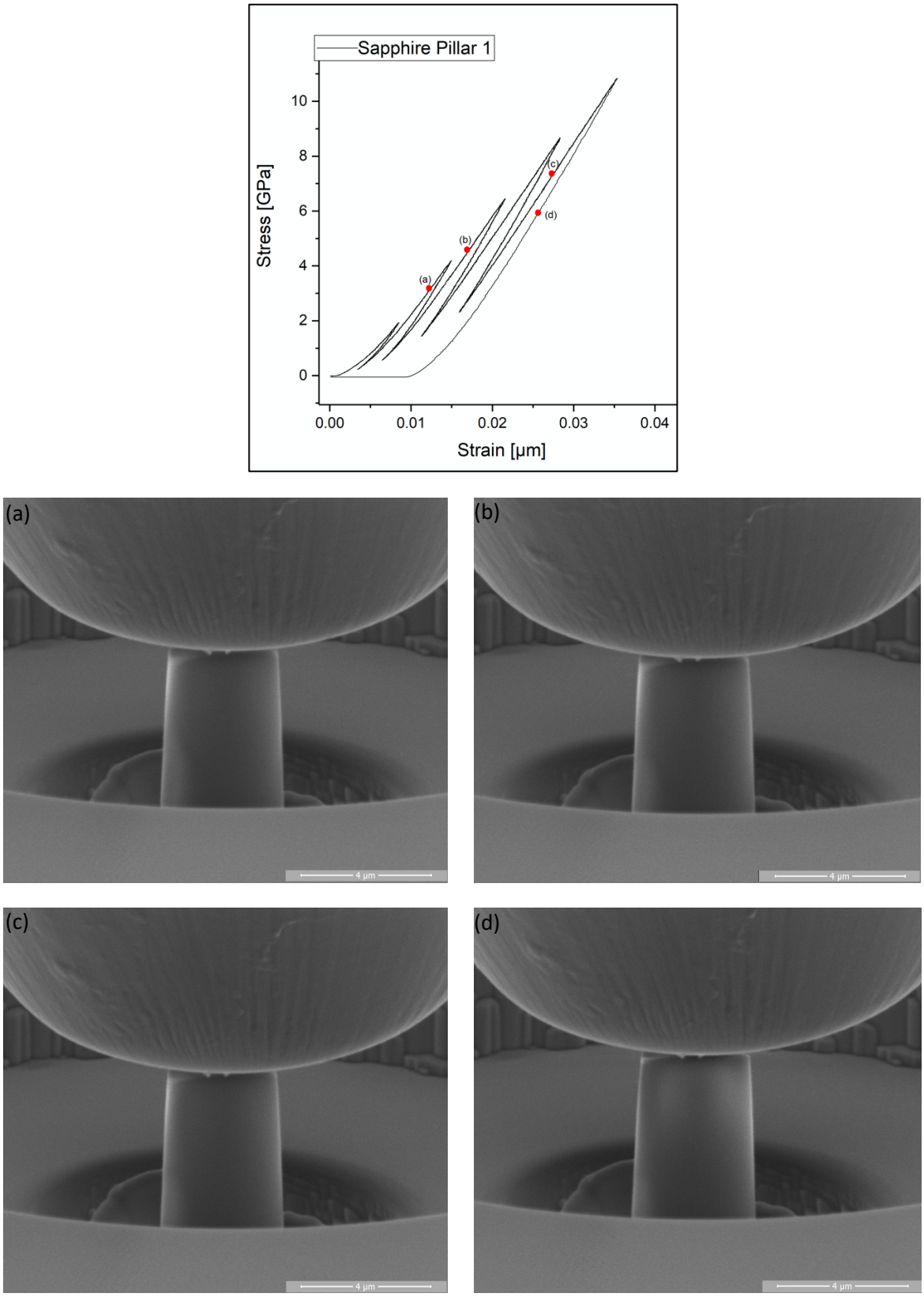
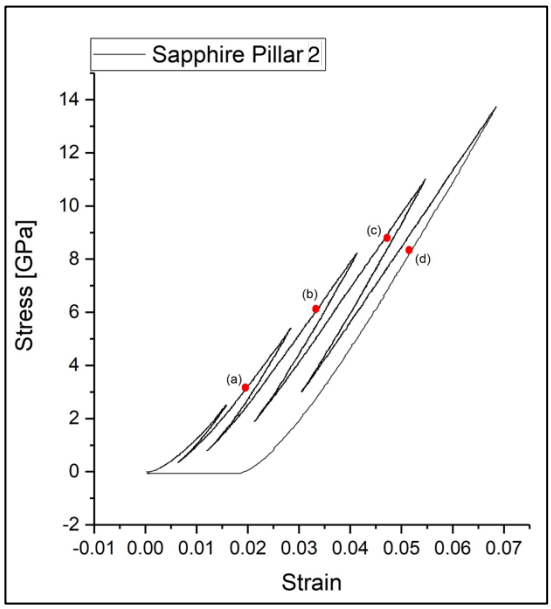
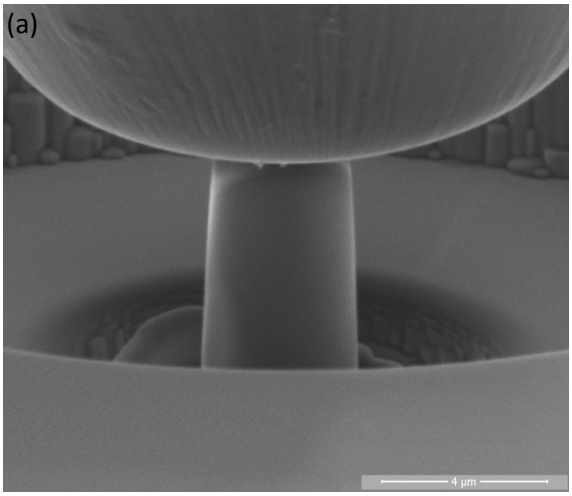
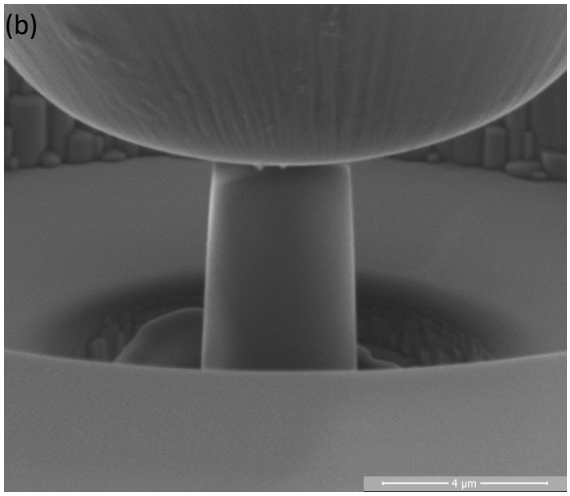
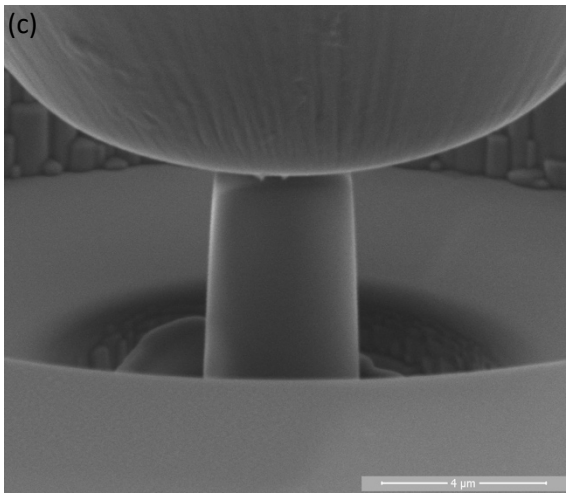


Figure 5.7: Pillar 1 of Sapphire (0001) denotes the morphology of the pillar during point (a), (b), (c) and (d) of microcompression test.









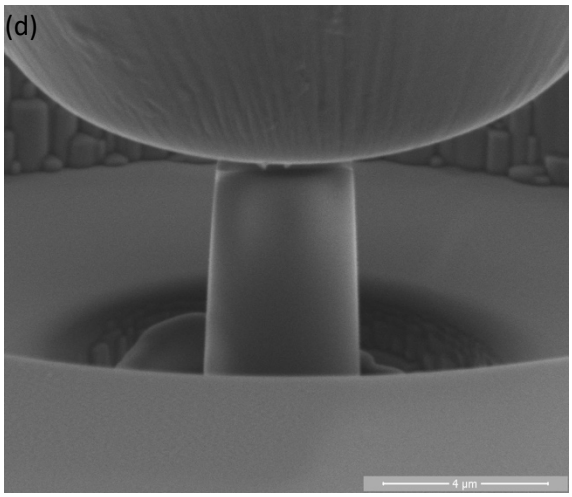


Figure 5.8: Pillar 2 of Sapphire (0001) denotes the morphology of the pillar during point (a), (b), (c) and (d) of microcompression test.

5.3.3 Microcompression of Fe_xN on sapphire

A major obstacle in this test was to determine the Young's modulus of the thin films. This is because during compression, not only does the film deform, but the substrate also presents elastic and a small amount of plastic deformation[214]. In order to understand the elastic properties of thin films, we need to remove the influence of the substrate from the overall displacement taken from the test. The mechanical response of the Fe_xN thin films is extracted by subtracting the displacement of the sapphire substrate from the total displacement measured by the experiment. The load displacement response in microcompression is extracted from the Equation (19) developed by Yang *et al.*[155];

$$\text{Area} = \pi r^2, \text{ Diameter} = 2r$$

Where,

$$= \pi \left(\frac{D}{2} \right)^2 = \frac{\pi D^2}{4} \tag{19}$$

Thus given the equation,

$$P = E_{sapphire} \times \frac{\pi D^2}{4} \times \delta_{sapphire} \tag{20}$$

where P is the applied load, $E_{sapphire}$ is the Young's modulus of the substrate, D is the diameter of the substrate and $\delta_{Sapphire}$ is the displacement of the sapphire micropillar. The δ_{Film} is obtained by subtracting the total displacement of the system (the whole pillar) which is measured during microcompression with the displacement of the substrate (Equation 20). $E_{sapphire}$ is extracted directly from the microcompression experiment that was conducted in the previous section. The $E_{sapphire}$ obtained from this experiment is 318.5 ± 0.24 GPa. Once the $E_{sapphire}$ is known, Fe_xN thin film load-displacement curve will be able to be extracted (Figure 5.9) in order to get the Young's modulus.

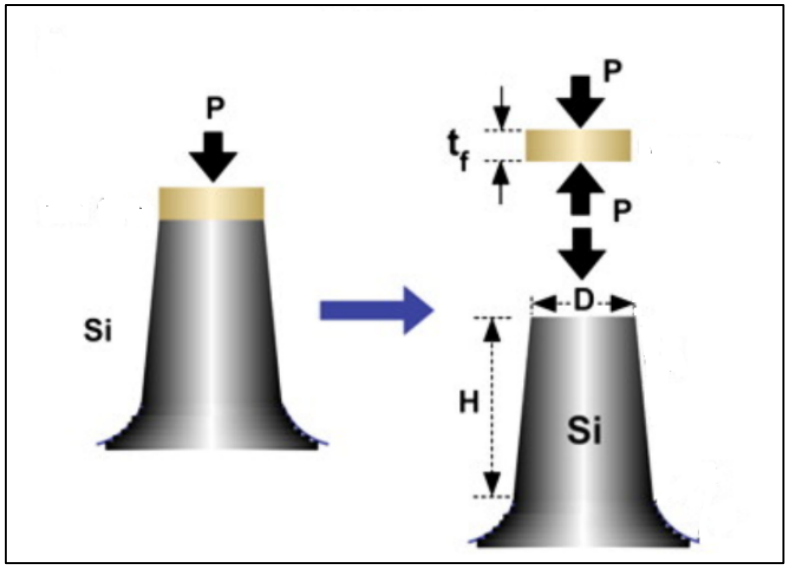


Figure 5.9: Adapted from Chu *et al.*[25] where this schematic illustration demonstrates the method of extracting mechanical properties of thin film. In our case, the substrate used is sapphire and thin films is Fe_xN and we are using the same method to get Fe_xN thin films Young's modulus.

Figure 5.10 of both Pillar 1 and Pillar 2 were extracted from the continuous loading-unloading compressive curve that corresponds to load-displacement of the pillar. The elastic modulus values of these pillars were obtained at the unloading curve in the stress-strain graph. Figure 5.10a and Figure 5.10c show the stress and strain curves of Fe_xN thin films of Pillar 1 and Pillar 2, while Figure 5.10b and Figure 5.10d show the fitting of the unloading section that was taken to find the Young's modulus. As observed, the elastic modulus increases as the cycles increase, which indicates how the contact between the punch and the surface area is changing progressively. This could either affect the surface due to roughness or gross yield of both pillars.

Referring to the trend of stress-strain curve for these two pillars (Figure 5.10a and Figure 5.10c), the gap between some of the cycles may be due to misalignment between the flat punch

and the sample, which corresponds to no contact between the sample and the flat punch. The trend of the graph for both pillars shows a linear progression as the number of cycles increased.

Pillar 1 experienced lower compressive stress, which is up 0.45 GPa compared to Pillar 2 where it gives around 0.9 GPa of compressive stress. The percentage of strain of these pillars increased from the first to the last cycle. Unlike the previous pillars of MgO and sapphires, these pillars consist of a thin film and a substrate where the change of height of the whole pillar corresponds to the mechanical properties of both thin film and substrate.

For this first cycle in Pillar 1 (Figure 5.10a), it shows a normal trend of cyclic load with minimal strain bursts occurring in the elastic region of the cycle. The trend for the initial to the final cycle was quite consistent with a given average of Young's modulus of 128 ± 0.15 GPa respectively. As for Pillar 2 (Figure 5.10c), the initial to the fourth cycles experienced a similar trend to Pillar 1.

However, as the microcompression approached the final cycle, it doubled up the compressive stress to 1.0 GPa. The average of Pillar 2 under microcompression for five cycles is calculated as 135 ± 0.20 GPa.

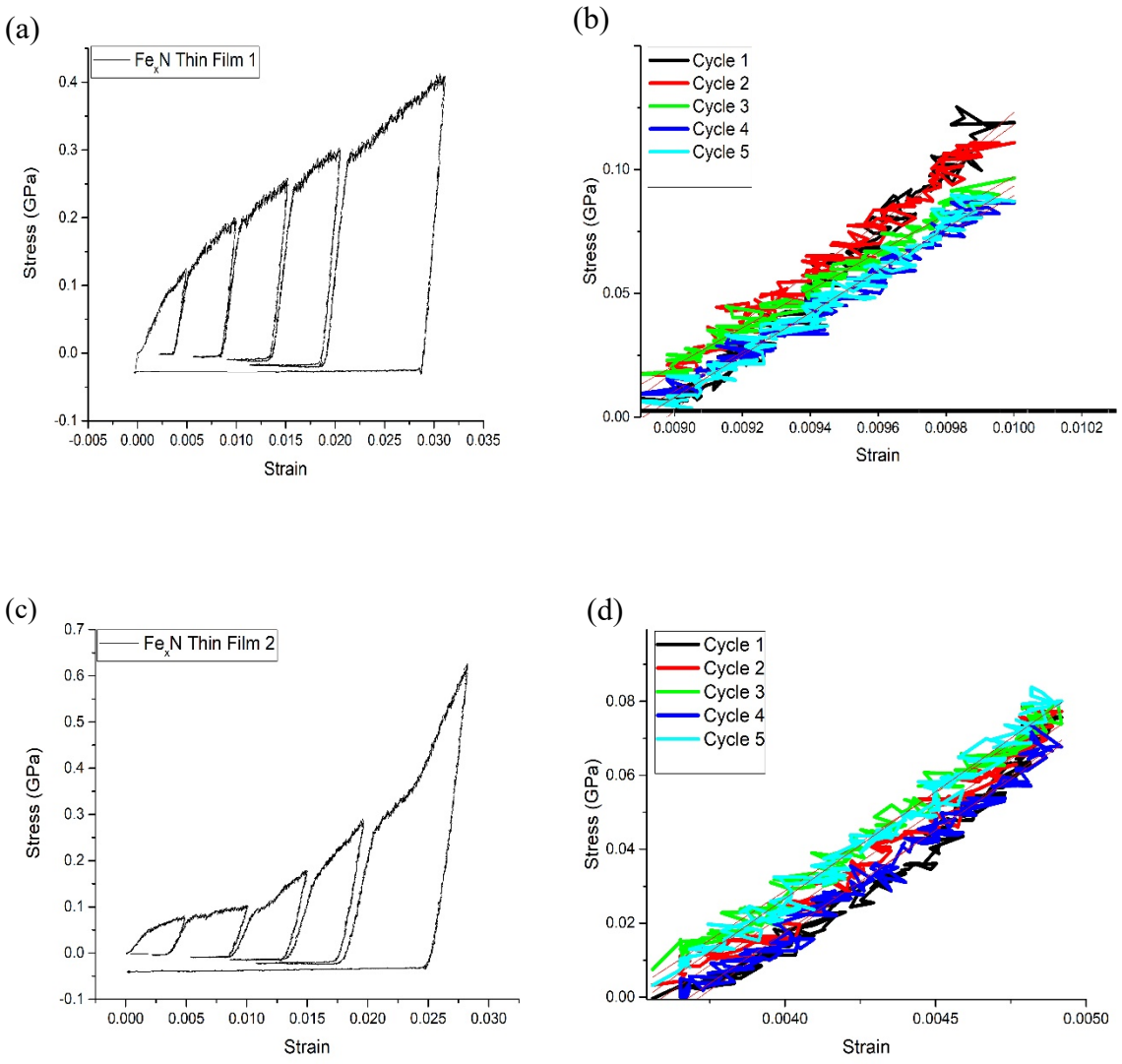


Figure 5.10: The stress-strain curves of the thin film pillars with the substrates removed of five cyclic loading and unloading cycles of Fe_xN thin film on sapphire for (a) pillar 1 with a diameter of 2.89 µm, and (c) pillar 2 with a diameter of 2.56 µm. The Young's modulus was extracted from the unloading segment of (b) pillar 1 and (d) pillar 2. The $E_{sapphire}$ was directly obtained from previous sapphire micropillar compression test.

Figure 5.11 shows the Young's modulus for each of the cycles for Pillar 1 and Pillar 2. These Young's moduli were obtained from the pillar stiffness by removing the elastic modulus of the substrate. Based on the graph presented, it is clear that these pillars show an increment in Young's modulus as the cycles increased. The average Young's modulus for both pillars is 132 GPa[81,215].

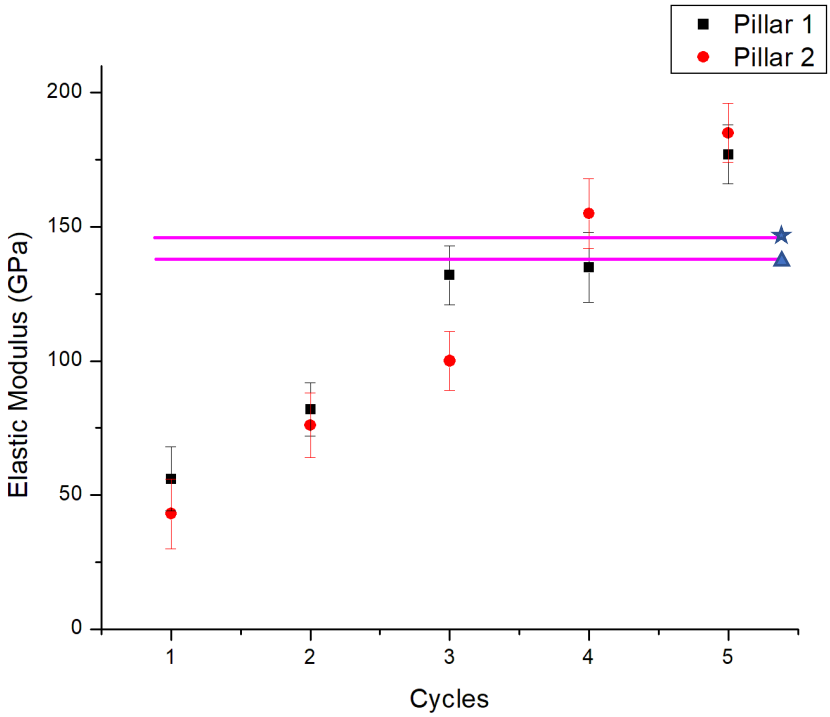


Figure 5.11: Young's modulus (GPa) of Pillar 1 (black square) and Pillar 2 (red circle) of Fe_xN thin films for five cycles during microcompression where the magenta lines show the Fe_3N literature value that was obtained from Rissanen *et al.*[13] (indicated in star) and Chen *et al.*[15] (indicated in triangle) which is between the values for third and fourth cycles for both pillars.

During the first cycle, Pillar 1 and Pillar 2 show a difference around 14 GPa of modulus. However, as compression is given to the second and third cycles, both of the pillars have almost similar values, which is around 122 GPa for Pillar 1 and 125 GPa for Pillar 2 respectively for the second cycle. As for the third cycle, Pillar 2 shows a small increment (127 GPa) in the modulus compared to Pillar 1 (133 GPa). A drastic change can be seen starting from the fourth and fifth cycles, where Pillar 2 has a higher elastic modulus compared to Pillar 1.

Another reason contributing to the lower modulus at the start of the cycle is that, during the initial cycles, the contact area between the pillar and the flat punch usually was not fully in contact leading to lower stiffness. As the cyclic load progresses, the roughness on the pillar

surface improves and becomes flatter, which results in a better contact area between the top surface of the pillar and the flat punch. Hence, a higher value of elastic modulus for the thin films was produced. Moreover, as the compression reached the final cycle, the elastic modulus for the pillars started to stabilise from which one can assume that not only has the misalignment been corrected, but the top pillar also has a flatter surface. Based on the bulk form of one of the iron nitride family which is Fe_3N, the Young's modulus is around 138.2 to 145.6 GPa[215,216].

5.3.4 Morphology of Fe_xN on sapphire micropillars

One of the key benefits of in situ testing is the ability to correlate the recorded stress-strain data with high resolution real time imaging[135]. In this case, mid-test movies and post-test microcompression SEM images reveal significant differences in deformation behaviour. The post compression behaviour in all compressed pillars were observed in Figure 5.12 until Figure 5.14.

Figure 5.12 shows the pre and post compression tests of both Pillar 1 and Pillar 2 for Fe_xN. It can be seen that for Pillar 1 (Figure 5.12a) after the compression test was conducted on it, the thin film seems to have changed in term of thickness as the flat punch pushed the top of the pillar and makes it flatter and a small deformation occurred. However, there was an apparent change on Pillar 2 (Figure 5.12b) from the pre and post SEM images where it can be seen that the top of the pillar has plastically deformed to the "mushroom" type due to cyclic load from the flat punch indenter. Furthermore, a small crack was also present on the thin film.

From Figure 5.13 and Figure 5.14, it can be observed that when the pillars are unloaded before any load-drop, loading and unloading curves are perfectly superimposed and no residual deformation such as slip was observed. Pillar 1 shows that there are no changes happening on the pillar at point (a) and point (b) (Figure 5.13a and Figure 5.13b), which is similar to Pillar 2 in point (a) and point (b) (Figure 5.14a and Figure 5.14b). This might be due to the unflattened

surface of the pillar, which is supported by the AFM data presented in Chapter 3. In the AFM results, the roughness of this thin film is quite high where these pillars did not provide a good surface for the compression to take place.

As we applied the cyclic load to the pillars' surfaces, the surface roughness deforms, which is presented in Figure 5.13c and Figure 5.13d for Pillar 1 and Figure 5.14c and Figure 5.14d for Pillar 2. This pushes the contact area and results in modulus value increment (as can be seen in the third to final cycles in both pillars). When this occurred, there is no room given for deformation to take place. Assuming the surface has been flattened and the roughness has been decreased based on the SEM images for both pillars, only then did the pillars experience plasticity, which leads to higher elastic modulus.

For Pillar 2 as presented in Figure 5.14, it can be seen then that a crack starts to be initiated in point (b) which is in the third cycle, as it went to point (c), the crack became more visible and the flattened surface on the top pillar took place and leads to point (d) that showed that the pillar has been plastically deformed in the unloading part of the stress-strain graph.

Another assumption from these images that leads to lower elastic modulus values is the presence of porosity which can be contributed to the micropillar surface and roughness. Porosity will lower the elastic modulus because there are holes in the structure which do not support the load during the microcompression[4,217] that leads to lower Young's modulus for the micropillar.

This is supported by the value of the elastic modulus for both of the pillars in this project during the two last cycles, which is around 177 GPa and 188 GPa. This value is in good agreement with the bulk sample. The initial cycles give a lower modulus as both of the pillars are experiencing (i) misalignment in the system and (ii) the roughness of the pillar surface is still an issue. These two issues have been solved as the cycles progress.

These images were extracted from the continuous loading-unloading compressive curve that corresponds to load and displacement of the pillar. The elastic modulus value increases as the number of cycles increased. Although the trend of the graph shows a linear increment, the average elastic modulus of Fe_xN for this project is still lower than expected.

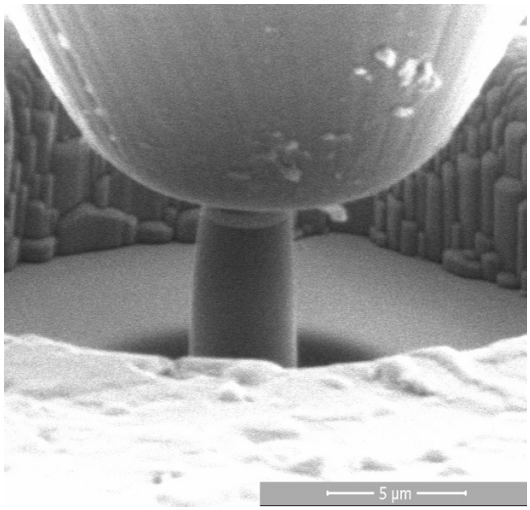
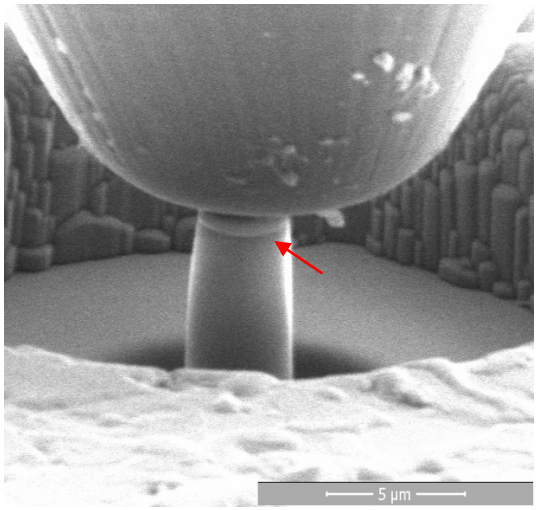
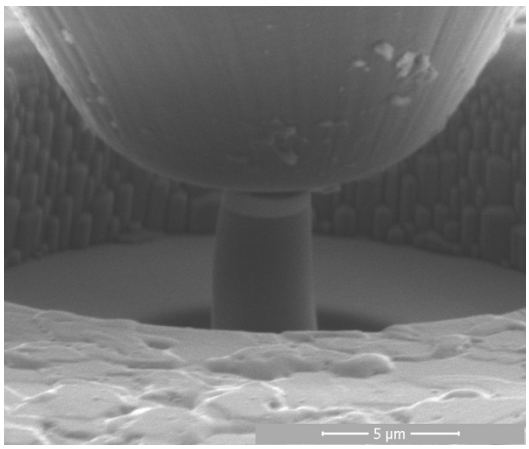
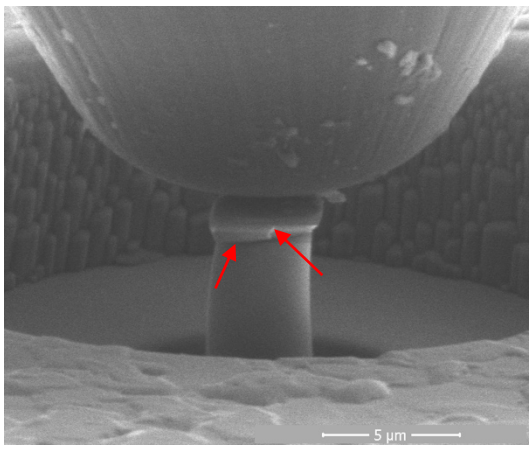
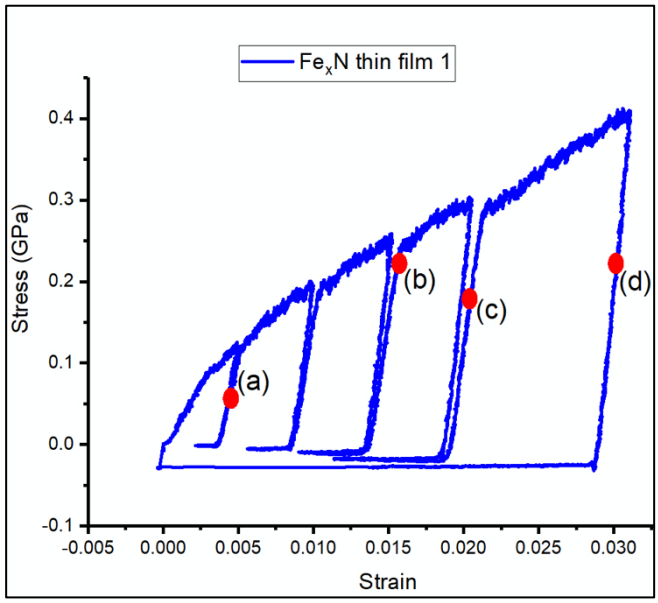
Pillar	Before	After
(a)		
(b)		

Figure 5.12: Micropillar of Fe_xN of before and after compression for (a) Pillar 1 and (b) Pillar 2 with Quanta SE, 650F with the red arrows depicting changes of the behaviour of the pillars.



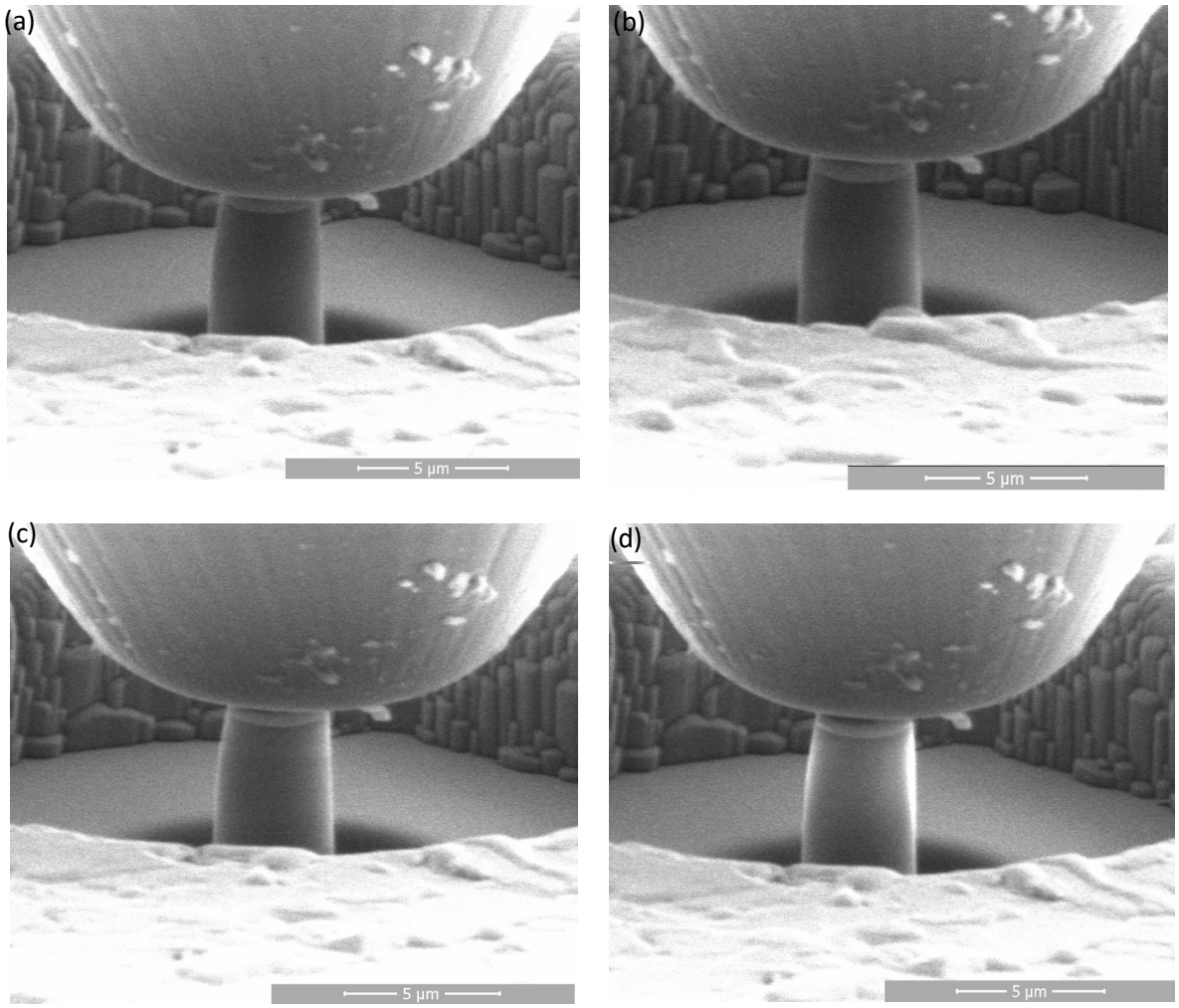


Figure 5.13: Pillar 1 of Fe_xN denotes the morphology of the pillar during point (a), (b), (c) and (d) of microcompression test.

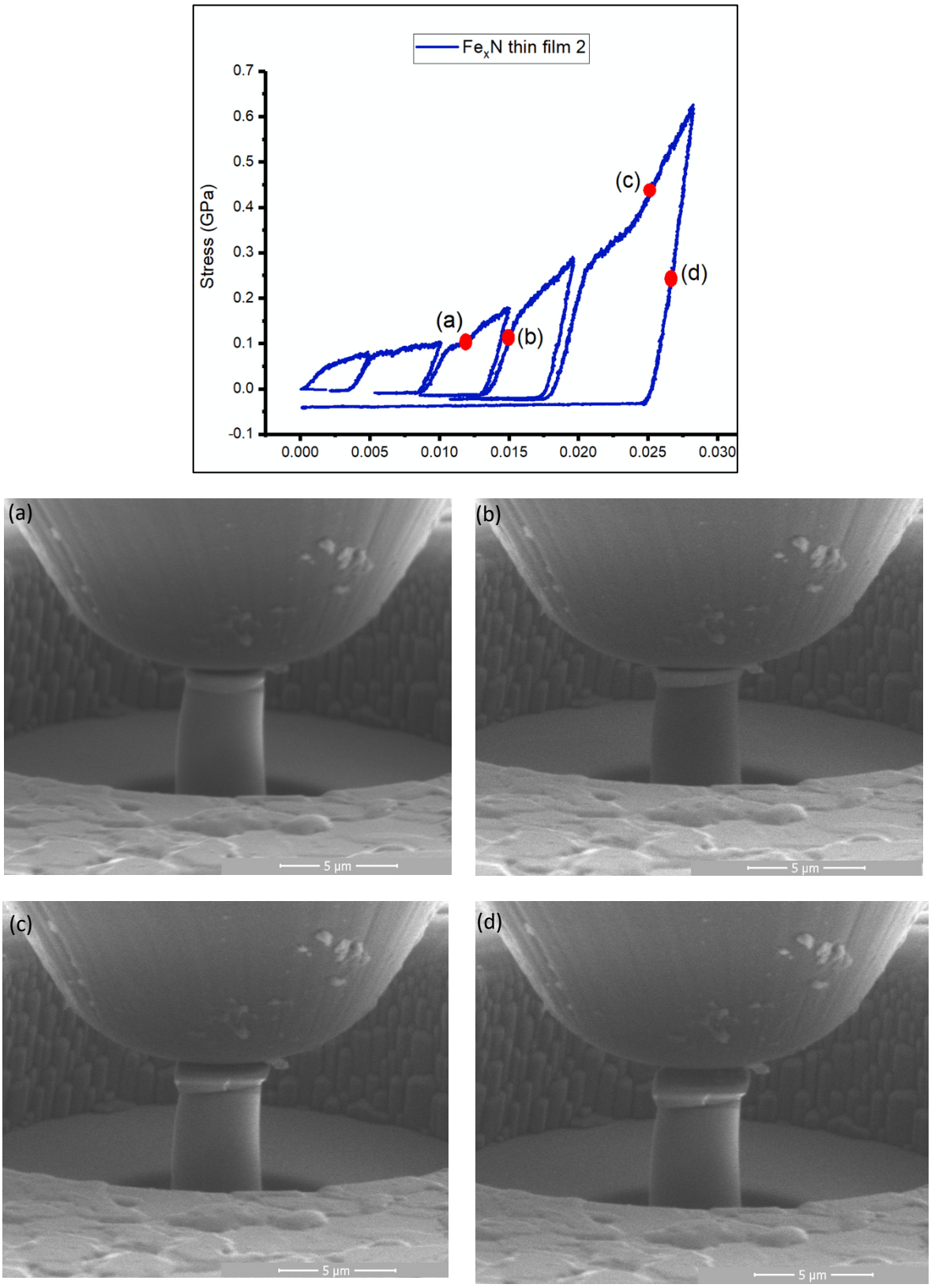


Figure 5.14: Pillar 2 of Fe_xN denotes the morphology of the pillar during point (a), (b), (c) and (d) of microcompression test.

5.4 Discussion

Referring to the trend of the sapphire graph in Figure 5.5 with the assistance of SEM images in Figure 5.7 and Figure 5.8, it can be seen that the dataset is relatively flat after a few cycles. It can be assumed that after the first cycle, there might have been misalignment, but it disappeared, by looking at the constant trend of the data after the first and second cycles. For both Pillar 1 and Pillar 2 of sapphire, the pillar started with a more pronounced misalignment issue between the pillar and the flat punch, and it took few cycles to resolve the misalignment issue.

The mode of deformation in both of these pillars is around 317 ± 0.24 GPa in Pillar 1 and 320 ± 0.24 GPa in Pillar 2, where when the average of all cycles for elastic modulus is taken the value is around 318.5 ± 0.24 GPa which is lower than the available reference. However, the value starts to increase after third cycles which might be due to roughness on the sample. If we were to exclude these first two cycles and the Young's modulus average is taken from the third cycle onwards for both of these sapphire pillars then value is far more sensible and in agreement with the literature data. Therefore, we recalculated the average elastic modulus with the cycles that we assumed have resolved the issue with misalignment and also the points that show surface formation and/or plasticity on the pillar based on the SEM images, which gives the average value of 353 ± 0.22 GPa, which is only 4 % lower than the lowest value of reference data in the literature review.

We removed these points for the reason that this is an average of the elastic modulus taken from each cycle for these two pillars but it might suggest that this in an early point that is influenced by a misalignment which happened slowly due to the presence of plastic deformation at the top of these pillars. Once the misalignment is resolved, the modulus showed a flat response on these pillars, which were then in agreement with the references.

This is strongly supported by the SEM images of the sapphire pillars that showed flattening on the top surface after the punches were removed during the microcompression test. This allowed us to make an assumption that this is happening because of some plasticity occurring on the top of the pillars and then it levels up and eventually makes the top flat and only then was it possible to apply the applied load from there.

The first assumption of lower Young's modulus value could be made about the topographic irregularities created by ion milling during FIB for sapphire pillars. This could be explained by the tapered geometry of the pillars and the diameter size (top, middle, bottom). Therefore, when microcompression is given to the pillars, the stress is unlikely to spread evenly on the sample, and instead just focuses on certain parts of it. Although the effect of ion implantation and defect nucleation by FIB is relative, it could also be attributed to the lower elastic modulus of the sapphire pillars.

As for microcompression conducted on iron thin film micropillars, based on Figure 5.5 of elastic modulus values, it can be seen that both pillars are gradually increasing as the number of cycles increased. These pillars start to increase in good agreement with the bulk samples in the third cycles onwards. Therefore, similar to reasons like sapphire pillars mentioned before, when we recalculated the points, it was found that the average for Pillar 1 is around 142.8 ± 0.15 GPa and 153.5 ± 0.20 GPa for Pillar 2, that gives the value of iron nitride thin films to be 151 ± 0.13 GPa. This is in good agreement with the literature values that stated around 142.3 GPa to 157.5 GPa for iron nitrides bulk samples.

This probably happened because the thin films were quite rough and not fully dense as there was presence of pores on the thin films. However, as loading was continually given on the pillars, we are continually compacting the surface of the films thus making the thin film a lot denser, which is proven by a smoother increment of values in the data. Similar to the sapphire

pillars, a trend of elastic modulus can be found on this thin film microcompression, where each time the pillars were given cyclic loads, the thin films got stronger (with an increment in elastic modulus).

Pillar 2 of thin film has a higher elastic modulus compared to Pillar 1. Based on the SEM images in Figure 5.12 to Figure 5.14, we can see that for Pillar 1 shown in Figure 5.12a and Figure 5.13, there is no large deformation occurring on the pillars, only a change of the thin films thickness prior to being flattened out by the flat punch. However, SEM images of pre and post microcompression for Pillar 2 (Figure 5.12b) proved that the surface of the top pillar is being flatter and denser with the presence of deformation and plasticity such as a small crack. Assuming the surface is being flattened based on the post deformation images, the roughness is believed to have decreased, thus leading to a higher elastic modulus value.

Furthermore, it was also observed that Pillar 2 of Fe_xN gives a higher elastic modulus due to the pillar being plastically deformed into mushroom like deformation while Pillar 1of Fe_xN only showed small deformation that led to a change in the thin film's thickness. Although the higher modulus was given by Pillar 2 it can be seen that a large amount of plasticity will change the area of the pillars, thus giving Pillar 1 a more stable value throughout the test compared to Pillar 2.

According to Mosyzynski *et al.*[218], a higher growth temperature of thin film (which for our project, the thin films were grown at 1000°C) usually leads to porosity of the layer, which might be the reason for a lower Young's modulus in the first and second cycles. However, as the cyclic load is increased, the pores on the thin films start closing due to the compression and results in the increase of the elastic modulus value from the third to the final cycle of microcompression. Further work of TEM shall be conducted on these samples to prove the state of porosity of these samples. From TEM imaging, one would be able to show whether the

change of property obtained by microcompression work is due to the roughness and the density of the thin films, making the elastic modulus values more reliable.

From Figure 5.14b to Figure 5.14d, it can be seen that there was crack initiated right after the third cycle, which leads to further deformation on the thin films. According to previous researchers, when growing thin films by the EBPVD method, microcracks and strains were expected to be present during the growth of thin films which often leads to defects to the thin films especially when it is non-stoichiometry thin films.

With regard to sapphire and iron nitride thin films microcompression data, comparing the stress strain data in Figure 5.4 for sapphire pillars and Figure 5.10 for Fe_xN thin films, it can be seen that the load trace between sapphire and iron nitride thin films is different. As shown in Figure 5.10 for iron nitrides, it is believed that the thin films are plastically deformed on every cyclic load during microcompression because the graph is not linear compared to stress-strain curve for sapphire pillars, which proves that the thin films have been plastically deformed. Therefore, based on the data, it is reasonable to say during cyclic load, the load given to the pillar is greatly focused on the rough surface of the pillar, which leads to deformation and also to a reduced the density of the thin film.

The trends shown in both sapphire and thin films micropillars where there was an increase in Young's modulus from the first to the fourth cycles, and sometimes the value dropped in the last cycle for both materials. This might be due to (i) the increase of the pillar surface area by removing the roughness, where this can be seen by the increase in the modulus of both pillars especially in the third cycles onwards which then leads to the second assumption that is (ii) the pillar density is increased by all the cyclic loads prior to the decrease in roughness on the pillar top surface which is shown in the stress-strain curve for both sapphire and iron nitride thin films. The trend in thin film was quite obvious where it might be due to (iii) flattening of the

whole pillar and making its surface wider, which is proven by their SEM images especially for iron thin films of Pillar 2. However, this is not happening on the sapphire pillars where one would need to be plastically deformed and the load should probably be lower than we used.

In addition, since the sapphire substrate is much stronger than Fe_xN thin films, it is assumed that the sapphire substrate only deforms elastically during microcompression tests, which is similar to the work conducted by Wang *et al.*[219,220]. Therefore, the microcompression technique is still reliable in this study although we did not get the higher value of elastic modulus as predicted from previous studies.

Furthermore, direct observation of an experiment in the SEM in combination with digital image correlation offers the additional advantage of determining the deformation directly in the sample that was tested. For example, during microcompression test, the instantaneous pillar shape together with the load applied by the indenter gives much better access to the local and instantaneous applied stress than the usually determined simple engineering stress, which assumes that the pillar deforms symmetrically.

5.5 Summary

Microcompression tests of sapphire and Fe_xN on sapphire as the substrate were conducted with the average elastic modulus of sapphire being around 319 GPa and 132 GPa based on the raw data but increased to 353 ± 0.22 GPa and 151 ± 0.13 GPa for sapphire and iron nitride thin films respectively after we removed points that we assumed to be associated with misalignment that needs to be calculated as the average of Young's modulus. The value of sapphire is still in a good agreement with the direction of this project. Meanwhile for Young's modulus for thin films showed to be in a range of the references for bulk samples due to the reasons discussed in the previous sections.

To the best of our knowledge, the iron nitride based material that is subjected to the mechanical influence in order to study its properties has not been explored. Therefore, it is very critical to understand the mechanical behaviour of these pillars when subjected to compression. It can be seen that during the last cycle, the value stabilised as the pillar surface was flattened and gave a better Young's modulus value which is in good agreement with the elastic modulus of bulk sample obtained from the reference that is around 138.2 to 145.6 GPa.

In terms of fabrication process, a higher aspect ratio is required to get better mechanical properties, therefore, increasing the film thickness will be one of the ways to get some insight for these samples.

Chapter 6

Conclusions & Further Work

6.1 Conclusions

All thin films were grown under nitrogen environment by the EBPVD method. The first series of Fe_xN thin films growth with different target ratios of x= 0.30, 0.33 and 0.35 ranging in thickness between 68 nm to 72 nm for each samples with different nitrogen flow rate found that the highest iron target ratio (x = 0.35) with 2 sccm flow rate of nitrogen seems like an ideal parameter to use for thicker thin films with a higher deposition temperature. XRD data also showed that these samples are Fe_3N, which we also assumed that nitrogen is present on the sample if we proceed with depth profiling analysis on this sample.

The second series of the growth is with a higher growth temperature, which is 1000ºC with two different growth times which were 30 minutes and 180 minutes. A higher growth resulted in a thicker sample which was 653 nm compared to 30 minutes which is 108 nm. The thicker sample showed presence of higher iron to nitrogen bond which proved that there is presence of iron nitride compound on the thin films. Meanwhile, from the XRD data shows a good agreement with the reference that the sample is Fe_3N. TEM images also shown a hexagonal crystal structure of Fe_3N thin film sample. The thicker thin film sample is nitrogen rich compared to the thinner sample because nitrogen is more active in high temperatures and there was an increase in the nitrogen emission during deposition.

We are able to measure the elastic properties of MgO 100 as 270 ± 1.9 GPa which was in good agreement with previous research. However, for MgO (110), the value obtained was lower than

the literature review which was 272 ± 1.5 GPa. The SEM images of these pillars showed deformation on the pillars' top area prior to the cyclic load given, which leads to the reason of lower value of elastic modulus compared to the references[19,41]. As for sapphire micropillars, as we exclude the points that were associated with misalignment, it is possible to measure the modulus of sapphire (353 ± 0.22 GPa) which is in good comparison with studies conducted by Saha and Nix[23] and Zoubolis *et al.*[24] which is around 370 GPa and 386 GPa by the nanoindentation and Brillouin scattering techniques.

We did not succeed in growing ternary nitrides but found two binary nitrides which were tungsten nitrides and iron nitrides on these samples. However, we managed to grow binary nitrides which is iron nitrides (Fe_xN) with elastic modulus of 151 ± 0.13 GPa and after we removed the misalignment points, the measured Young's modulus obtained were in the range of 138.2 GPa to 145.6 GPa[215,216], which is in agreement with the literature review, although this is potentially affected by porosity in the thin films.

6.2 Future work

Although some important insights regarding the growth routes and mechanical response between the materials were gained from this work, there are many areas which require further investigation.

- The growth parameters of iron nitride thin films. In order to get pure binary nitride of FeN, the nitrogen flow rate shall be intensively studied. The thickness of the sample also should be from 600 nm to 1000 nm in order to understand the effect of microcompression on the thin films.
- It is hard to grow ternary iron nitrides and to date, no research has been conducted by growing this ternary nitride by the EBPVD technique, therefore preliminary studies of

the growth routes of ternary nitrides seem like an interesting area to explore and understand, and ternary nitrides has the possibility of having better properties and performance compared to binary nitrides due to their similar MAX phase structures.

- We acknowledge the fact that during the experiment, we encountered an issue that started with cyclic loads on a porous material that leads to deformed area of the pillars that leads to unknown geometry of the post microcompression pillar. However, we are still able to obtain values that are quite sensible with the literature data. Therefore, for future work, it would be helpful to try to understand how the flattening of pillar surface occurred during the experiment and how it is possible to stop the test before the pillars experience plasticity on a large scale.
- Continuous cyclic loads given to the samples in order to understand their fracture modes and observe to what extent can the materials withhold the compaction. Furthermore, TEM investigations of the micropillar compression could be useful to study the porosity on the thin film samples especially after microcompression. This will be useful to prove that the reason for low Young's modulus might be due to the nature of the thin films as a porous material and the value only increased after it became dense.
- It is also worth to understand the slip systems that have been activated due to microcompression as it influenced the fracture mode of the samples, which can be seen clearly in MgO (100) and MgO (110) micropillars.

References

1. Högberg, H. *et al.* Growth and characterization of MAX-phase thin films. *Surf. Coatings Technol.* **193**, 6–10 (2005).

2. Geim, a K. & Grigorieva, I. V. Van der Waals heterostructures. *Nature* **499**, 419–25 (2013).

3. H.A. Wriedt, N. A. G. and R. H. N. The Fe-N (Iron-Nitrogen) System. *Bull. Alloy Phase Diagr.* **8**, 123–124 (1987).

4. Gölden, D., Hildebrandt, E. & Alff, L. Thin film phase diagram of iron nitrides grown by molecular beam epitaxy. *J. Magn. Magn. Mater.* **422**, 407–411 (2017).

5. Hari Babu, V., Rajeswari, J., Venkatesh, S. & Markandeyulu, G. Effect of thickness on structural and magnetic properties in nanocrystalline Fe–N thin films. *J. Magn. Magn. Mater.* **339**, 1–5 (2013).

6. Bem, D., Gibson, C. & Loye, H. Zur. Synthesis of intermetallic nitrides by solid-state precursor reduction. *Chem. Mater.* **5**, 397–399 (1993).

7. Miura, A. *et al.* Crystal structures and ferromagnetism of FexWN2 (x ∼ 0.74, 0.90) with defective iron triangular lattice. *J. Alloys Compd.* **593**, 154–157 (2014).

8. Weil, K. S. & Kumta, P. N. Synthesis of ternary transition metal nitrides using chemically complexed precursors. *Mater. Sci. Eng. B* **38**, 109–117 (1996).

9. Ciurea, C. C. The Influence of Temperature on the Mechanical Behaviour of Ceramics in Ti 1-x Al x N System.

10. Giovannini, T. Understanding the deformation mechanisms of CVD alpha-alumina coatings. (2018).

11. Fei, H., Abraham, A., Chawla, N. & Jiang, H. Evaluation of Micro-Pillar Compression Tests for Accurate Determination of Elastic-Plastic Constitutive Relations. *J. Appl. Mech.* **79**, 61011 (2012).

12. Innova AFM Manual, Veeco Metrology, Inc, 112 RObin Hill Rd., Santa Barbara, C. No Title.

13. Moram, M. A. & Vickers, M. E. X-ray diffraction of III-nitrides. *Reports Prog. Phys.* **72**, (2009).

14. Chit, H. & Tsui, L. Characterisation of scandium-based III- nitride thin films. (2016).

15. Calvo-barrio, L. & Vargas, G. Photoelectron spectroscopy for surface analysis: X-ray and UV excitation. 1–3 (2012).

16. Lin, Y., Hong, J., Yen, C., Tong, S. & Tung, M. X-ray photoelectron spectroscopic investigation on Fe geometrical sites of iron nitride thin films X-ray photoelectron spectroscopic investigation on Fe geometrical sites of iron nitride thin fi lms. **033002**,

1–4 (2015).

17. Davis, S. *Electron Microscopy*. (2009). doi:10.1002/9781444305395.ch14.

18. Williams, D. B. & Carter, C. B. *Transmission Electron Microscopy: A Textbook for Materials Science*. *Materials Science* vols 1–4 (2009).

19. Chung, D.-H. Elastic moduli of single crystal and polycrystalline MgO. *Philos. Mag.* **8086**, 833–841 (1963).

20. Baudson, H., Debucquoy, F., Huger, M., Gault, C. & Rigaud, M. Ultrasonic measurement of Young's modulus MgO/C refractories at high temperature. *J. Eur. Ceram. Soc.* **19**, 1895–1901 (1999).

21. Isaak, D. G., Anderson, O. L. & Goto, T. Measured elastic moduli of single-crystal MgO up to 1800 K. *Phys. Chem. Miner.* **16**, 704–713 (1989).

22. Zha, C.-S., Mao, H. & Hemley, R. J. Elasticity of MgO and a primary pressure scale to 55 GPa. *Proc. Natl. Acad. Sci. U. S. A.* **97**, 13494–13499 (2000).

23. Saha, R. & Nix, W. D. Effects of the substrate on the determination of thin film mechanical properties by nanoindentation. *Acta Mater.* **50**, 23–38 (2002).

24. Zouboulis, E. S. & Grimsditch, M. Refractive index and elastic properties of single-crystal corundum (α-Al2O3) up to 2100 K. *J. Appl. Phys.* **70**, 772–776 (1991).

25. Chu, J. P. *et al.* Thin film metallic glasses: Unique properties and potential applications. *Thin Solid Films* **520**, 5097–5122 (2012).

26. Shannon, R. D. Revised effective ionic radii in halides and chalcogenides. *Acta Crystallogr.* 751 (1976) doi:10.1107/S0567739476001551.

27. Toth, L. E. *Transition metal carbides and nitrides*. (Academic Press, 1971).

28. Bem, D. S. & Loye, H. C. Z. Synthesis of the New Ternary Transition Metal Nitride FeWN2 via Ammonolysis of a Solid State Oxide Precursor. *Journal of Solid State Chemistry* vol. 104 467–469 (1993).

29. Bem, D. S., Lampe-Önnerud, C. M., Olsen, H. P. & zur Loye, H.-C. Synthesis and Structure of Two New Ternary Nitrides: FeWN 2 and MnMoN 2. *Inorg. Chem.* **35**, 581–585 (1996).

30. Osterlund, E., Kinnunen, J., Rontu, V. & Torkkeli, A. Mechanical properties and reliability of aluminum nitride thin fi lms. **772**, 306–313 (2019).

31. Sugimoto, A., Ukita, R., Ekino, T., Zheng, Z. & Yamanaka, S. STM/STS observation on layered nitride superconductor α-(DDA)xTiNCl. *J. Phys. Conf. Ser.* **400**, (2012).

32. Yamanaka, S., Hotehama, K. & Kawaji, H. Superconductivity at 25.5 K in electron-doped layered hafnium nitride. *Nature* **392**, 580 (1998).

33. Shimamura, K. *et al.* Epitaxial Growth of GaN on (1 0 0) β-Ga $_2$ O $_3$ Substrates by Metalorganic Vapor Phase Epitaxy. *Jpn. J. Appl. Phys.* **44**, L7–L8 (2005).

34. Paszkowicz, W., Podsiadło, S. & Minikayev, R. Rietveld-refinement study of

aluminium and gallium nitrides. *J. Alloys Compd.* **382**, 100–106 (2004).

35. Haruki, M., Tada, J., Tanaka, K., Onishi, H. & Tada, Y. Enhancing the effective thermal conductivity of Kapton-type polyimide sheets via the use of hexagonal boron nitride. *Thermochim. Acta* **662**, 1–7 (2018).

36. Wang, M. *et al.* Enhanced thermal conductivity of poly(vinylidene fluoride)/boron nitride nanosheet composites at low filler content. *Compos. Part A Appl. Sci. Manuf.* **109**, 321–329 (2018).

37. Ningthoujam, R. S. & Gajbhiye, N. S. Synthesis, electron transport properties of transition metal nitrides and applications. *Prog. Mater. Sci.* **70**, 50–154 (2015).

38. Gubert, G. *et al.* Laser irradiation of iron, cobalt, and nickel targets in liquid nitrogen: A facile approach for nitride nanoparticle fabrication of ferromagnetic transition metals. *J. Alloys Compd.* **725**, 519–525 (2017).

39. Barnett, S. A. & Madan, A. Hardness and stability of metal–nitride nanoscale multilayers. *Scr. Mater.* **50**, 739–744 (2004).

40. Rasaki, S. A., Zhang, B., Anbalgam, K., Thomas, T. & Yang, M. Synthesis and application of nano-structured metal nitrides and carbides: A review. *Prog. Solid State Chem.* (2018) doi:https://doi.org/10.1016/j.progsolidstchem.2018.05.001.

41. Yoneda, A. Pressure derivatives of elastic constants of single crystal MgO and MgAl2O4. *J. Phys. Earth* **38**, 19–55 (1990).

42. Ljungcrantz, H., Oden, M., Hultman, L., Greene, J. E. & Sundgren, J. E. Nanoindentation studies of single-crystal (001)-, (011)-, and (111)-oriented TiN layers on MgO. *J. Appl. Phys.* **80**, 6725–6733 (1996).

43. Zou, Y. & Spolenak, R. Size-dependent plasticity in micron-and submicron-sized ionic crystals. *Philos. Mag. Lett.* **93**, 431–438 (2013).

44. Furimsky, E. Metal carbides and nitrides as potential catalysts for hydroprocessing. *Appl. Catal. A Gen.* **240**, 1–28 (2003).

45. Dong, S., Chen, X., Zhang, X. & Cui, G. Nanostructured transition metal nitrides for energy storage and fuel cells. *Coord. Chem. Rev.* **257**, 1946–1956 (2013).

46. Salamat, A., Hector, A. L., Kroll, P. & McMillan, P. F. Nitrogen-rich transition metal nitrides. *Coord. Chem. Rev.* **257**, 2063–2072 (2013).

47. Hargreaves, J. S. J. Heterogeneous catalysis with metal nitrides. *Coord. Chem. Rev.* **257**, 2015–2031 (2013).

48. Giménez, M. A. N. & Lopasso, E. M. Tungsten Carbide compact primary shielding for Small Medium Reactor. *Ann. Nucl. Energy* **116**, 210–223 (2018).

49. Pittari, J. J. *et al.* Sintering of tungsten carbide cermets with an iron-based ternary alloy binder: Processing and thermodynamic considerations. *Int. J. Refract. Met. Hard Mater.* (2018) doi:https://doi.org/10.1016/j.ijrmhm.2018.05.008.

50. Prokudina, V. K. Titanium Carbide. in *Concise Encyclopedia of Self-Propagating*

High-Temperature Synthesis (eds. Borovinskaya, I. P. et al.) 394–397 (Elsevier, 2017). doi:https://doi.org/10.1016/B978-0-12-804173-4.00159-9.

51. Laassiri, S., Zeinalipour-Yazdi, C. D., Catlow, C. R. A. & Hargreaves, J. S. J. Nitrogen transfer properties in tantalum nitride based materials. *Catal. Today* **286**, 147–154 (2017).

52. Hu, C., Tian, Y. & Zheng, W. A Review of Corrosion-Protective Transition Metal Nitride Coatings. *Innov. Corros. Mater. Sci.* **5**, 2–9 (2015).

53. Giordano, C. & Antonietti, M. Synthesis of crystalline metal nitride and metal carbide nanostructures by sol-gel chemistry. *Nano Today* **6**, 366–380 (2011).

54. Ted Oyama, S. Crystal structure and chemical reactivity of transition metal carbides and nitrides. *J. Solid State Chem.* **96**, 442–445 (1992).

55. Marchand, R., Laurent, Y., Guyader, J., L'Haridon, P. & Verdier, P. Nitrides and oxynitrides: Preparation, crystal chemistry and properties. *J. Eur. Ceram. Soc.* **8**, 197–213 (1991).

56. Koutsokeras, L. E. *et al.* Electronic properties of binary and ternary, hard and refractory transition metal nitrides. *Surf. Coatings Technol.* **204**, 2038–2041 (2010).

57. Roul, B., Kumar, M., Rajpalke, M. K., Bhat, T. N. & Krupanidhi, S. B. Binary group III-nitride based heterostructures: band offsets and transport properties. *J. Phys. D. Appl. Phys.* **48**, 423001 (2015).

58. Dierkes, T., Plewa, J. & Jüstel, T. From metals to nitrides - Syntheses and reaction details of binary rare earth systems. *J. Alloys Compd.* **693**, 291–302 (2017).

59. Gregory, D. H., Barker, M. G., Edwards, P. P., Slaski, M. & Siddons, D. J. Synthesis , Structure , and Magnetic Properties of the New Ternary Nitride BaHfN 2 and of the BaHf 1 ⁄ x Zr x N 2 Solid Solution. **70**, 62–70 (1998).

60. Gregoryanz, E. *et al.* Synthesis and characterization of a binary noble metal nitride. *Nat. Mater.* **3**, 294–297 (2004).

61. DiSalvo, F. J. & Clarke, S. J. Ternary nitrides: A rapidly growing class of new materials. *Curr. Opin. Solid State Mater. Sci.* **1**, 241–249 (1996).

62. Tessier, F. *et al.* Thermodynamics of Formation of Binary and Ternary Nitrides in the System Ce / Mn / N È ren Nitriden. *Z. Anorg.Allg.Chem* **627**, 194–200 (2001).

63. Dovidenko, K., Oktyabrsky, S., Narayan, J. & Razeghi, M. Aluminum nitride films on different orientations of sapphire and silicon. *J. Appl. Phys.* **79**, 2439–2445 (1996).

64. Lei, T., Ludwig, K. F. & Moustakas, T. D. Heteroepitaxy, polymorphism, and faulting in GaN thin films on silicon and sapphire substrates. *J. Appl. Phys.* **74**, 4430–4437 (1993).

65. Wickenden, D. K., Faulkner, K. R., Brander, R. W. & Isherwood, B. J. Growth of epitaxial layers of gallium nitride on silicon carbide and corundum substrates. *J. Cryst. Growth* **9**, 158–164 (1971).

66. Gregory, D. H. *et al.* Layered ternary transition metal nitrides; synthesis, structure and physical properties. *J. Alloys Compd.* **317**–**318**, 237–244 (2001).

67. Eklund, P., Beckers, M., Jansson, U., Högberg, H. & Hultman, L. The Mn + 1AXn phases: Materials science and thin-film processing. *Thin Solid Films* **518**, 1851–1878 (2010).

68. Elder, S. H. *et al.* LiMoN2: The First Metallic Layered Nitride. *Chem. Mater.* **4**, 928–937 (1992).

69. Elder, S. H. *et al.* Lithium molybdenum nitride (LiMoN2): the first metallic layered nitride. *Chem. Mater.* **4**, 928–937 (1992).

70. Elder, S. H., DiSalvo, F. J., Topor, L. & Navrotsky, A. Thermodynamics of Ternary Nitride Formation by Ammonolysis: Application to LiMoN2, Na3WN3, and Na3WO3N. *Chem. Mater.* **5**, 1545–1553 (1993).

71. Jacobs, H. & Hellmann, B. Synthesis and structure of a caesium niobium (V) nitride, CsNbN 2. *J. Alloys Compd.* **191**, 277–278 (1993).

72. Matenoglou, G. M. *et al.* Structure, stability and bonding of ternary transition metal nitrides. *Surf. Coatings Technol.* **204**, 911–914 (2009).

73. Novoselov, K. S. *et al.* Two-dimensional atomic crystals. *Proc. Natl. Acad. Sci. U. S. A.* **102**, 10451–10453 (2005).

74. Chopra, N. G. & Zettl, A. Measurement of the elastic modulus of a multi-wall boron nitride nanotube. *Solid State Commun.* **105**, 297–300 (1998).

75. Rubio, A., Corkill, J. L. & Cohen, M. L. Theory of graphitic boron nitride nanotubes. *Phys. Rev. B* **49**, 5081–5084 (1994).

76. Blase, X., Rubio, a, Louie, S. G. & Cohen, M. L. Stability and Band Gap Constancy of Boron Nitride Nanotubes. *Europhys. Lett.* **28**, 335–340 (2007).

77. Jin, C., Lin, F., Suenaga, K. & Iijima, S. Fabrication of a freestanding boron nitride single layer and Its defect assignments. *Phys. Rev. Lett.* **102**, 3–6 (2009).

78. Jack, K. H. The iron–nitrogen system: the crystal structures of ε-phase iron nitrides. *Acta Crystallogr.* **5**, 404–411 (1952).

79. Sifkovits, M., Smolinski, H., Hellwig, S. & Weber, W. Interplay of chemical bonding and magnetism in Fe N , Fe N and -Fe N. **204**, 6–9 (1999).

80. Li, G.-K. *et al.* Crystallographic phases and magnetic properties of iron nitride films. *Thin Solid Films* **589**, 22–26 (2015).

81. Chen, J.-S., Yu, C. & Lu, H. Phase stability, magnetism, elastic properties and hardness of binary iron nitrides from first principles. *J. Alloys Compd.* **625**, 224–230 (2015).

82. Coey, J. M. D. & Sun, H. Improved magnetic properties by treatment of iron-based rare earth intermetallic compounds in anmonia. *J. Magn. Magn. Mater.* **87**, 251–254 (1990).

83. Gupta, R. *et al.* Formation of iron nitride thin films with Al and Ti additives. *J. Appl. Phys.* **111**, (2012).

84. Peltzer y Blancá, E. L., Desimoni, J., Christensen, N. E., Emmerich, H. & Cottenier, S. The magnetization of γ ′-Fe4N: Theory vs. experiment. *Phys. Status Solidi Basic Res.* **246**, 909–928 (2009).

85. Komuro, M., Kozono, Y., Hanazono, M. & Sugita, Y. Epitaxial growth and magnetic properties of Fe16N2 films with high saturation magnetic flux density (invited). *J. Appl. Phys.* **67**, 5126–5130 (1990).

86. Kardonina, N. I., Yurovskikh, a S. & Kolpakov, a S. Transformations in the Fe-N System. *Met. Sci. Heat Treat.* **52**, 457–467 (2010).

87. Kim, T. K. & Takahashi, M. New magnetic material having ultrahigh magnetic moment. *Appl. Phys. Lett.* **20**, 492–494 (1972).

88. Coey, J. M. D. & Smith, P. A. I. Magnetic nitrides. *J. Magn. Magn. Mater.* **200**, 405–424 (1999).

89. Rissanen, L., Neubauer, M., Lieb, K. . & Schaaf, P. The new cubic iron-nitride phase FeN prepared by reactive magnetron sputtering. *J. Alloys Compd.* **274**, 74–82 (1998).

90. Rissanen, L. *et al.* The production of the new cubic FeN phase by reactive magnetron sputtering. *Appl. Surf. Sci.* **138**–**139**, 261–265 (1999).

91. Kappaganthu, S. R. & Sun, Y. Effect of nitrogen partial pressure and temperature on RF sputtered Fe – N films. *Surf. Coatings Technol.* **167**, 165–169 (2003).

92. Atiq, S., Ko, H. S., Siddiqi, S. A. & Shin, S. C. Effect of epitaxy and lattice mismatch on saturation magnetization of ????? - FFFe4 N thin films. *Appl. Phys. Lett.* **92**, 2–5 (2008).

93. Nikolaev, K. R. *et al.* Structural and magnetic properties of triode-sputtered epitaxial γ′-Fe4N films deposited on SrTiO3 (001) substrates. *Appl. Phys. Lett.* **82**, 4534–4536 (2003).

94. Yamaguchi, K. *et al.* Epitaxial growth of ferromagnetic Fe3N films on Si(111) substrates by molecular beam epitaxy. *J. Cryst. Growth* **301**–**302**, 597–601 (2007).

95. Nakajima, K., Okamoto, S. & Okada, T. Formation of ferromagnetic iron nitrides in iron thin films by high-dose nitrogen ion implantation. *J. Appl. Phys.* **65**, 4357–4361 (1989).

96. Wohlschlögel, M., Welzel, U. & Mittemeijer, E. J. Unexpected formation of ε iron nitride by gas nitriding of nanocrystalline α-Fe films. *Appl. Phys. Lett.* **91**, 1–4 (2007).

97. Takahashi, N., Toda, Y., Ishibashi, A. & Nakamura, T. Growth mechanism of FeN films by means of an atmospheric pressure halide chemical vapor deposition. *Mater. Chem. Phys.* **65**, 113–116 (2000).

98. Emmett, P. H., Hendricks, S. B. & Brunauer, S. The dissociation pressure of fe4n. *J. Am. Chem. Soc.* **52**, 1456–1464 (1930).

99. Borsa, D. M., Grachev, S., Presura, C. & Boerma, D. O. Growth and properties of Cu3N films and Cu3N/ γ′-Fe4N bilayers. *Appl. Phys. Lett.* **80**, 1823–1825 (2002).

100. Matar, S. F., Demazeau, G. & Siberchicot, B. Magnetic particles derived from iron nitride. *IEEE Trans. Magn.* **26**, 60–62 (1990).

101. Rissanen, L. *et al.* The production of the new cubic FeN phase by reactive magnetron sputtering. *Appl. Surf. Sci.* **138**–**139**, 261–265 (1999).

102. Hari Babu, V., Rajeswari, J., Venkatesh, S. & Markandeyulu, G. Effect of thickness on structural and magnetic properties in nanocrystalline Fe-N thin films. *J. Magn. Magn. Mater.* **339**, 1–5 (2013).

103. Mchale, J. M., Navrotsky, A., Kowach, G. R., Balbarin, V. E. & Disalvo, F. J. Energetics of Ternary Nitrides : Li - Ca - Zn - N and Ca - Ta - N Systems. **2**, 1538–1546 (1997).

104. Niewa, R. & DiSalvo, F. J. Recent Developments in Nitride Chemistry. *Chem. Mater.* **10**, 2733–2752 (1998).

105. Bem, D. S., Olsen, H. P. & zur Loye, H. C. Synthesis, Electronic and Magnetic Characterization of the Ternary Nitride (Fe0.8Mo0.2)MoN2. *Chem. Mater.* **7**, 1824–1828 (1995).

106. Li, C. & Wang, Z. 9 - Computational modelling and ab initio calculations in {MAX} phases – I. in *Advances in Science and Technology of Mn+1AXn Phases* (ed. Low, I. M.) 197–222 (Woodhead Publishing, 2012). doi:https://doi.org/10.1533/9780857096012.197.

107. Faurie, D. *et al.* Elastic anisotropy of polycrystalline Au films: Modeling and respective contributions of X-ray diffraction, nanoindentation and Brillouin light scattering. *Acta Mater.* **58**, 4998–5008 (2010).

108. Cohen, R. E. & Krakauer, H. Electronic structure studies of the differences in ferroelectric behavior of batio 3 and PbTiO 3. *Ferroelectrics* **136**, 65–83 (1992).

109. Bannikov, V. V., Shein, I. R. & Ivanovskii, A. L. Electronic structure, chemical bonding and elastic properties of the first thorium-containing nitride perovskite TaThN3. *Phys. Status Solidi - Rapid Res. Lett.* **1**, 89–91 (2007).

110. Mattesini, M. *et al.* Elastic properties and electrostructural correlations in ternary scandium-based cubic inverse perovskites: A first-principles study. *Phys. Rev. B - Condens. Matter Mater. Phys.* **79**, 1–9 (2009).

111. Migliori, A. *et al.* Resonant ultrasound spectroscopic techniques for measurement of the elastic moduli of solids. *Phys. B* **183**, 1–24 (1993).

112. Leisure, R. G. & Willis, F. a. Resonant ultrasound spectroscopy. *J. Phys. Condens. Matter* **9**, 6001–6029 (1999).

113. Schwarz, R. B. & Vuorinen, J. F. Resonant ultrasound spectroscopy: Applications, current status and limitations. *J. Alloys Compd.* **310**, 243–250 (2000).

114. Radovic, M., Lara-Curzio, E. & Riester, L. Comparison of different experimental

techniques for determination of elastic properties of solids. *Mater. Sci. Eng. A* **368**, 56–70 (2004).

115. Oliver, W. C., Pharr, G. M. & Introduction, I. An improved technique for determining hardness and ellastic modulus using load and displacement sensing indentation experiement. (1992).

116. Doerner, M. F. & Nix, W. D. A method for interpreting the data from depth-sensing indentation instruments. *J. Mater. Res.* **1**, 601–609 (1986).

117. Fischer-cripps, A. C. *Introduction to Contact Mechanics*. *Introduction to Contact Mechanics* (2000). doi:10.1007/b97709.

118. Fischer-Cripps, A. C. Critical review of analysis and interpretation of nanoindentation test data. *Surf. Coatings Technol.* **200**, 4153–4165 (2006).

119. Zeng, Z. & Tan, J. C. AFM Nanoindentation to Quantify Mechanical Properties of Nano- and Micron-Sized Crystals of a Metal-Organic Framework Material. *ACS Appl. Mater. Interfaces* **9**, 39839–39854 (2017).

120. Pharr, G. M. & Oliver, W. C. Measurement of thin film mechanical properties using nanoindentation. *Mrs Bull.* **17**, 28–33 (1992).

121. Li, H. & Vlassak, J. J. Determining the elastic modulus and hardness of an ultra-thin film on a substrate using nanoindentation. *J. Mater. Res.* **24**, 1114–1126 (2009).

122. Chen, X. & Vlassak, J. J. Numerical study on the measurement of thin film mechanical properties by means of nanoindentation. (2001).

123. Hong, S. H. *et al.* Characterization of elastic moduli of Cu thin films using nanoindentation technique. *Compos. Sci. Technol.* **65**, 1401–1408 (2005).

124. Fischer-Cripps, A. C. A simple phenomenological approach to nanoindentation creep. *Mater. Sci. Eng. A* **385**, 74–82 (2004).

125. Feng, G. & Nix, W. D. Indentation size effect in MgO. *Scr. Mater.* **51**, 599–603 (2004).

126. Bucaille, J. L., Stauss, S., Felder, E. & Michler, J. Determination of plastic properties of metals by instrumented indentation using different sharp indenters. *Acta Mater.* **51**, 1663–1678 (2003).

127. Giannakopoulos, A. E. & Suresh, S. Determination of elastoplastic properties by instrumented sharp indentation. *Scr. Mater.* **40**, 1191–1198 (1999).

128. Bhushan, B. & Li, X. Nanomechanical characterisation of solid surfaces and thin films. *Int. Mater. Rev.* **48**, 125–164 (2003).

129. Gouldstone, A., Koh, H. J., Zeng, K. Y., Giannakopoulos, A. E. & Suresh, S. Discrete and continuous deformation during nanoindentation of thin films. *Acta Mater.* **48**, 2277–2295 (2000).

130. Gouldstone, A. *et al.* Indentation across size scales and disciplines: Recent developments in experimentation and modeling. *Acta Mater.* **55**, 4015–4039 (2007).

131. Uchic, M. D., Shade, P. A. & Dimiduk, D. M. Micro-compression testing of fcc metals: A selected overview of experiments and simulations. *Jom* **61**, 36–41 (2009).

132. Uchic, M. D. & Dimiduk, D. M. A methodology to investigate size scale effects in crystalline plasticity using uniaxial compression testing. *Mater. Sci. Eng. A* **400–401**, 268–278 (2005).

133. Soler, R. *et al.* Micropillar compression of LiF [1 1 1] single crystals: Effect of size, ion irradiation and misorientation. *Int. J. Plast.* **36**, 50–63 (2012).

134. Guillonneau, G. *et al.* Nanomechanical testing at high strain rates: New instrumentation for nanoindentation and microcompression. *Mater. Des.* **148**, 39–48 (2018).

135. Reichardt, A. *et al.* Nanoindentation and in situ microcompression in different dose regimes of proton beam irradiated 304 SS. *J. Nucl. Mater.* **486**, 323–331 (2017).

136. Wörgötter, H., Kiener, D., Purswani, J. M., Gall, D. & Dehm, G. Testing Thin Films by Microcompression : Benefits and Limits. 257–262 (2008).

137. Schuster, B. E. *et al.* Bulk and microscale compressive properties of a Pd-based metallic glass. *Scr. Mater.* **57**, 517–520 (2007).

138. Oliver, W. C. & Pharr, G. M. Measurement of hardness and elastic modulus by instrumented indentation: Advances in understanding and refinements to methodology. *J. Mater. Res.* **19**, 3–20 (2004).

139. Zhang, H., Schuster, B. E., Wei, Q. & Ramesh, K. T. The design of accurate micro-compression experiments. *Scr. Mater.* **54**, 181–186 (2006).

140. Singh, J. & Wolfe, D. E. Nano and macro-structured component fabrication by electron beam-physical vapor deposition (EB-PVD). *J. Mater. Sci.* **40**, 1–26 (2005).

141. Wolfe, D. E., Singh, J. & Narasimhan, K. Synthesis and characterization of multilayered TiC/TiB2 coatings deposited by ion beam assisted, electron beam–physical vapor deposition (EB–PVD). *Surf. Coatings Technol.* **165**, 8–25 (2003).

142. Mazurkiewicz, A., Smolik, J., Zbrowski, A. & Kacprzyńska, J. Innovative technical solutions for evaporation of multilayer coatings by EB-PVD method. *Arch. Civ. Mech. Eng.* **14**, 250–254 (2014).

143. Johnson, D., Hilal, N. & Bowen, W. R. *Basic principles of atomic force microscopy*. *Atomic Force Microscopy in Process Engineering* (Elsevier Ltd, 2009). doi:10.1016/B978-1-85617-517-3.00001-8.

144. Hobbs, J. K., Farrance, O. E. & Kailas, L. How atomic force microscopy has contributed to our understanding of polymer crystallization. *Polymer (Guildf).* **50**, 4281–4292 (2009).

145. Loos, J. The Art of SPM: Scanning Probe Microscopy in Materials Science. *Adv. Mater.* **17**, 1821–1833 (2005).

146. McLean, R. S. & Sauer, B. B. Tapping-mode AFM studies using phase detection for resolution of nanophases in segmented polyurethanes and other block copolymers.

Macromolecules **30**, 8314–8317 (1997).

147. Thomas, J. H. Photoelectron Spectroscopy : Applications to Semiconductors. (2014).

148. Pinto, R. M.-R. Photoelectron Spectroscopy of Nitrogen Containing Molecules Of Biological and Industrial Interest. vol. 3 (Universidade Nova De Lisboa, 2011).

149. Haasch, R. X-Ray Photoelectron Spectroscopy (XPS) and Auger Electron Spectroscopy (AES). *Pract. Mater. charactrization* 99–132 (2014) doi:10.1007/978-1-4614-9281-8_3.

150. Nguyen, T. D., Keefe, M. A. O., Kilaas, R., Gronsky, R. & Kortright, J. B. Effects of Fresnel Fringes on TEM Images of Interfaces in X-Ray Multilayers Effects of Fresnel Fringes on TEM Images of Interfaces in X-Ray Multilayers. **7**, 94–96 (1992).

151. Gholinia, A. *Introduction to Focused Ion Beam (FIB)*. (2011).

152. Swanson, L. W. Liquid metal ion sources: Mechanism and applications. *Nucl. Instruments Methods Phys. Res.* **218**, 347–353 (1983).

153. Prasad, K. E., Rajesh, K. & Ramamurty, U. Micropillar and macropillar compression responses of magnesium single crystals oriented for single slip or extension twinning. *Acta Mater.* **65**, 316–325 (2014).

154. Sernicola, G. *et al.* In situ stable crack growth at the micron scale. *Nat. Commun.* **8**, (2017).

155. Yang, Y., Ye, J. C., Lu, J., Liu, F. X. & Liaw, P. K. Effects of specimen geometry and base material on the mechanical behavior of focused-ion-beam-fabricated metallic-glass micropillars. *Acta Mater.* **57**, 1613–1623 (2009).

156. Kim, Y. Micropillar Arrays for High Sensitivity Sensors by. (2016).

157. Greer, J. R. & Nix, W. D. Nanoscale gold pillars strengthened through dislocation starvation. *Phys. Rev. B - Condens. Matter Mater. Phys.* **73**, 1–6 (2006).

158. Wang, S., Yang, Y., Zhou, L. M. & Mai, Y. W. Size effect in microcompression of epoxy micropillars. *J. Mater. Sci.* **47**, 6047–6055 (2012).

159. Jun, T. S., Sernicola, G., Dunne, F. P. E. & Britton, T. B. Local deformation mechanisms of two-phase Ti alloy. *Mater. Sci. Eng. A* **649**, 39–47 (2016).

160. Pharr, G. M., Oliver, W. C. & Brotzen, F. R. On the generality of the relationship among cantact stiffness,contact area, and elastic-modulus during indentation. *J. Mater. Res.* **7**, 613–617 (1992).

161. Frick, C. P., Clark, B. G., Orso, S., Schneider, A. S. & Arzt, E. Size effect on strength and strain hardening of small-scale [111] nickel compression pillars. *Mater. Sci. Eng. A* **489**, 319–329 (2008).

162. Jiang, L. & Chawla, N. Mechanical properties of Cu6Sn5 intermetallic by micropillar compression testing. *Scr. Mater.* **63**, 480–483 (2010).

163. Jun, T. S., Zhang, Z., Sernicola, G., Dunne, F. P. E. & Britton, T. B. Local strain rate sensitivity of single α phase within a dual-phase Ti alloy. *Acta Mater.* **107**, 298–309

(2016).

164. Lee, C. J., Huang, J. C. & Nieh, T. G. Sample size effect and microcompression of Mg65 Cu25 Gd10 metallic glass. *Appl. Phys. Lett.* **91**, 2007–2009 (2007).

165. Wang, X. *et al.* Growth, structural, and magnetic properties of iron nitride thin films deposited by dc magnetron sputtering. *Appl. Surf. Sci.* **220**, 30–39 (2003).

166. Prieto, P., Marco, J. F. & Sanz, J. M. Synthesis and characterization of iron nitrides. An XRD, Mössbauer, RBS and XPS characterization. *Surf. Interface Anal.* **40**, 781–785 (2008).

167. Tao, Z. K. *et al.* Ferromagnetic Fe3N films grown on GaN(0 0 0 2) substrates by MOCVD. *J. Cryst. Growth* **312**, 1525–1528 (2010).

168. Khan, W. Q., Wang, Q., Jin, X. & Yasin, G. Corrosion, optical and magnetic properties of flexible iron nitride nano thin films deposited on polymer substrate. *Phys. B Condens. Matter* **524**, 71–80 (2017).

169. Dirba, I., Komissinskiy, P., Gutfleisch, O. & Alff, L. Increased magnetic moment induced by lattice expansion from α -Fe to α'-Fe_8N. *J. Appl. Phys.* **117**, 173911 (2015).

170. Zheng, J. *et al.* Iron nitride thin films deposited by chloride assisted plasma enhanced chemical vapour deposition: Facile stoichiometry control and mechanism study. *J. Phys. D. Appl. Phys.* **42**, (2009).

171. Kong, A., Kong, Y., Zhu, X., Han, Z. & Shan, Y. Ordered mesoporous Fe (or Co)-N-graphitic carbons as excellent non-precious-metal electrocatalysts for oxygen reduction. *Carbon N. Y.* **78**, 49–59 (2014).

172. Zhao, Y., Watanabe, K. & Hashimoto, K. Self-supporting oxygen reduction electrocatalysts made from a nitrogen-rich network polymer. *J. Am. Chem. Soc.* **134**, 19528–19531 (2012).

173. Kuivila, C. S., Butt, J. B. & Stair, P. C. Characterization of surface species on iron synthesis catalysts by X-ray photoelectron spectroscopy. *Appl. Surf. Sci.* **32**, 99–121 (1988).

174. Xiao, H., Shao, Z. & Lu, W. Fe – N – carbon black for the oxygen reduction reaction in sulfuric acid. *Carbon N. Y.* **57**, 443–451 (2013).

175. Wu, G. *et al.* Synthesis-structure-performance correlation for polyaniline-Me-C non-precious metal cathode catalysts for oxygen reduction in fuel cells. *J. Mater. Chem.* **21**, 11392–11405 (2011).

176. Villasana, Y. *et al.* Atomic ratio effect on catalytic performance of FeW-based carbides and nitrides on thiophene hydrodesulfurization. *Fuel* **110**, 259–267 (2013).

177. Bem, D. S. & Loye, H.-C. Zur. Synthesis of the New Ternary Transition Metal Nitride FeWN2 via Ammonolysis of a Solid State Oxide Precursor. *J. Solid State Chem.* **104**, 467–469 (1993).

178. Koutsokeras, L. Growth, structure and electronic properties of ternary transition metal

nitrides thin films. (2010).

179. Sugita, Y. *et al.* Giant magnetic moment and other magnetic properties of epitaxially grown Fe16N2 single-crystal films (invited). *J. Appl. Phys.* **70**, 5977 (1991).

180. Ramaseshan, R., Jose, F., Rajagopalan, S. & Dash, S. Preferentially orientated E-beam TiN thin films using focused jet of nitrogen gas. 1–6 (2014).

181. Etaati, G. R., Hosseinnejad, M. T., Ghoranneviss, M., Habibi, M. & Shirazi, M. Deposition of tungsten nitride on stainless steel substrates using plasma focus device. *Nucl. Instruments Methods Phys. Res. Sect. B Beam Interact. with Mater. Atoms* **269**, 1058–1062 (2011).

182. Subramanya Herle, P., Vasanthacharya, N. Y., Hegde, M. S. & Gopalakrishnan, J. Synthesis of new transition metal nitrides, MWN2 (M□Mn, Co, Ni). *J. Alloys Compd.* **217**, 22–24 (1995).

183. Comini, E., Pandolfi, L., Kaciulis, S., Faglia, G. & Sberveglieri, G. Correlation between atomic composition and gas sensing properties in tungsten-iron oxide thin films. *Sensors Actuators, B Chem.* **127**, 22–28 (2007).

184. García-Valenzuela, J. A., Andreu, J. & Bertomeu, J. Effect of the base pressure achieved prior deposition on the main properties of ZnO:Al films obtained by DC magnetron sputtering at room temperature for electrical contact use. *J. Vac. Sci. Technol. A Vacuum, Surfaces, Film.* **35**, 021603 (2017).

185. Hott, R., Kleiner, R., Wolf, T. & Zwicknagl, G. Review on Superconducting Materials. (2013).

186. Frankel, G. S., Chen, X.-B., Gupta, R. K., Kandasamy, S. & Birbilis, N. Effect of Vacuum System Base Pressure on Corrosion Resistance of Sputtered Al Thin Films. *J. Electrochem. Soc.* **161**, C195–C200 (2014).

187. Jantasom, K. *et al.* Influence of nitrogen flow rates on iron nitride thin films prepared by DC reactive magnetron sputtering. *Mater. Today Proc.* **4**, 6173–6177 (2017).

188. Chen, Y., Halstead, T. & Williams, J. S. Influence of milling temperature and atmosphere on the synthesis of iron nitrides by ball milling. **5093**, (1996).

189. Stavrev, M., Fischer, D., Wenzel, C., Drescher, K. & Mattern, N. Crystallographic and morphological characterization of reactively sputtered Ta, Ta-N and Ta-N-O thin films. *Thin Solid Films* **307**, 79–88 (1997).

190. Bhattacharyya, S. Iron nitride family at reduced dimensions: A review of their synthesis protocols and structural and magnetic properties. *J. Phys. Chem. C* **119**, 1601–1622 (2015).

191. Ajenifuja, E., Popoola, A. P. I. & Popoola, O. M. Thickness dependent chemical and microstructural properties of DC reactive magnetron sputtered titanium nitride thin films on low carbon steel cross-section. *J. Mater. Res. Technol.* **8**, 377–384 (2019).

192. Roth, R., Schubert, J., Martin, M. & Fromm, E. Effect of process parameter changes on the composition of magnetron sputtered and evaporated TiN and AlN films measured by UHV in-situ techniques. *Thin Solid Films* **270**, 320–324 (1995).

193. Ajenifuja, E., Osinkolu, G. A., Yisau Fasasi, A., Pelemo, D. A. & Obiajunwa, E. I. Rutherford backscattering spectroscopy and structural analysis of DC reactive magnetron sputtered titanium nitride thin films on glass substrates. *J. Mater. Sci. Mater. Electron.* **27**, 335–341 (2016).

194. Bhattacharyya, S., Kurian, S., Shivaprasad, S. M. & Gajbhiye, N. S. Synthesis and magnetic characterization of CoMoN2 nanoparticles. *J. Nanoparticle Res.* **12**, 1107–1116 (2010).

195. Marchand, R., Tessier, F. & DiSalvo, F. J. New routes to transition metal nitrides: and characterization of new phases. *J. Mater. Chem.* **9**, 297–304 (1999).

196. Korte, S., Ritter, M., Jiao, C., Midgley, P. A. & Clegg, W. J. Three-dimensional electron backscattered diffraction analysis of deformation in MgO micropillars. *Acta Mater.* **59**, 7241–7254 (2011).

197. Korte, S. & Clegg, W. J. Discussion of the dependence of the effect of size on the yield stress in hard materials studied by microcompression of MgO. *Philos. Mag.* **91**, 1150–1162 (2011).

198. Chung, D. H. & Buessem, W. R. The elastic anisotropy of crystals. *J. Appl. Phys.* **38**, 2010–2012 (1967).

199. Montagne, A., Audurier, V. & Tromas, C. Influence of pre-existing dislocations on the pop-in phenomenon during nanoindentation in MgO. *Acta Mater.* **61**, 4778–4786 (2013).

200. Csanádi, T. *et al.* Deformation characteristics of WC micropillars. *J. Eur. Ceram. Soc.* **34**, 4099–4103 (2014).

201. Greer, J. R., Oliver, W. C. & Nix, W. D. Size dependence of mechanical properties of gold at the micron scale in the absence of strain gradients. *Acta Mater.* **53**, 1821–1830 (2005).

202. Kunz, A., Pathak, S. & Greer, J. R. Size effects in Al nanopillars: Single crystalline vs. bicrystalline. *Acta Mater.* **59**, 4416–4424 (2011).

203. Li, H., Ngan, A. H. W. & Wang, M. G. Continuous strain bursts in crystalline and amorphous metals during plastic deformation by nanoindentation. *J. Mater. Res.* **20**, 3072–3081 (2005).

204. Howie, P. R., Korte, S. & Clegg, W. J. Fracture modes in micropillar compression of brittle crystals. *J. Mater. Res.* **27**, 141–151 (2012).

205. Howie, P. R., Korte, S. & Clegg, W. J. Fracture modes in micropillar compression of brittle crystals. *J. Mater. Res.* **27**, 141–151 (2012).

206. Nagoshi, T., Shibata, A., Todaka, Y., Sato, T. & Sone, M. Mechanical behavior of a microsized pillar fabricated from ultrafine-grained ferrite evaluated by a microcompression test. *Acta Mater.* **73**, 12–18 (2014).

207. Soler, R. *et al.* Understanding size effects on the strength of single crystals through high-temperature micropillar compression. *Acta Mater.* (2014) doi:10.1016/j.actamat.2014.08.007.

208. Korte-Kerzel, S. Microcompression of brittle and anisotropic crystals: Recent advances and current challenges in studying plasticity in hard materials. *MRS Commun.* **7**, 109–120 (2017).

209. Montagne, A., Pathak, S., Maeder, X. & Michler, J. Plasticity and fracture of sapphire at room temperature : Load-controlled microcompression of four different orientations. *Ceram. Int.* **40**, 2083–2090 (2014).

210. Wheeler, J. M. *et al.* The plasticity of indium antimonide: Insights from variable temperature, strain rate jump micro-compression testing. *Acta Mater.* **106**, 283–289 (2016).

211. Troyon, M. & Lafaye, S. About the importance of introducing a correction factor in the Sneddon relationship for nanoindentation measurements. *Philos. Mag.* **86**, 5299–5307 (2006).

212. Ghosh, R., Basak, D. & Fujihara, S. Effect of substrate-induced strain on the structural, electrical, and optical properties of polycrystalline ZnO thin films. *J. Appl. Phys.* **96**, 2689–2692 (2004).

213. Luan, X. *et al.* The mechanical response characteristics of sapphire under dynamic and quasi-static indentation loading. *Ceram. Int.* (2018) doi:10.1016/j.ceramint.2018.05.162.

214. Antunes, J. M., Fernandes, J. V., Sakharova, N. A., Oliveira, M. C. & Menezes, L. F. On the determination of the Young's modulus of thin films using indentation tests. *Int. J. Solids Struct.* **44**, 8313–8334 (2007).

215. Rissanen, L., Neubauer, M., Lieb, K. . & Schaaf, P. The new cubic iron-nitride phase FeN prepared by reactive magnetron sputtering. *J. Alloys Compd.* **274**, 74–82 (1998).

216. Cheng, C.-H. *et al.* Magnetic and Mechanical Properties of Deformed Iron Nitride - Fe4N, Magnetic and Mechanical Properties of Deformed Iron Nitride -Fe4N. *J. Appl. Math. J. Appl. Math.* **2015**, **2015**, e238730 (2015).

217. Braeckman, B. R., Djemia, P., Tétard, F., Belliard, L. & Depla, D. Impurity-controlled film growth and elastic properties of CoCrCuFeNi thin films. *Surf. Coatings Technol.* **315**, 475–483 (2017).

218. Moszyński, D., Kiełbasa, K. & Arabczyk, W. Influence of crystallites' size on iron nitriding and reduction of iron nitrides in nanocrystalline Fe–N system. *Mater. Chem. Phys.* **141**, 674–679 (2013).

219. Wang, J. Mechanical Behaviour of Metallic Thin Films and Multilayers at the Micron / submicron Scale. (2012).

220. Wang, J., Yang, C. & Hodgson, P. D. Mechanical Behavior of Nano-crystalline Metallic Thin Films and Multilayers Under Microcompression. *Metall. Mater. Trans. A Phys. Metall. Mater. Sci.* **46**, 1405–1412 (2015).

Appendix A

Permission for third party copyright works

Here is the list of permission obtained for reproducing figures in this thesis from third party copyright works and the permission documents are attaches

Figure	Source of work, copyright holder and year
Figure 1.2, page 14	Nature (2013)499,7459 (Figure 1)©Springer Nature
Figure 1.4, page 17	Journal of Magnetism and Magnetic Materials (2017)5, 422 (Figure 8) ©Elsevier
Figure 1.5, page 19	Journal of Magnetism and Magnetic Materials (2013)4, 339 (Figure 2) ©Elsevier
Figure 1.6, page 20	Journal of Solid State Chemistry (1993),2, 104 (Figure 1) ©Elsevier
Figure 1.7, page 21	Journal of Solid State Chemistry (2010),5, 183 (Figure 1) ©Elsevier
Figure 1.8, page 22	Materials Science and Engineering: B (1996)2, 38 (Figure 2) ©Elsevier
Figure 2.10, page 56	Transmission Electron Microscopy: A textbook for Materials Science Ch. 19, 2009, 274 ©Springer